Satellite Measurements of Carbon Dioxide: Analysis and Reduction of Scattering Related Retrieval Errors

Jens Heymann

Universität Bremen 2013

Satellite Measurements of Carbon Dioxide: Analysis and Reduction of Scattering Related Retrieval Errors

Vom Fachbereich für Physik und Elektrotechnik
der Universität Bremen

zur Erlangung des akademischen Grades eines

Doktor der Naturwissenschaften (Dr. rer. nat.)

genehmigte Dissertation

von

Dipl. Phys. Jens Heymann

aus Bremerhaven

1.Gutachter:	Prof. Dr. J. P. Burrows
2.Gutachter:	Prof. Dr. O. Schrems
Eingereicht am:	22.01.2013
Tag des Promotionskolloquiums:	04.04.2013

Abstract

The greenhouse gas carbon dioxide (CO_2) is the most important human-made contributor to global warming. Despite its importance, our knowledge about its sources and sinks has large gaps. This limits a reliable climate prediction. Satellite observations of atmospheric CO_2 combined with modelling can help to reduce these knowledge gaps. However, this requires to meet demanding accuracy and precision requirements for the satellite instrument, the retrieval algorithm and the model.

One of the most important error sources for satellite retrievals of CO_2 from reflected and backscattered solar radiation is unaccounted scattering by aerosols and clouds. In this context, the objectives of this thesis are to assess the quality of an existing satellite-based CO_2 data set focussing on the investigation of these error source and to generate and validate an improved CO_2 data set.

The CO_2 data bases on measurements of the passive remote sensing satellite instrument SCIAMACHY on-board ENVISAT, which has performed more than 10 years of radiance measurements in the short wave infrared spectral region. In the period 2003 – 2009, SCIAMACHY was the only satellite instrument measuring CO_2 with high sensitivity down to the Earth's surface where the sources and sinks of CO_2 are located. Therefore, the SCIAMACHY measurements are important in terms of generating an accurate global long-term atmospheric CO_2 data set.

Starting point for this thesis was an analysis of an existing 7-year (2003 – 2009) data set of column-averaged dry air mole-fraction of CO_2, denoted XCO_2, which was generated with version 2.1 of the Weighting Function Modified - Differential Optical Absorption Spectroscopy (WFM-DOAS) retrieval algorithm (WFMDv2.1).

Initially, a scan-angle-dependent bias of this data set has been identified. Simulated retrievals indicate that this error is caused by not fully accounted scattering related light path modifications. An empirical correction method has been developed to correct for this error.

In order to study if differences between satellite-derived and modelled XCO_2 are from scattering related retrieval errors, the SCIAMACHY XCO_2 data set has been compared with the output of NOAA's modelling and assimilation system CarbonTracker. It has been investigated to what extent the differences between SCIAMACHY and CarbonTracker XCO_2 are temporally and spatially correlated with global aerosol and cloud data sets. For this purpose, aerosol information from the European GEMS pro-

ject and cloud information of NASA's CALIPSO satellite have been utilised.

In this analysis, significant correlations with thin clouds especially over tropical and southern hemispheric regions have been found. The maximum temporal (r^2=54%) and spatial (r^2=46%) correlations have been found for Darwin, Australia. Large temporal correlations with thin clouds have also been observed over other regions of the Southern Hemisphere (e.g. r^2=43% for South America and r^2=31% for South Africa). Over the Northern Hemisphere the temporal correlations are typically much lower. An exception is India, where large temporal correlations with clouds and aerosols have also been found. These results indicate, that the SCIAMACHY WFMDv2.1 XCO_2 data set suffers from scattering related retrieval errors caused especially by thin clouds.

In order to reduce the scattering related retrieval errors, a new version of the WFM-DOAS retrieval algorithm has been developed (WFMDv2.2), which is based on a new cloud filtering and correction method. This method is based on radiances from the 1.4 μm strong water vapour absorption and the 0.76 μm O_2-A band. The new version of the WFM-DOAS retrieval algorithm has been used to generate an improved SCIAMACHY XCO_2 data set covering the period 2003 – 2009.

The new data set has been validated using ground-based Fourier Transform Spectrometer (FTS) observations from the Total Carbon Column Observing Network (TCCON). The validation shows significant improvements of the new version WFMDv2.2 in comparison to the previous version WFMDv2.1. For instance, the standard deviation of the difference to TCCON over Darwin has been improved from 4 ppm to 2 ppm. Overall, the validation of the SCIAMACHY WFMDv2.2 XCO_2 can be summarised by a single measurement precision of 3.8 ppm, a regional scale precision of monthly averages of 1.6 ppm and an estimated regional scale relative accuracy of 0.8 ppm.

In order to investigate the differences between the new SCIAMACHY WFMDv2.2 XCO_2 data set and CarbonTracker XCO_2, a comparison between these data sets has been performed. It has been shown that the new data set agrees better with CarbonTracker than the previous version.

The new SCIAMACHY XCO_2 data set has already been used for interesting applications, for example, for an assessment of regional enhancements of atmospheric CO_2 and trends over major anthropogenic CO_2 source regions. The data set has also been used as part of the Ensemble Median Algorithm (EMMA). EMMA is a promising candidate for generating a CO_2 data set which fulfils the demanding requirements needed to obtain information on regional CO_2 surface fluxes via inversion modelling.

List of Publications

Articles in Peer-Reviewed Journals

- Heymann, J., Bovensmann, H., Buchwitz, M., Burrows, J. P., Deutscher, N. M. , Notholt, J., Rettinger, M., Reuter, M., Schneising, O., Sussmann, R. and Warneke, T.: SCIAMACHY WFM-DOAS XCO_2: reduction of scattering related errors, Atmos. Meas. Tech., 5, 2375 – 2390, 2012.

- Heymann, J., Schneising, O., Reuter, M., Buchwitz, M., Rozanov, V. V., Velazco, V. A., Bovensmann, H. and Burrows, J. P.: SCIAMACHY WFM-DOAS XCO_2: comparison with CarbonTracker XCO_2 focusing on aerosols and thin clouds, Atmos. Meas. Tech., 5, 1935 – 1952, 2012.

- Bovensmann, H., Buchwitz, M., Burrows, J. P., Reuter, M., Krings, T., Gerilowski, K., Schneising, O., Heymann, J., Tretner, A. and Erzinger, J.: A remote sensing technique for global monitoring of power plant CO_2 emissions from space and related applications, Atmos. Meas. Tech., 3, 781 – 811, 2010.

- Reuter, M., Boesch, H., Bovensmann, H., Bril, A., Buchwitz, M., Butz, A., Burrows, J. P., O'Dell, C. W., Guerlet, S., Hasekamp, O., Heymann, J., Kikuchi, N., Oshchepkov, S., Parker, R., Pfeifer, S., Schneising, O., Yokota, T. and Yoshida, Y.: A joint effort to deliver satellite retrieved atmospheric CO_2 concentrations for surface flux inversions: the ensemble median algorithm EMMA, Atmos. Chem. Phys. Discuss., 12, 23195 – 23217, 2012.

- Reuter, M., Bovensmann, H., Buchwitz, M., Burrows, J. P., Deutscher, N. M., Heymann, J., Rozanov, A., Schneising, O., Suto, H., Toon, G. C. and Warneke, T.: On the potential of the 2041 – 2047 nm spectral region for remote sensing of atmospheric CO_2 isotopologues, Journal of Quantitative Spectroscopy and Radiative Transfer, 113, 2009 – 2017, 2012.

- Reuter, M., Buchwitz, M., Schneising, O., Hase, F., Heymann, J., Guerlet, S., Cogan, A. J., Bovensmann, H., and Burrows, J. P.: A simple empirical model

estimating atmospheric CO_2 background concentrations, Atmos. Meas. Tech., 5, 1349 – 1357, 2012.

- Reuter, M., Bovensmann, H., Buchwitz, M., Burrows, J. P., Connor, B. J., Deutscher, N. M., Griffith, D. W. T., Heymann, J., Keppel-Aleks, G., Messerschmidt, J., Notholt, J., Petri, C., Robinson, J., Schneising, O., Sherlock, V., Velazco, V., Warneke, T., Wennberg, P. O. and Wunch, D.: Retrieval of atmospheric CO_2 with enhanced accuracy and precision from SCIAMACHY: Validation with FTS measurements and comparison with model results, Journal of Geophysical Research, 116, D04301, 2011.

- Reuter, M., Buchwitz, M., Schneising, O., Heymann, J., Bovensmann, H., and Burrows, J. P.: A method for improved SCIAMACHY CO_2 retrieval in the presence of optically thin clouds, Atmos. Meas. Tech., 3, 209 – 232, 2010.

- Schneising, O., Heymann, J., Buchwitz, M., Reuter, M., Bovensmann, H. and Burrows, J.P.: Anthropogenic carbon dioxide source areas observed from space: assessment of regional enhancements and trends, Atmos. Chem. Phys. Discuss., 12, 31507 – 31530, 2012.

- Schneising, O., Bergamaschi, P., Bovensmann, H., Buchwitz, M., Burrows, J. P., Deutscher, N. M., Griffith, D. W. T., Heymann, J., Macatangay, R., Messerschmidt, J., Notholt, J., Rettinger, M., Reuter, M., Sussmann, R., Velazco, V. A., Warneke, T., Wennberg, P. O. and Wunch, D.: Atmospheric greenhouse gases retrieved from SCIAMACHY: comparison to ground-based FTS measurements and model results, Atmos. Chem. Phys., 12, 1527 – 1540, 2012.

- Schneising, O., Buchwitz, M., Reuter, M., Heymann, J., Bovensmann, H., Burrows, J. P.: Long-term analysis of carbon dioxide and methane column-averaged mole fractions retrieved from SCIAMACHY, Atmos. Chem. Phys., 11, 2881 – 2892, 2011.

- Velazco, V. A., Buchwitz, M., Bovensmann, H., Reuter, M., Schneising, O., Heymann, J., Krings, T., Gerilowski, K. and Burrows, J. P.: Towards space based verification of CO_2 emissions from strong localized sources: fossil fuel power plant emissions as seen by a CarbonSat constellation, Atmos. Meas. Tech., 4, 2809 – 2822, 2011.

Selected Oral and Poster Presentations

- Heymann, J., Schneising, O., Buchwitz, M., Reuter, M., Bovensmann, H. and Burrows, J. P.: SCIAMACHY WFM-DOAS XCO_2: Improvements and comparison with FTS measurements, oral presentation given at European Geosciences Union (EGU) General Assembly 2012, 22 – 27 April 2012, Vienna, Austria, 2012.

- Heymann, J., Schneising, O., Buchwitz, M., Reuter, M., Bovensmann, H. and Burrows, J. P.: Recent improvements in SCIAMACHY WFM-DOAS XCO_2 retrievals, oral presentation given at SCIAMACHY SADDU meeting, 28 – 29 February 2012, SRON, Utrecht, The Netherlands, 2012.

- Heymann, J., Schneising, O., Reuter, M., Buchwitz, M., Rozanov, V. V., Velazco, V. A., Bovensmann, H. and Burrows, J. P.: Characterization of aerosol and cirrus cloud related errors of SCIAMACHY WFM-DOAS XCO_2 retrievals, poster presentation given at TTORCH Summer School 2011, 27 September – 4 October 2011, Hyytiälä, Finland, 2011.

- Heymann, J., Schneising, O., Reuter, M., Buchwitz, M., Rozanov, V. V., Bovensmann, H. and Burrows, J. P.: Error characterization of SCIAMACHY WFM-DOAS XCO_2: Impact of aerosols and cirrus clouds, poster presentation given at European Geoscience Union General Assembly, 3 – 8 April 2011, Vienna, Austria, 2011.

- Heymann, J., Reuter, M., Schneising, O., Buchwitz, M., Bovensmann, H. and Burrows, J. P.: Sensitivity of SCIAMACHY XCO_2 to Aerosols and Cirrus Clouds, poster presentation given at 38th COSPAR Scientific Assembly, 18 – 25 July 2010, Bremen, Germany, 2010.

- Heymann, J., Reuter, M., Schneising, O., Buchwitz, M., Bovensmann, H. and Burrows, J. P.: Sensitivity of SCIAMACHY XCO_2 to Aerosols and Cirrus Clouds, poster presentation given at EGU General Assembly 2010, 2 – 7 May 2010, Vienna, Austria, 2010.

- Heymann, J., Reuter, M., Schneising, O., Buchwitz, M., Bovensmann, H. and Burrows, J. P.: Sensitivity of SCIAMACHY XCO_2 to Aerosols and Cirrus Clouds, oral presentation given at DPG-Früjahrstagung 2010, 8 – 12 March 2010, Hannover, Germany, 2010.

Table of Contents

1 Introduction

Since the Industrial Revolution, technological, economic and social developments have resulted in the extensive combustion of fossil fuels, e.g., for heating and energy supply. This has led to an increase of the atmospheric concentration of carbon dioxide (CO_2) by about 40 % since the pre-industrial times. As CO_2 is an important greenhouse gas, the increase of its concentration causes an amplification of the greenhouse effect which leads to global warming. In order to assess global warming's adverse consequences for the life on Earth such as a rising sea level and more frequent extreme weather conditions, a reliable climate prediction is required. For this purpose, a comprehensive knowledge about the natural and anthropogenic sources and sinks of CO_2 is necessary. However, the knowledge about the sources and sinks of CO_2 has currently large gaps (e.g. Stephens et al., 2007), which cannot be closed by the very accurate but sparse surface networks of ground-based measurements (Marquis and Tans, 2008). Highly accurate and precise satellite observations of the vertical column of CO_2 or of its column-averaged dry air mole fraction, XCO_2, offer the possibility to close these gaps (Rayner and O'Brien, 2001; Houweling et al., 2004; Miller et al., 2007; Chevallier et al., 2007).

The grating spectrometer SCIAMACHY (SCanning Imaging Absorption spectroMeter of Atmospheric CHartographY) on-board ENVISAT (ESA's ENVIronmental SATellite) was a passive remote sensing satellite instrument, which observed reflected and backscattered sunlight in the ultraviolet (UV) to short wave infrared (SWIR) spectral region and provided measurements of CO_2 columns or XCO_2 with high sensitivity down to the Earth's surface. This is necessary in order to obtain information about regional CO_2 surface fluxes. For the period of mid 2002 – March 2009, SCIAMACHY was the only satellite instrument observing CO_2 with high near-surface sensitivity. The only other satellite instrument with this characteristic is the Fourier transform spectrometer TANSO (Thermal And Near infrared Sensor for carbon Observation) on-board GOSAT (Greenhouse gases Observing SATellite), which was launched in 2009. Other satellites will be launched in the future such as OCO-2 (Orbiting Carbon Observatory - 2) and possibly CarbonSat (Carbon monitoring Satellite), which have the objective to provide additional knowledge on CO_2 sources and sinks.

In order to get information on the sources and sinks of CO_2 from satellite meas-

urements, the surface flux inversion application is used. This application infers CO_2 surface fluxes from the measured information on CO_2 by consideration of the atmospheric transport. Prerequisites for this application are accurate measurements and an accurate transport model. For the measurements, not only an appropriate instrument is needed but also an appropriate retrieval algorithm, which converts the observed radiances into information on atmospheric CO_2. Among the existing algorithms is the Weighting Function Modified - Differential Optical Absorption Spectroscopy (WFM-DOAS) retrieval algorithm. This algorithm was developed to retrieve, among others, XCO_2 from SCIAMACHY measurements and was used to generate a global long-term XCO_2 data set (Schneising et al., 2011).

An important error source for satellite XCO_2 retrievals, including WFM-DOAS, are scattering due to aerosols and clouds (e.g., Aben et al., 2006; Bril et al., 2007; Reuter et al., 2010). In order to reduce scattering related errors, retrieval algorithms have been developed, which explicitly account for aerosols and clouds (Butz et al., 2009; Reuter et al., 2010; O'Dell et al., 2012; Yoshida et al., 2011; Bösch et al., 2011). These algorithms are computationally very expensive. In contrast, WFM-DOAS is a computationally very fast algorithm because it uses a look-up-table (LUT) approach that avoids time consuming on-line radiative transfer calculations. High processing speed is an important advantage especially for future satellites, such as CarbonSat, which will deliver orders of magnitude more observations than the current ones.

In this context, the objectives of this thesis are, firstly, to assess the quality of an existing SCIAMACHY XCO_2 data set focussing on the investigation of aerosol and cloud related retrieval errors and, secondly, to generate and validate a new global long-term SCIAMACHY XCO_2 data set with improved precision and accuracy suitable for geophysical exploitation. In order to achieve this goal, the following has been undertaken:

It has been investigated (i) to what extent the existing SCIAMACHY WFM-DOAS v2.1 XCO_2 data set suffers from aerosol and cloud related errors. The results of this analysis are the reason for (ii) the development of an improved WFM-DOAS retrieval algorithm, which is used (iii) to generate a more accurate and precise SCIAMACHY XCO_2 data product. (iv) This new data product has been validated against ground-based measurements in order to assess improvements in the data quality with respect to the demanding requirements and (v) has been compared with model output.

Thesis Outline

This thesis is divided into the following chapters:

- Chapter 1 provides the scientific background relevant for the topic of this thesis. This includes information about the atmosphere, the greenhouse effect, atmospheric carbon dioxide, infrared spectroscopy and other items.
- Chapter 2 presents a description of the WFM-DOAS retrieval algorithm, results of a sensitivity study of the WFM-DOAS cloud detection algorithm and information about a viewing geometry correction, which has been developed as part of this thesis.
- Chapter 3 shows results of a comparison of SCIAMACHY WFM-DOAS XCO_2 with model output. This comparison has the focus on identifying retrieval errors related to scattering by aerosols and thin clouds.
- Chapter 4 presents a description of a new version of the WFM-DOAS algorithm which is based on an improved cloud filtering and correction scheme. In addition, validation results with ground-based measurements and model comparisons are shown.
- Chapter 5 summarises the results of this thesis and conclusions are given. In addition, an overview about future work related to the WFM-DOAS retrieval algorithm is presented.
- The appendix includes additional information about the viewing geometry correction and the comparison presented in Chap. 3.

2 Scientific Background

Satellite observations of atmospheric carbon dioxide (CO_2) can significantly improve our knowledge about the sources and sinks of CO_2. However, this needs sophisticated retrieval algorithms, which are needed to extract the information on CO_2 from the measured radiances. This includes appropriate modelling of the radiative transfer. Thereby, a consideration of the basic physical principle of the interaction of molecules and larger particles is necessary. In order to obtain an overview about this scientific field and additionally motivate this work, fundamental background knowledge relevant for this thesis is given in this chapter. Starting point is an overview of the atmosphere.

2.1 The Atmosphere

The gaseous shell above the Earth's surface, the atmosphere, is held by gravitational attraction. Within the atmosphere and in interaction with the incoming solar radiation, processes are taking place which make life possible on Earth. In these processes, the constituents and the structure of the atmosphere play an essential role. A short overview of the constituents and the structure of the atmosphere follows. For more detailed information see, e.g., Goody (1995), Brasseur et al. (1999), Roedel (2000) and Burrows et al. (2011).

2.1.1 Constituents of the Atmosphere

The most abundant constituents of the atmosphere, nitrogen (N_2) and oxygen (O_2), together with the noble gases (e.g. argon (Ar), neon (Ne), helium (He)) are characterised by long lifetimes and are well mixed in the homosphere (up to 80-90 km height). Besides these gases, there are small fluid or solid particles, denoted as aerosols, clouds and a number of trace gases whose concentrations are more or less temporally and spatially variable. Trace gases are water vapour (H_2O), carbon dioxide (CO_2), nitrous oxide (N_2O), methane (CH_4) and ozone (O_3). The abundances of the most abundant components of the air are listed in Tab. 2.1. Almost all of these gases

Component	Chemical Notation	Volume Fraction in Air
Nitrogen	N_2	78.084 %
Oxygen	O_2	20.948 %
Argon	Ar	0.923 %
Carbon Dioxide	CO_2	390 ppmv
Helium	He	5.24 ppmv
Methane	CH_4	1.9 ppmv
Molecular Hydrogen	H_2	0.55 ppmv
Nitrous Oxide	N_2O	0.31 ppmv
Carbon Monoxide	CO	50-250 ppbv
Ozone (Tropospheric)	O_3	10-500 ppbv
Ozone (Stratospheric)	O_3	0.5-10 ppmv

Table 2.1: Main components, their chemical notation and their concentration in dry air. The concentrations are given in %, ppmv (parts per million per volume) and ppbv (parts per billion per volume).

are involved in important chemical and physical processes taking place in the atmosphere. CO_2, for instance, is involved in the greenhouse effect, which is described in Sec. 2.2. Other gases like CH_4 and N_2O, which are also greenhouse gases, are also directly or indirectly involved in other processes such as in the destruction of the ozone layer.

2.1.2 Structure of the Atmosphere

The vertical structure of the atmosphere is characterised by the vertical profiles of the pressure (p) and the temperature (T). The pressure is a cause of the weight of the air column above the Earth's surface and is typically 1,013 hPa at sea level. For example, Fig. 2.1 shows the pressure profile of the US standard atmosphere (Dubin et al., 1976). As can be seen, the pressure decreases with height (z), which is described for a hydrostatic and isotherm atmosphere (with geometric mean temperature $\bar{T}$) by the barometric law:

$$p(z) = p(z_0) \cdot e^{-\frac{Mgz}{R\bar{T}}}. \tag{2.1}$$

Here, M is the molar mass of air ($M \approx 29 \frac{\mathrm{g}}{\mathrm{mol}}$), g is the gravitational acceleration ($g \approx 9.81 \frac{\mathrm{m}}{\mathrm{s}^2}$) and R is the universal gas constant ($R \approx 8.31 \frac{\mathrm{J}}{\mathrm{molK}}$). This barometric law is an approximation because the temperature but also other parameters such as the gravitational acceleration are not constant with height. A consequence of the height dependent pressure is that the amount of air molecules (N) being directly propor-

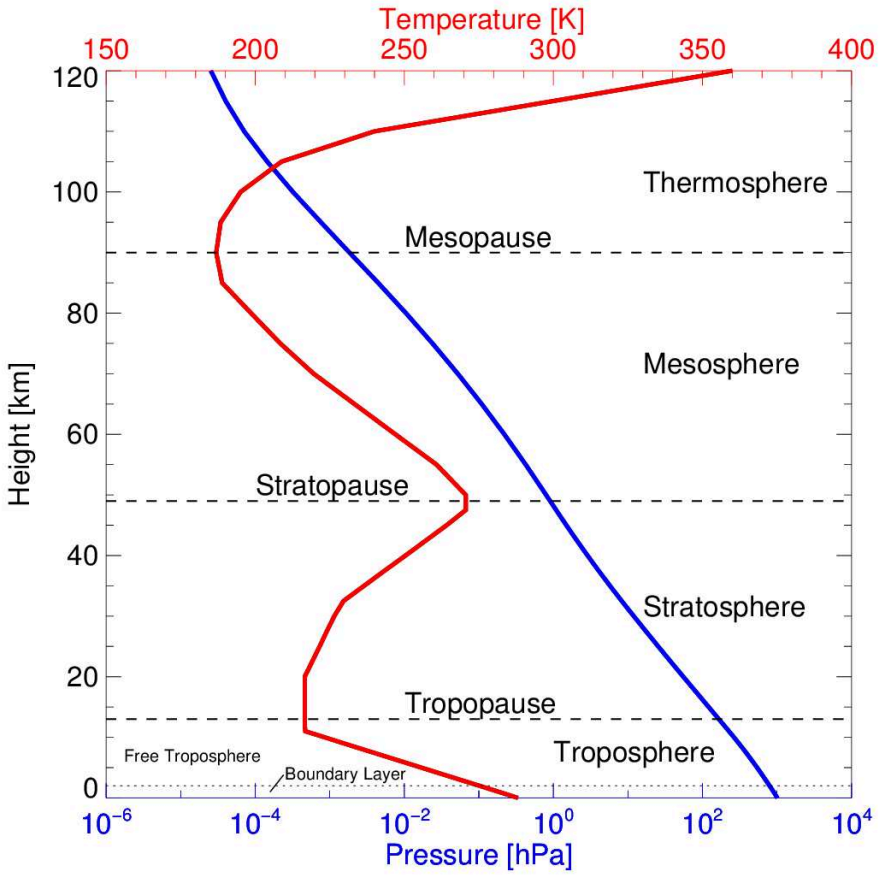

Figure 2.1: Temperature (red) and pressure (blue) profile according to the U.S. standard atmosphere.

tional to the pressure is divided in half every 5.5 km. This means, that 50 % of all air molecules are located below 5.5 km and more than 90 % are located below 20 km.

The atmosphere can be separated in several layers according to the temperature profile (e.g., Fig. 2.1). These layers are characterised in terms of their specific vertical temperature gradients.

The lowest layer of the atmosphere extends from the Earth surface to a height of about 18 km in the tropics, 12 km at mid-latitudes and 6 – 8 km near the poles and is called the troposphere. The troposphere is characterised by a negative temperature gradient, i.e., the temperature decreases with height at a rate of approximately 6.5 K/km, and has a mean temperature near the surface of about 14 °C. This temperature is achieved due to the greenhouse effect, which is described in the next section. As a result of the heating of the Earth's surface by the sun, the lower part of the tro-

posphere, the planetary boundary layer, is very unstable. Most of the atmospheric water vapour is located in this layer. Together with convection activities and vertical mixing up to the free troposphere, the higher part of the troposphere, these are responsible for the complex weather phenomena (from rainfalls to giant hurricanes). The upper boundary of the troposphere, the tropopause, is characterised by a negligible temperature gradient. The region above the tropopause and up to about 50 km is the stratosphere. The temperature gradient in the stratosphere is positive, i.e., the temperature rises with increasing height. This temperature inversion is responsible for a stable layering and a low exchange between troposphere and stratosphere. The reason for the temperature increase is the effective absorption of ultraviolet (UV) radiation in the spectral region of 30 – 200 nm by the ozone layer consisting of 90 % of the atmospheric ozone. The stratopause is the upper boundary of the stratosphere. This boundary is characterised by a maximum in ozone UV radiation absorption and a small temperature gradient. In the region above the stratopause, the mesosphere, the temperature gradient is again negative. The mesosphere is located up to 80 – 90 km height. The minimum temperature occurs at the mesopause. In the following layer, the thermosphere, the temperature increases again. The reason for this increase is the absorption of high-energetic radiation mostly by molecular oxygen. The maximum temperature in this layer depends on the level of solar activities. The thermosphere is located up to 500 – 600 km. The air particles are gravitationally separated according to their molecular or atomic weight. The change over to the interplanetary space is called the exosphere and is located up to about 1,000 km.

2.2 The Natural Greenhouse Effect

The greenhouse effect, which is responsible for a warming of the Earth's surface and the lower atmosphere, is a natural process and makes life possible on Earth. The first step in the initiation of the greenhouse effect is a heating of the Earth's surface by the sun. This heating is achieved by the incoming solar energy, which can be characterised by the solar constant. This constant is the amount of solar energy reaching the top of the Earth's atmosphere each second on an area of one square metre perpendicular to the sun direction and is about 1,368 W/m^2. The average of this value over the entire Earth is 342 W/m^2 (considering the curvature of the Earth's surface). As can be seen in Fig. 2.2, two-third of the incoming solar radiation is mostly absorbed by the surface and the atmosphere. The rest is reflected back to space. In order to achieve an energy balance, the absorbed energy is re-emitted. The maximum amount of re-emitted radiation is in the infrared spectral region according to Wien's

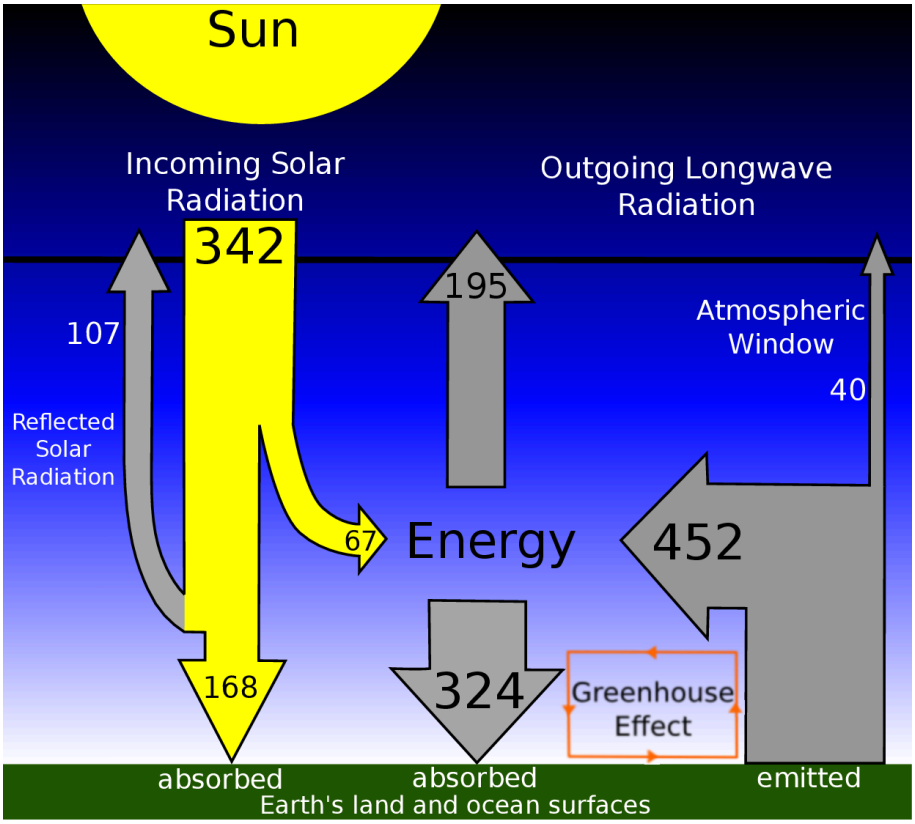

Figure 2.2: Earth's estimated energy balance. All values are given in Watts per square metre (values from Solomon et al., 2007).

law ($\lambda_{max} = b/T$, with the wavelength at maximum spectral radiant energy density λ_{max}, the Wien's constant $b = 2,897.8\mu m$ and temperature T) and the lower surface temperature of the Earth ($T_E \approx 14°C$) in comparison to the sun ($T_\odot \approx 5,800°C$). Some of the re-emitted radiation passes through the atmosphere (transmission through the atmospheric window: ~40 W/m^2), but most of it is absorbed by the greenhouse gas molecules and clouds. The absorbed radiation is again re-emitted in all directions (the so called thermal back radiation), also back to the Earth's surface. This causes a warming of the Earth's surface and of the lower parts of the atmosphere.

The greenhouse gases are characterised by an absorption of radiation in the infrared spectral region. This absorption corresponds to transitions in the vibrational and rotational energy structure of the greenhouse gas molecules (see Sec. 2.5).

The most important greenhouse gases are H_2O (responsible for 62% of the natural greenhouse effect) and CO_2(22 %). Besides these both greenhouse gases, O_3 (7%), N_2O (4 %) and CH_4 (2.5 %) contribute to the greenhouse effect (Roedel, 2000). Other important contributors to the greenhouse effect are clouds and aerosols.

Without the greenhouse gases in the atmosphere, the mean surface temperature on Earth would be about -19 °C instead of 14 °C according to the Stefan-Boltzmann-law ($I = \sigma T^4$, with the intensity I of the emitted radiation, the Stefan-Boltzmann-constant $\sigma = 5.67 \cdot 10^{-8} \frac{\mathrm{W}}{\mathrm{m^2 K^4}}$ and temperature T) (Solomon et al., 2007). Therefore, the greenhouse effect and the greenhouse gases are necessary to preserve the life on Earth. In contrast, an increase of the concentration of the greenhouse gases causes an amplification of the greenhouse effect and leads to global warming with adverse consequences for the Earth (Solomon et al., 2007). More details on the anthropogenic greenhouse effect, global warming and the resulting climate change are given in the next section.

2.3 Global Warming and Climate Change

Global warming and climate change have been in the focus of public interest for several years. Possible consequences of global warming and climate change for the human being and the possibilities of preventing these consequences have been discussed on several UN conferences on climate change. However, climate change related activities are only hesitantly resolved and realised. Since greenhouse gas emissions are responsible for global warming, a few facts about these topics are presented here, which are mostly adapted from the Intergovernmental Panel on Climate Change (IPCC) report 2007 (Solomon et al., 2007).

The term “global warming” means in this context the temperature increase near the surface since the beginning of the Industrial Revolution, i.e., the late 18th century. This is a result of an increase of greenhouse gas concentrations and an associated amplification of the greenhouse effect, which is called the anthropogenic greenhouse effect. The greenhouse gas concentrations were stable within a long period before the beginning of the industrialisation. Since the beginning of the Industrial Revolution, the concentrations have steeply increased, which is shown in Fig. 2.3 using the example of CO_2, CH_4 and N_2O. The amplification of the greenhouse effect and the resulting temperature increase cause a change in the global climate which is referred to “climate change”.

The efficiency of a greenhouse gas to trap heat in the atmosphere is given by the Global Warming Potential (GWP). This parameter considers the absorption characteristics of a greenhouse gas and their lifetime in the atmosphere. The GWP of an greenhouse gas is expressed as an equivalent mass of CO_2. Therefore, CO_2 has a GWP of 1. The atmospheric greenhouse gas CH_4 has a GWP of 25 (on a time scale of 100 years), which means, that 1 kg of CH_4 is such as efficient as 25 kg of CO_2. Other

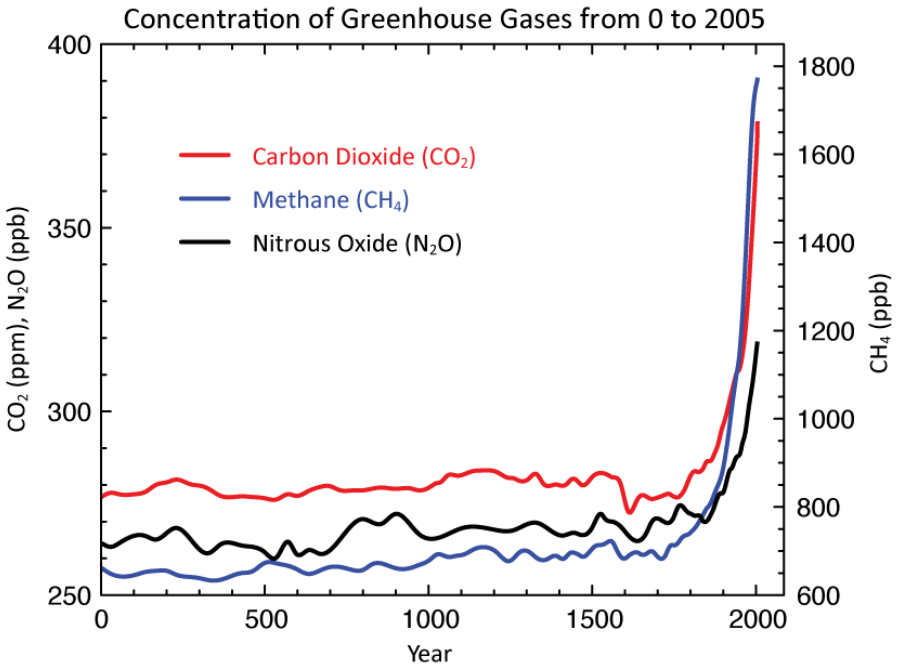

Figure 2.3: Increase of global atmospheric CO_2 (red), CH_4 (blue) and N_2O (black) concentration in the time period 0 – 2005 (obtained from ice cores, firn measurements and atmospheric measurements). The concentration of CO_2 is given in ppm and the concentrations of CH_4 and N_2O are given in ppb (adapted from Solomon et al., 2007).

greenhouse gases such as N_2O and chlorofluorocarbons (CFC) have a GWP of 298 and $\lesssim$14,400 , respectively. However, the much larger concentration of CO_2 in the atmosphere is the reason why CO_2 has a larger impact on the energy budget within the Earth's atmosphere than CH_4, N_2O and CFC.

2.3.1 Radiative Forcing and the Human Fingerprint

The individual contribution of the greenhouse gases and the other components influencing the energy budget of the Earth can be illustrated by their radiative forcings. Radiative forcing is a measure of how the energy balance between incoming solar radiation and outgoing infrared (IR) radiation within the Earth's atmosphere is changed. Radiative forcing is the rate of energy change per unit area of the globe in a time period as measured at the tropopause and is given in units Watts per square meter. If the radiative forcing is positive, the energy within the Earth's atmosphere is increased leading to a warming whereas a negative radiative forcing means a decreased energy which leads to a cooling of the system.

Figure 2.4 shows the major radiative forcings, which are given for the time period 1750 – 2005. The total net radiative forcing is composed of the following.

The natural processes which significantly contribute to the total radiative forcing are the solar activity and volcanic eruptions. However, their impact is small in comparison to human activities.

The most important greenhouse gas, water vapour, is influenced only indirectly by human activities. However, a global warming has the potential to significantly change the water vapour content of the atmosphere on a global scale. A warmer climate will lead to a larger water vapour content. A rise of 1°C in global temperature increases the water-holding capacity of the atmosphere by about 7% (Solomon et al., 2007). Another indirect influence is through methane emissions because methane is partially chemically destructed in the stratosphere. As a result, a small amount of water vapour is produced. This process results in a radiative forcing of 0.07 ± 0.05 W/m^2.

The most important anthropogenic greenhouse gas is carbon dioxide with the largest radiative forcing (1.66 ± 0.17 W/m^2) resulting from the rise of the atmospheric CO_2 concentration (shown by Fig. 2.3) mostly due to fossil fuel combustion, cement production and deforestation. A more detailed overview of atmospheric carbon dioxide and its sources and sinks can be found in the next section.

The atmospheric CH_4 concentration (second most important anthropogenic greenhouse gas) has also been increased from a nearly constant concentration of 720 ppb for pre-industrial times to more than 1,800 ppb (as shown by Fig. 2.3). After a period of a stabilised CH_4 concentration in the period between 1999 – 2006 (Bousquet et al., 2006), a renewed methane increase has been detected (see, e.g., Schneising et al., 2011). CH_4 contributes with 0.48 ± 0.05 W/m^2 to the total radiative forcing and is released from agriculture (mostly from rice fields and livestock farming), natural gas exploitation and transportation and landfills. CH_4 is not only released due to human activities, but also due to natural processes which take place, e.g., in wetlands.

The N_2O concentration has been increased from 270 ppb to more than 319 ppb since the pre-industrial times (see Fig. 2.3) mainly as a result of the use of fertilisers in the agriculture and livestock farming. N_2O contributes with 0.16 ± 0.05 W/m^2 to the total radiative forcing.

The concentrations of other greenhouse gases like ozone and halocarbon gases (including the third most important anthropogenic greenhouse gas CFC-12) have been increased mainly or only due to human activities. The increased ozone concentration in the troposphere results in a positive radiative forcing of about 0.35 W/m^2. In the stratosphere, the rise of the halocarbon gases including the chlorofluorocarbons caused a destruction of ozone, which resulted in the ozone hole over the Antarctica. Stratospheric ozone results in a small negative radiative forcing of

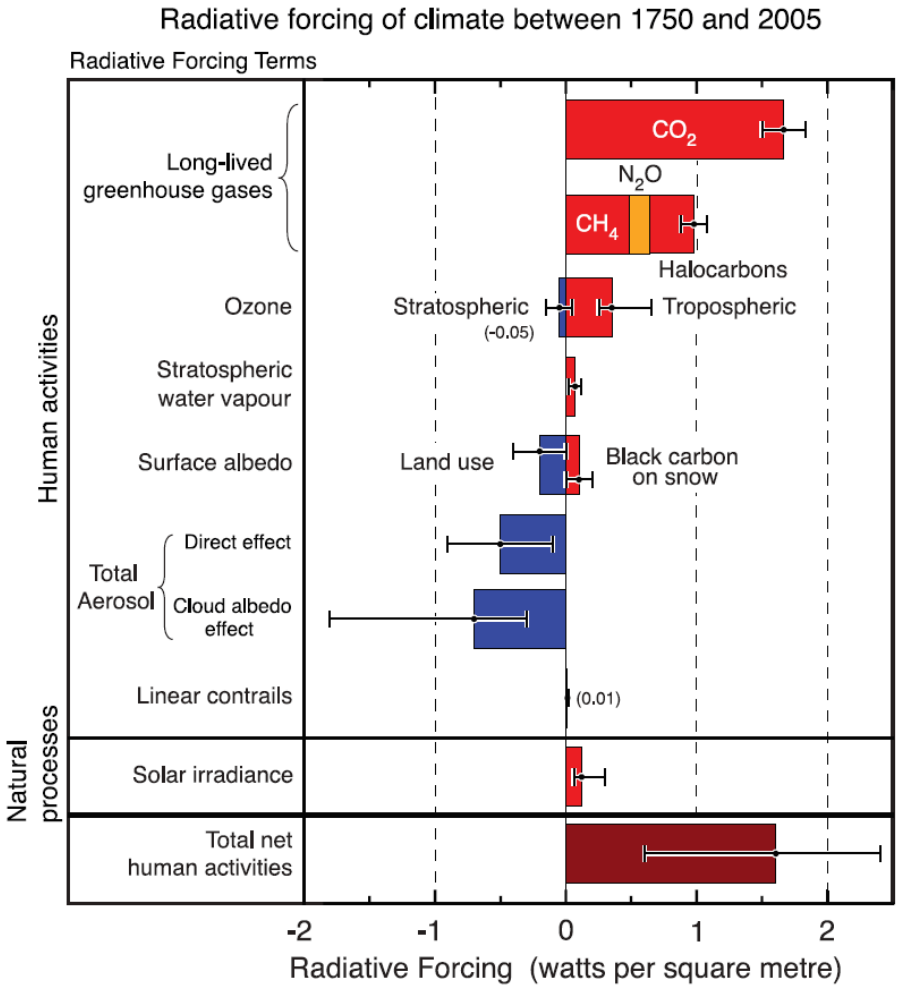

Figure 2.4: Radiative forcings and their uncertainties between 1750 and 2005. Red, orange and brown radiative forcings are positive and blue forcings are negative. The forcings are divided into human activities and natural processes. The sum of all forcings are the total net radiative forcing (from Solomon et al., 2007).

-0.05 ± 0.10 W/m^2. However, international regularisations are the reason why the concentrations of the chlorofluorocarbons are decreasing.

The amount of aerosols has also been increased due to fossil fuel and biomass burning, surface mining and other industrial processes. Aerosols have a direct shielding effect on the radiation, which causes a negative forcing (-0.5 ± 0.4 W/m^2). They indirectly affect, e.g., the cloud albedo. This leads to a negative forcing of about -0.7 W/m^2. However, due to the large temporal and spatial variability and the limited knowledge of the formation and annihilation processes of aerosols, the radiative forcings are highly uncertain.

The albedo has also an impact on the radiative forcing. Land cover changes (-0.2 ± 0.2 W/m^2) and black carbon (soot) on snow (0.1 ± 0.1 W/m^2), which reduces the albedo by absorbing more sunlight, contribute to the total forcing. In addition, contrails from the air traffic contribute to global warming with a forcing of about 0.01 W/m^2.

These forcings sum up to a total net radiative forcing of about 1.6 W/m^2 (between 0.6 and 2.4 W/m^2). This positive total net forcing indicates a rise of the amount of energy in the atmosphere which causes global warming.

In order to investigate if the anthropogenic forcings are the reason for global warming, climate simulations for several regions were performed with and without these forcings (Solomon et al., 2007). Figure 2.5 shows the results of these simulations. A good agreement with the observation can only be found for the simulations with considered anthropogenic forcings. This agreement considerably shows the human fingerprint on the global warming.

2.3.2 The Observed Consequences

At this stage, consequences of global warming can already be seen. As a result of increasing greenhouse gas concentrations and a resulting positive net radiative forcing, the global temperature has increased by 0.35°C between 1910 to 1940 and by 0.55°C between 1970 to the present. In addition, the occurrence of warm years has increased. 11 of the 12 warmest years on record had occurred in the period 1995 to 2006 (Solomon et al., 2007).

As a result, the Arctic sea ice amount has been decreased by 2.7 ± 0.6 % per decade, in summer by 7.4 ± 2.4 % per decade. In addition, many mountain glaciers and ice caps have melted. Overall, these melting processes lead to a sea level rise of approximately 1.2 ± 0.4 mm/yr for the period between 1993 to 2003. Together with the thermal expansion of the oceans, due to the fact that water expands as it is warmer, the sea level has risen at a rate of around 3 mm/yr (Solomon et al., 2007).

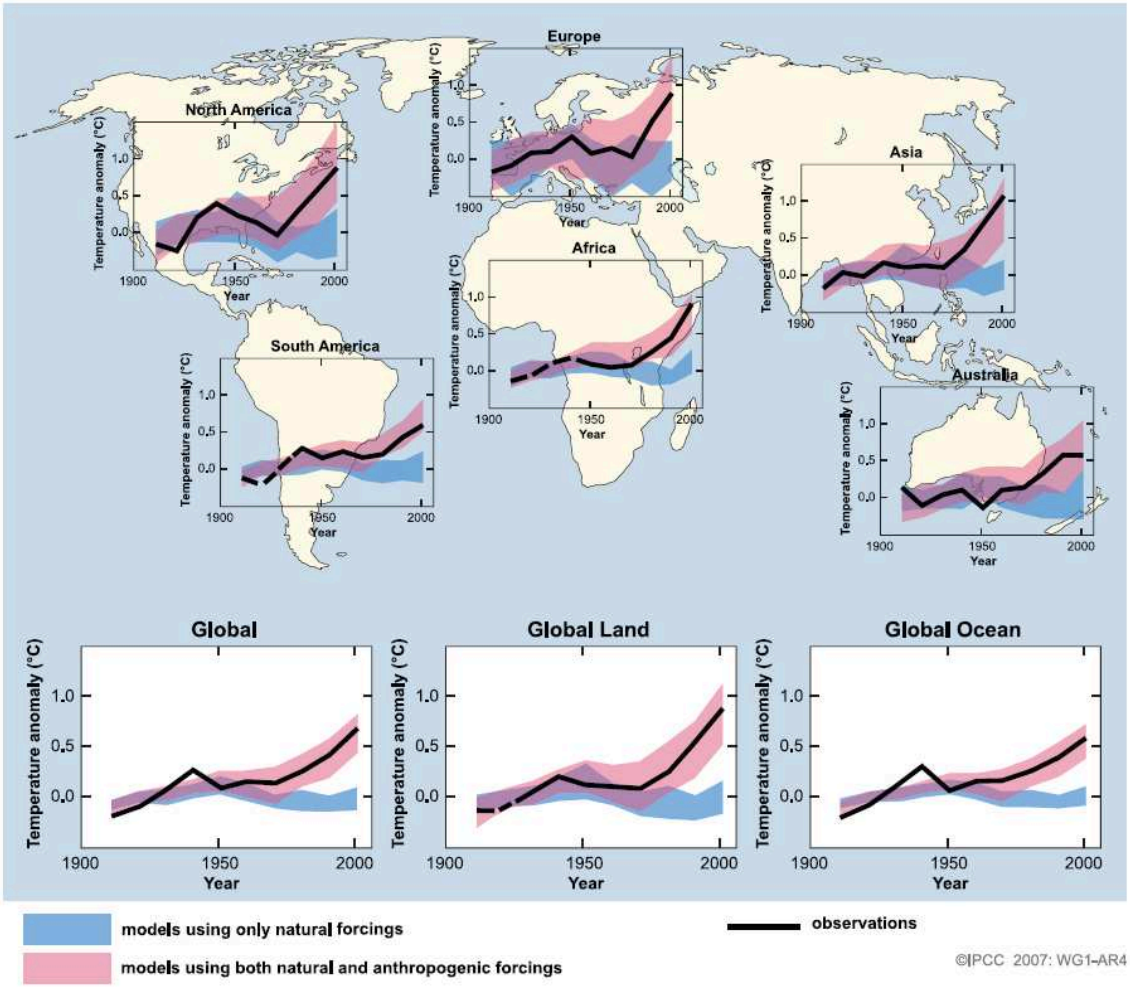

Figure 2.5: Comparison of simulations and observations of temperature changes for several regions. The simulations have been performed with (red) and without (blue) anthropogenic forcings. The temperature anomalies correspond to the mean temperature in the time period 1901 – 1950 and are given per decade. The dashed line are decades with just a few observations (from Solomon et al., 2007).

Besides the melting processes and the rising sea level, the occurrence of heavy precipitation events and floods has increased in some regions. However, in some other regions the occurrence of droughts has increased. In addition, there is evidence, that intensity and duration of tropical storms and hurricanes have increased since the 1970s, but the frequency considerably varies from year to year (Solomon et al., 2007).

2.3.3 Future Projections

One of the most important questions related to climate change is the possible future evolution of the climate and its consequences. Therefore, the future climate (2000 – 2100) has been projected with different models and emission scenarios. The emission scenarios are based on the Special Report on Emission Scenarios (SRES) of the IPCC (Nakićenović and Swart, 2000). These scenarios (A1B, A1FI, A1T, A2, B1, B2) are based on different demographic, socio-economic and technological developments. Every scenario has its own storyline which is coupled to different emission estimates. For instance, the A2 scenario described a heterogeneous world with a regional oriented economic and social development. The global economic growth and the development and the exchange of clean and resource-efficient technologies is rather slow. In addition, an increasing global population is assumed.

As can be seen by Fig. 2.6 the projections show a more or less strong increase of the concentration of the greenhouse gases CO_2 and N_2O. For methane, some scenarios show a decreasing concentration. However, the radiative forcings and also the global mean temperature increase. A comparison of the global mean temperature between the periods 2090 to 2099 and 1980 to 1999 shows a temperature increase in a range of 1.1°C to 6.4°C. This temperature increase has significant consequences for the mankind such as a sea level rise between the periods of 1980 to 1999 and 2090 to 2099 of 0.18 to 0.59 m, a higher occurrence of intense heat waves and droughts and an increase of precipitation but with longer time between rainfall events (Solomon et al., 2007).

The possible consequences show how important reliable climate predictions are. However, in order to have better assessments of the future climate, a profound knowledge of the sources and sinks of the greenhouse gases are necessary. Especially the knowledge on the sources and sinks of CO_2 as the most important greenhouse gas with the largest radiative forcing has large gaps. This is further clarified in the next section.

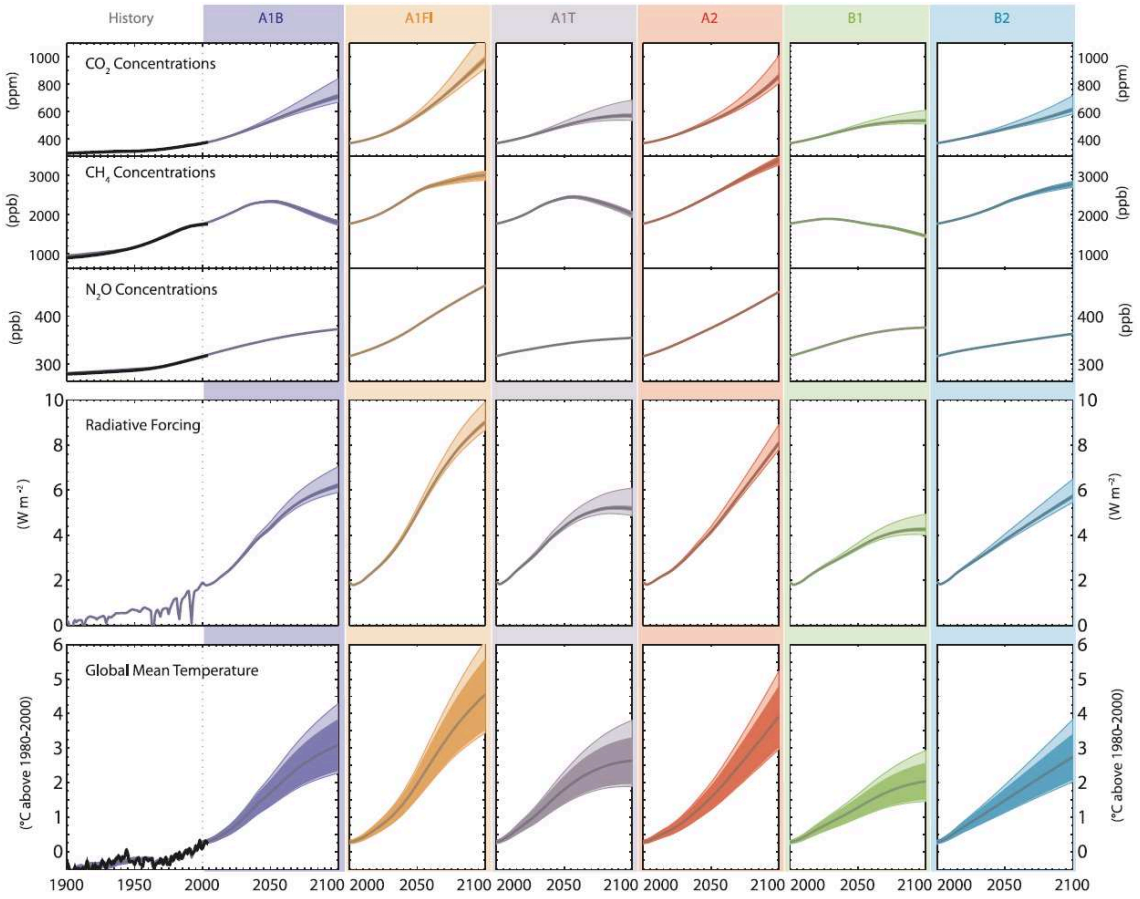

Figure 2.6: Projections of the concentration of CO_2, CH_4 and N_2O, total radiative forcing and the global mean temperature between 1900 and 2100 based on the SRES emission scenarios (A1B, A1FI, A1T, A2, B1, B2). (from Solomon et al., 2007)

2.4 Atmospheric Carbon Dioxide

Carbon dioxide (CO_2) is an inodorous and transparent gas, which mainly originates in the atmosphere from combustion processes. The CO_2 molecule consists of two oxygen atoms and a carbon atom and is chemically inert. Due to its optical characteristics, CO_2 is an important atmospheric gas. It is an effective thermal infrared (IR) radiation absorber and belongs to the greenhouse gases. In the past 200,000 years, the global atmospheric carbon dioxide concentration varied between 200 and 280 ppm. Since the mid-19th century, with the beginning of the industrial era, the CO_2 concentration has been increased by about 40% and reached approximately 390 ppm today. This increase and the effectiveness in IR radiation absorption are the main reason,

that CO_2 is the most important anthropogenic greenhouse gas.

The following sections aim at giving an overview about the current state of research in terms of atmospheric carbon dioxide, which includes information about important but still open scientific questions and an overview about measurement methods.

2.4.1 The Carbon Cycle

The exchange of carbon between the Earth's main reservoirs, namely the atmosphere, the land and the ocean is called the carbon cycle. Carbon means in this context all chemical carbon species occurring in the atmosphere, ocean and land. The main carbon species in the atmosphere are CO_2 and CH_4. However, in comparison to CO_2, CH_4 has a much lower concentration in the atmosphere. The carbon exchange between atmosphere – land and between atmosphere – ocean are in the main focus of this subsection.

An important parameter is the carbon flux, which is the amount of carbon exchanged between the reservoirs in a time period and is given in peta gram carbon per year (PgC/yr) or in the equivalent giga tons carbon per year (GtC/yr). Depending on the direction of the flux, the process responsible for the exchange is a source or a sink of carbon.

The sources and sinks of carbon and the reservoir sizes are shown in Fig 2.7. The net exchange between the main reservoirs are relatively small compared to the sizes of the carbon reservoirs. The main carbon reservoir are rocks. However, they are not important in the context of climate change. Therefore, they are not shown in Fig 2.7. The reason for this is that the exchange with the atmosphere is only slow (on a time scale of >1 Myr) and therefore plays only a minor role in time scales of centuries to millennia.

The ocean stores about 38,000 PgC dissolved inorganic carbon and about 3 PgC within organic biomass. The dissolving of the atmospheric CO_2 occurs in the ocean surface water due to different partial pressures of CO_2 in ocean and atmosphere. The solubility of CO_2 in water depends on the temperature, the degree of saturation and also on the wind speed. The dependencies of the solubility of CO_2 and biogenic activities are the reason why in some regions the ocean becomes a source and in other regions the ocean becomes a sink. However, as can be seen by the net flux (-1.6 PgC/yr) of the exchange of carbon between the ocean and the atmosphere, the ocean is a small net-sink. The transfer of the dissolved carbon into the deep ocean is due to the ocean circulation and the organic pump (the transport of carbon stored in extinct organic material to the sea ground). The dissolved CO_2 also reacts with the water to carbonic acid, which also can be found, e.g., in some soft drinks. The chemical

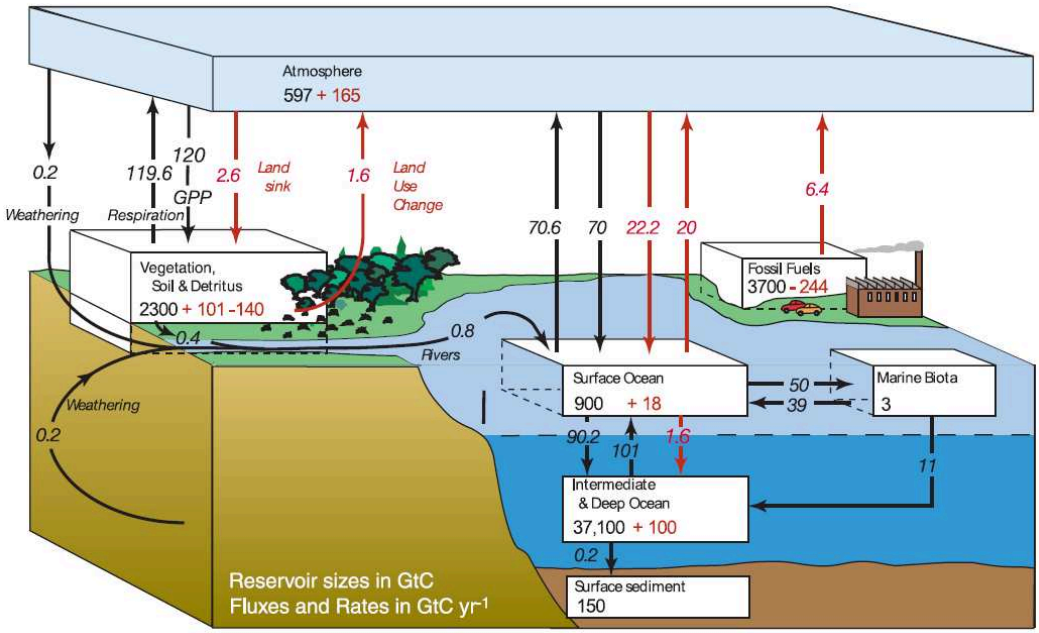

Figure 2.7: Global carbon cycle in the 1990's. The black lines and numbers indicate natural carbon fluxes and the red lines and numbers are the anthropogenic fluxes given in GtC/yr. Carbon reservoir sizes and the anthropogenic contribution are in the white boxes and given in GtC. GPP is the gross primary production (from Solomon et al., 2007).

reactions are the following:

$$CO_2^{aq} + H_2O \leftrightarrow H_2CO_3 \tag{2.2}$$

$$H_2CO_3 + H_2O \leftrightarrow HCO_3^- + H_3O^+ \tag{2.3}$$

$$HCO_3^- + H_2O \leftrightarrow CO_3^{2-} + H_3O^+ \tag{2.4}$$

These processes are in a chemical equilibrium. The originating H_3O^+ ions are the reason for an acidification of the ocean. Currently the ocean is slightly alkaline, but an increase of atmospheric CO_2 results in an increase of oceanic CO_2, which leads to a stronger acidification of the ocean. The consequences of this are not well known (Caldeira and Wickett, 2003).

The land stores ~2,250 PgC carbon in soils and biosphere. The main reason for the carbon uptake over land is the photosynthesis by the land biosphere. This means, that in the presence of light, carbon dioxide and water are transformed to organic matter (Glucose) and oxygen. Photosynthesis is a complex process and depends on

temperature, precipitation and the plant species. Therefore, the atmospheric carbon dioxide concentration depends on the vegetation. In the spring months shortly before the growing season starts, the atmospheric CO_2 concentration is high (e.g., April in the Northern Hemisphere) and at the end of the summer (e.g., August) the concentration is low. This temporal characteristic is called the seasonal cycle. The net chemical equation for the photosynthesis is the following:

$$6H_2O + 6CO_2 + h\nu \rightarrow C_6H_{12}O_6 + 6O_2 \tag{2.5}$$

The amount of carbon which is dissipated by photosynthesis and other processes is called the Gross Primary Production (GPP) and accounts for a flux of 120 PgC/yr. The largest land source is respiration by land vegetation, animals and human beings. This process transforms the organic matter and oxygen back into carbon dioxide, water and energy. The Net Primary Production (NPP) is the GPP minus the respiration from plants (approximately 50% of the flux for respiration shown in Fig. 2.7) and amounts to 60 PgC/yr.

In pre-industrial times, the atmosphere stored about 600 PgC. However, due to the anthropogenic sources, the atmospheric reservoir has been increased to about 750 PgC. Figure 2.7 shows that in the 1990's, the anthropogenic carbon fluxes are 6.4 PgC/yr for fossil fuel combustion and cement production and 1.6 PgC/yr for land-use change. In the period 2000 – 2006, the carbon flux from fossil fuel combustion was increased to a value of 7.6 PgC/yr (Canadell et al., 2007). The flux from land-use change is nearly stable and is 1.5 PgC/yr during this period. The net-fluxes from the natural sinks are -2.8 PgC/yr from land and -2.2 PgC/yr from ocean (Canadell et al., 2007). These fluxes show that an amount of 4.1 PgC/yr are accumulated in the atmosphere. This means, that about 50 % of the anthropogenic emissions are absorbed by the biosphere and the oceans, the rest remains in the atmosphere.

2.4.2 Open Scientific Questions

In order to evaluate the consequences of global warming and the future climate, a reliable future climate prediction is necessary. A profound knowledge about the sources and sinks of CO_2 is essential for these predictions, e.g., to assess changes in the carbon cycle response to climate change. However, there are important but still open questions about the sources and sinks of CO_2 which have to be answered.

For instance, the atmospheric CO_2 growth rate is subject to large year-to-year fluctuations while the fossil fuel emission increases very monotonic as seen in Fig. 2.8. The mechanism which control these large year-to-year variations and the real strength of the sinks are poorly understood (Crisp et al., 2009 and references given

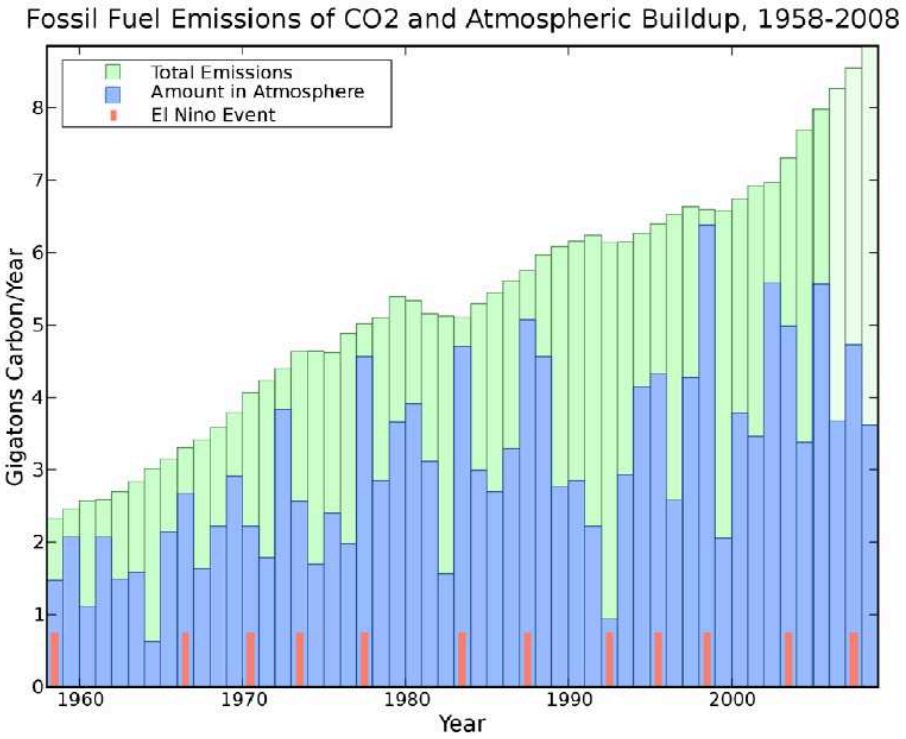

Figure 2.8: Comparison of global average carbon emissions from fossil fuel combustion (green) and yearly atmospheric CO_2 growth rate (blue) between 1958 and 2008 (from Crisp et al., 2009).

therein).

Figure 2.9 shows the simulated global atmospheric CO_2 concentration between 1850 and 2100 from 11 different models (A description of the models and their differences can be found in the publication of Friedlingstein et al., 2006). All of theses models use the same emission scenario, the same historical emissions and the SRES A2 scenario. As can be seen, the predicted atmospheric CO_2 concentration in the year 2100 is highly uncertain. The models predict concentrations to be in the range between 700 ppm and 1,000 ppm. This indicates that the efficiency and the possible evolution in times of climate change of the CO_2 sinks is not well known. Changes in wind pattern can alter the exchange rates between atmosphere and ocean or changes in the surface temperature can modify the solubility of CO_2 in the ocean. For the land sinks, also changes in the temperature affect the efficiency of the photosynthesis and has implications for the CO_2 storage (Solomon et al., 2007). Large amounts of carbon can be released, e.g., from peat-lands in response to global warming (Brasseur et al., 1999).

In addition, the processes behind the carbon uptake by the terrestrial biosphere

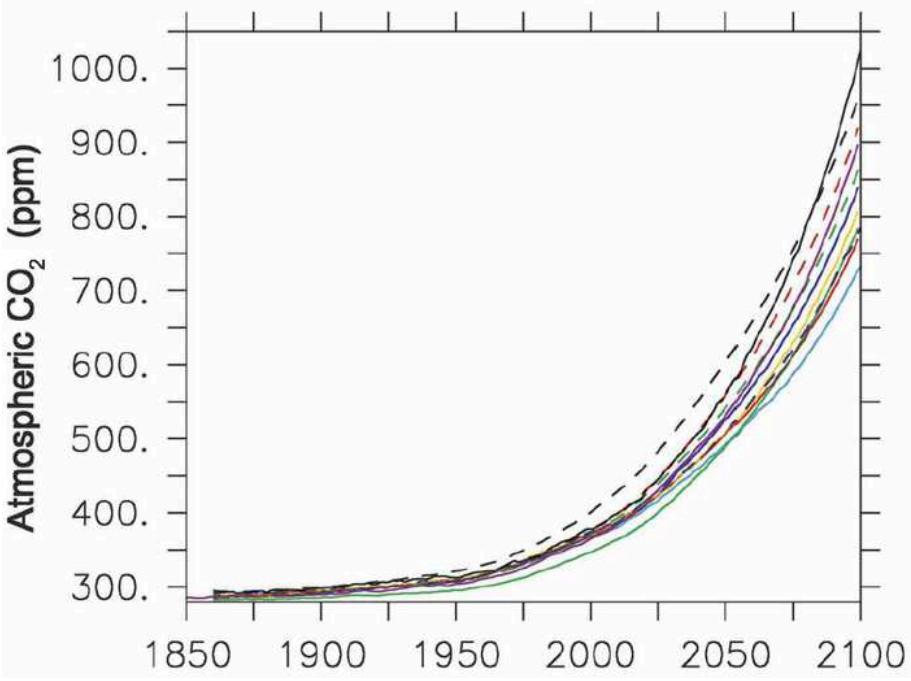

Figure 2.9: Projections of atmospheric CO_2 concentration between 1850 and 2100. Results are obtained from simulations with 11 different models all using the same emission scenario SRES A2 (from Friedlingstein et al., 2006).

and the oceans are not fully understood and the question about an "unidentified" or "missing" CO_2 sink is still not clarified. This missing carbon sink accounts for 15 % to 30 % or more of the annual anthropogenic carbon emissions (Myneni et al., 2001; Field, 2001; Pregitzer et al., 2008).

The year-to-year variations, the uncertain model results and the other open questions show that the sizes and distribution of the anthropogenic, but especially the natural sources and sinks of CO_2 and their temporal and spatial variability is not yet well understood. Therefore, it is necessary to improve this knowledge. This can be achieved by more accurate and precise measurements and surface flux inversion models, which is the method used to obtain information on the sources and sinks of CO_2 from the measurements.

2.4.3 Atmospheric CO_2 Measurements

Carbon dioxide is a long-lived trace gas. Therefore, the background CO_2 concentration in the atmosphere is large and the variations due to the sources and sinks of CO_2 are very small compared to the background ($\sim 1\,\%$). For this reason, a high accuracy

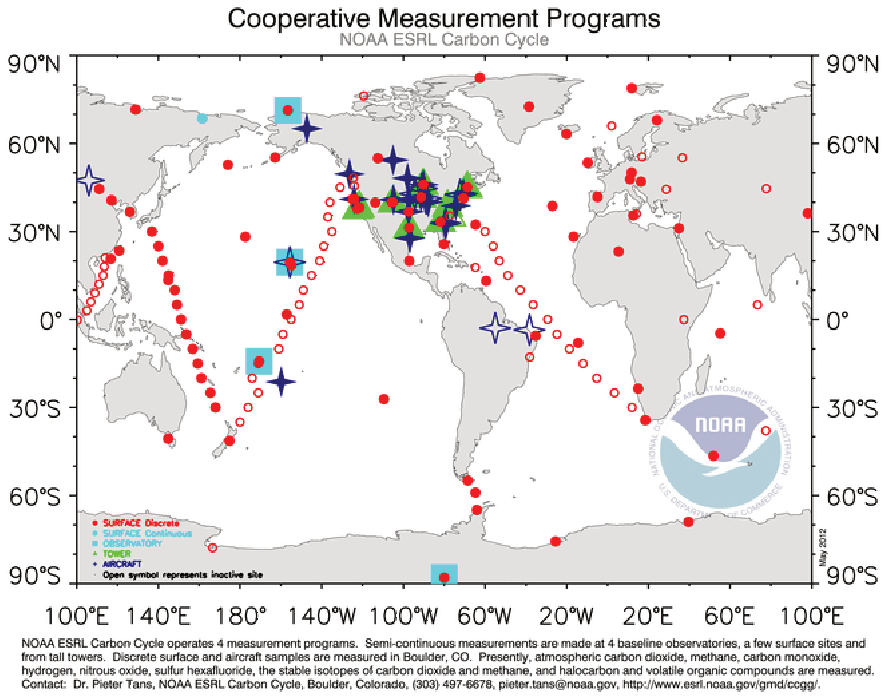

Figure 2.10: NOAA's greenhouse gas air sampling network (from http:\\www.esrl.noaa.gov).

for the measurements of CO_2 concentrations is required.

There are several instruments which permit accurate and precise measurements of atmospheric CO_2 and are more or less suitable for the observation of CO_2's global sources and sinks. There are two main groups of these instruments namely in-situ and remote sensing instruments.

In-situ instruments measure within the investigated medium or are based on analysing air samples in the laboratory. Examples of these instruments are mass spectrometer and laser spectrometer, which are used for measurements from ground, tall towers and air planes. In order to obtain information about global atmospheric CO_2 concentrations, the greenhouse gas air sampling network of NOAA (National Oceanic and Atmospheric Administration of the United States) has been established (shown in Fig. 2.10). These measurements are very accurate and precise. However, large parts of the Earth, e.g. Southern America, East Asia, Australia and Africa remain unobserved.

The other group of instruments are remote sensing instruments, which radiomet-

rically observe the investigated medium from some distance. Examples of passive remote sensing instruments are grating spectrometers and Fourier transform spectrometers (FTS). An example of an active remote sensing instrument is a LIDAR (LIght Detection And Ranging). The passive remote sensing satellite instruments have typically a large temporal and spatial coverage. SCIAMACHY on-board ENVISAT and TANSO on-board GOSAT are two examples of such satellite instruments. These two satellite instruments have also a high sensitivity down to the Earth's surface where the sources and sinks of CO_2 are located. This is important in order to improve the knowledge of the sources and sinks of CO_2.

Remote sensing instruments are also used for ground-based measurements. A network of ground-based FTS stations have been established in the last years and is incorporated under the name TCCON (Total Carbon Column Observing Network) (Wunch et al., 2011). The measurements of the FTS instruments correspond to the total CO_2 column such as the satellite measurements. Therefore, this measurements are useful for the validation of the satellite measurements. More about the TCCON network can be found in Sec. 5.3.1 and e.g., in the publication of Wunch et al. (2011).

It is also possible to measure different CO_2 isotopologues. These observations can provide additional information about the sources and sinks of CO_2. The primary C^{12} ($^{16}O^{12}C^{16}O$) and secondary C^{13} ($^{16}O^{13}C^{16}O$) carbon dioxide isotopologues have a natural abundance in the air of about 98.4 % and 1.1 %, respectively. Plants prefer C^{12} for the photosynthesis. This results in a relative enrichment of C^{13} in the ambient air. In addition, one would expect an enrichment of C^{12} in the amount of CO_2 which is generated during the combustion of fossil fuel as plants are a source of fossil fuel. The potential to measure CO_2 isotopologues from space is discussed by Reuter et al. (2012a).

The basic concept behind most of the measurement method to measure CO_2 concentrations is the infrared spectroscopy, which is described in the next section.

2.5 Infrared Spectroscopy

The absorption of electromagnetic radiation by molecules in the atmosphere is an important physical process, which is for instance the physical basis of the greenhouse effect. The spectroscopic atmospheric observation of infrared (IR) radiation in the spectral region of these molecular absorptions gives information on the species and the amount of these molecules in the atmosphere. Here only a brief overview of this topic is given. More details can be found in the textbooks of Barrow (1962), Herzberg (1973) and Haken and Wolf (2006).

The molecular absorptions of O_2 and CO_2 (both are important for this work) are located in the near and short wave infrared spectral region. The near infrared region (NIR) is located between 0.75 – 1.4 µm. In this region, the O_2-A band is located at 755 – 775 nm. The short wave infrared (SWIR) is situated between 1.4 – 3 µm. Here, the used CO_2 absorption lines are located at 1558 – 1594 nm. The thermal infrared region is located at longer wavelength (> 3µm).

As presented in Sec. 2.2, the gas molecules in an atmospheric layer partly absorb the incoming thermal radiation from the Earth surface (which was heated by the sun) resulting in a heating of this layer. The absorption of the gas molecules results in absorption lines in the spectra of the outgoing radiation. These absorption lines are due to energy transitions in the molecules. The energy transitions are described by the wavelength and the depth of the lines are described by the cross sections and the concentration of the corresponding gas. Cross sections are temperature and pressure dependent quantities and illustrate the efficiency of absorptions at a given wavelength. These quantities are utilised in order to describe the radiative transfer through the atmosphere.

The quantum-mechanical description of the absorption of electromagnetic radiation is provided by Schrödinger's equation:

$$i\hbar\frac{\partial}{\partial t}\boldsymbol{\psi} = \hat{H}\boldsymbol{\psi}. \tag{2.6}$$

Here, i is the imaginary unit, $\hbar = \frac{h}{2\pi}$, h is the Plank's constant, $\boldsymbol{\psi}$ is the wave function of the quantum system and $\hat{H}$ is the Hamiltonian operator. The excitation energies of the transitions are determined by the energy values of the Hamilton operator and is given by a sum of different transition energies:

$$E = E_{\text{rot}} + E_{\text{vib}} + E_{\text{el}}. \tag{2.7}$$

Transitions within a molecule can be rotations (rot), vibrations (vib) and electronic transitions (el).

The number of fundamental rotational and the vibrational transitions depends on the number of atoms in the molecule and the molecular structure. The amount of possible fundamental movement patterns are given by the degree of freedom. In 3-dimensional space, each position of an atom in a molecule is determined by 3 coordinates. The resulting value of 3n coordinates is the degree of freedom. The constant n is the amount of atoms in the given molecule. A molecule has 3 translational, 3 rotational (2 for symmetric molecules) and 3n-6 vibrational (3n-5 for symmetric molecules) degrees of freedom.

2.5.1 Rotational Transitions

Rotational transitions are between different rotational energy levels. They can be found in the microwave and far infrared spectral region. A molecule rotates around the molecule's main axis (A,B,C). The three principal moments of inertia (I_A,I_B,I_C) can be used for a characterisation of a molecule. Three classes of molecules with rotational spectrum can be found: the linear ($I_A \ll I_B = I_C$), the symmetric-top ($I_A \neq I_B = I_C$) and the asymmetric-top ($I_A \neq I_B \neq I_C$). However, a prerequisite for observing rotational spectra is that the molecule has a permanent or oscillating dipole moment. The energy of a rotational level in the rigid rotor approximation is given by

$$E_{\text{rot}} = \frac{\hbar}{2\Theta} \cdot J(J+1). \tag{2.8}$$

Here, Θ is the inertia momentum of the molecule, and J is the orbital quantum number. The selection rule for a rotational transition is $\Delta J = \pm 1$.

The molecular rotational energy levels are populated in thermal equilibrium for a given temperature (T) according to the Boltzmann distribution:

$$\frac{N_J}{N_0} = \frac{g_J}{g_0} exp(-\frac{E_J - E_0}{k_B T}). \tag{2.9}$$

Here, E_J is the J-th energy level and E_0 is the energy of the ground level. N_0 is the population of the ground level, N_J is the population of the J-th energy level, g_J and g_0 are the degeneracies of the energy levels, which are the number of states having the same energy, and k_B is the Boltzmann constant.

2.5.2 Vibrational Transitions

Vibrational transitions are transitions between different vibrational energy levels and can be found in the infrared spectral region. The energy of vibrational transitions in the harmonic oscillator approximation is given by

$$E_{\text{vib}} = \hbar\omega(v + \frac{1}{2}). \tag{2.10}$$

Here, ω is the vibrational frequency and v is the vibrational quantum number.

Together with vibrational levels, rotational levels always exist and form an absorption band. This absorption band can be classified as a parallel or perpendicular band. For a linear molecule such as CO_2, the parallel band means that the oscillating dipole moment is parallel to the linear axis (z-axis) and the perpendicular band means that the oscillating dipole moment is perpendicular to the linear axis (in the xy-plane).

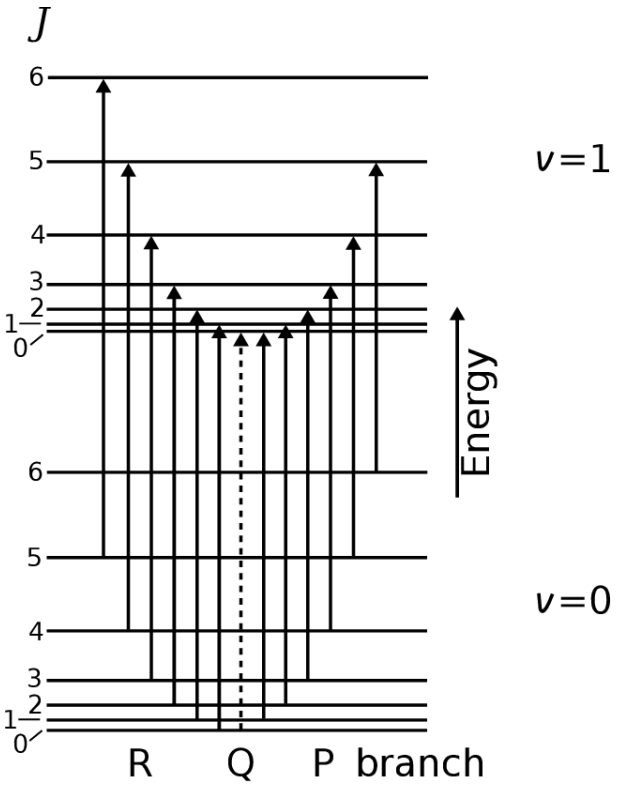

Figure 2.11: Energy level diagram and transitions of a linear chain molecule such as CO_2. Shown are the rotational transitions between the vibrational ground state ($v = 0$) and the exited state ($v = 1$). The dashed line shows the transition $v = 0$, $J = 0 \rightarrow v = 1$, $J = 0$ and corresponds to the Q branch.

The selection rules for a parallel band are $\Delta v = \pm 1$ and $\Delta J = \pm 1$ and for a perpendicular band are $\Delta v = \pm 1$ and $\Delta J = 0, \pm 1$. Overtones of vibrational transitions with lower intensities are also possible for $\Delta v = \pm 2, \pm 3, ...$

An example of a vibrational rotational transition is shown in Fig. 2.11 in which transitions between two vibrational levels within a CO_2 like molecule can be seen. The rotational structure of vibrational bands is divided in three different branches. The P branch originates from transitions with $\Delta J = -1$ and is located at longer wavelengths. The separation of the lines in the P branch increases with increasing wavelength. The R branch corresponds to rotational transitions with rotational quantum number changes of $\Delta J = +1$ and is located at smaller wavelengths. The separation of the lines decreases with increasing wavelength. The Q branch exist only for pure vibrational transitions which means that $\Delta J = 0$. The existence of the Q branch depends on the molecular symmetry.

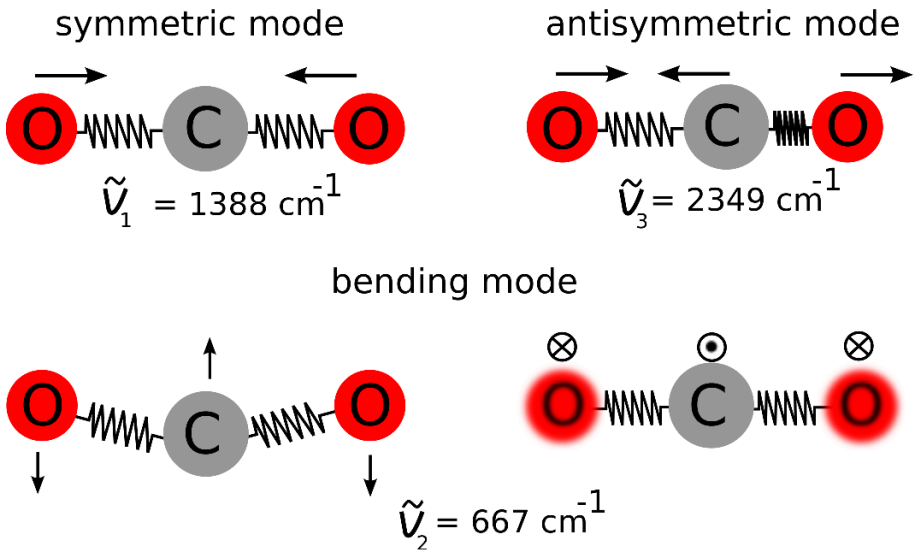

Figure 2.12: Fundamental vibration modes of CO_2. The bending mode is doubly degenerated.

For instance, carbon dioxide is a molecule which consists of two oxygen atoms and one carbon atom (n=3), which are grouped in a linear chain. The mean distance between the carbon and one oxygen atom is about 116.3 pm. The CO_2 molecule is a symmetric-top molecule and has 4 fundamental vibrational states (3 translational, 2 rotational and 3n-5=4 vibrational degrees of freedom). The symmetric and antisymmetric stretch and the bending mode, which is doubly degenerated, are shown in Fig. 2.12. The bending mode correspond to a perpendicular band. The transitions of the bending modes can be found at larger wavelengths than the transitions of the symmetric and antisymmetric stretch modes. In addition, a Q branch can be found for this transition. The ground state of the bending mode can be found at $\tilde{\nu}_2$ =667 cm^{-1} (λ_2 = 14,992 nm). The non-degenerated symmetric and antisymmetric stretch modes are parallel bands. Their ground states are at $\tilde{\nu}_1$ =1,388 cm^{-1} (λ_1 = 7,474 nm) and $\tilde{\nu}_3$ =2,349 cm^{-1} (λ_3 = 4,257 nm), respectively. The symmetric stretch mode is not infrared active because there is no permanent or vibrating dipole moment. The CO_2 absorption band used for the retrieval of atmospheric CO_2 information from SCIAMACHY measurements is located at 6,348 cm^{-1} (1,575 nm). This absorption band is a combination of the antisymmetric stretching mode $\tilde{\nu}_3$ and overtones of $\tilde{\nu}_1$ and $\tilde{\nu}_2$.

2.5.3 Electronic Transitions

The electronic transitions are transitions between rotational and vibrational levels of different electronic energy levels. Electronic transitions can be found in the near infrared, visible and ultraviolet region. For instance, the O_2-A band (at 762 nm or 13,122 cm^{-1}) is an overlap of a strong ($O_2(^1\Sigma_g^+, v' = 0) \leftarrow O_2(^3\Sigma_g^-, v'' = 0)$) and a weak band ($O_2(^1\Sigma_g^+, v' = 1) \leftarrow O_2(^3\Sigma_g^-, v'' = 1)$) of electronic transitions between the ground state ($^1\Sigma_g^+$) and an excited state ($^3\Sigma_g^-$).

2.6 Radiative Transfer

In this section, an overview of the process of the radiative transfer through the Earth's atmosphere is given. Therefore, the passage of the incoming solar light through the atmosphere and the interacting processes like the absorption, scattering and reflection of light needs to be described. Information about the absorption of light by gas molecules can be found in the previous section.

The radiative transfer can be described by using the Lambert-Beer law. This law characterises the exponential decrease of the radiant intensity ($I(\lambda)$) during the passage through a medium along a given light path (l) and wavelength (λ):

$$I(\lambda) = I_0(\lambda) \cdot e^{-\tau(\lambda)}. \tag{2.11}$$

$I_0(\lambda)$ is the (incoming) radiance at the starting point of the light path and $\tau(\lambda)$ is the optical depth which is determined from

$$\tau_\lambda = \int_{l_1}^{l_2} \varepsilon_\lambda(l) dl. \tag{2.12}$$

Here, $\varepsilon_\lambda(l)$ is the extinction coefficient along the light path and is obtained by the product of the cross section ($\sigma(l)$) and the number density ($n(l)$) of the absorbing and scattering constituent of the atmosphere which are gas molecules, aerosols and clouds. The extinction coefficient can also be written by the sum of scattering coefficient and absorption coefficient ($\varepsilon_\lambda = k_{a,\lambda} + k_{s,\lambda}$).

2.6.1 Rayleigh and Raman Scattering

An important scattering effect is Rayleigh scattering, which is the elastic scattering of light on small particles ($2\pi r \ll \lambda$, where r is the particle radius) such as gas molecules. The Rayleigh scattering coefficient is given by $k_R = \sigma_R \cdot n$, where σ_R is the

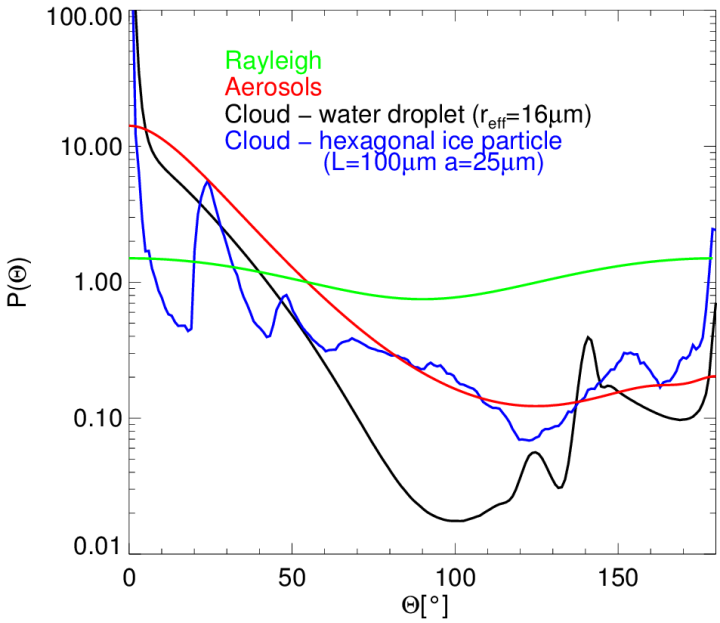

Figure 2.13: Phase functions for different particle sizes and shapes. The green curve shows the phase function for scattering on small particles (Rayleigh). The red curve shows the phase function for larger particles (Aerosols) according to the Mie theory. The blue and black curve are the phase functions of cloud particles with different shapes.

Rayleigh scattering cross section and n is the air density. The Rayleigh scattering cross section is proportional to λ^{-4}, which means that blue light is scattered more in the atmosphere than red light. Therefore, the (cloud free) sky is typically blue.

An important parameter for light scattering is the phase function (P). It describes the angular distribution of the scattered light. The angular distribution function is characterised by a more or less distinct forward and backward peak and is given for Rayleigh scattering by

$$P(\cos\Theta) = \frac{3}{4}(1+\cos^2\Theta). \tag{2.13}$$

Here, Θ is the scattering angle. The Rayleigh phase function is shown in Fig. 2.13.

Raman scattering is the inelastic scattering of light. This process occurs primary in the UV region and is responsible for an in-filling of the Fraunhofer lines, which is also referred to as the Ring effect (Grainger and Ring, 1962). In the spectral region of the O_2-A band and the 1.6 µm CO_2 absorption band used for this thesis, Raman scattering only plays a minor role.

2.6.2 Aerosols

Aerosols are suspended particles in the atmosphere with sizes typically between 1 µm and 10 µm. They are characterised by their form, size, mass, chemical composition and their moisture content. They influence directly or indirectly the radiation budget of the atmosphere as shown in Sec. 2.3 and have an effect on the human health.

The size and the composition of aerosol particles are determined by their origin and atmospheric processes. An important source is the ocean. Due to the wind and droplet evaporation about 1,000 – 10,000 Mt/yr of sea salt aerosols are produced (Brasseur et al., 1999). Other sources are windblown dust (e.g. desert dust), forest fires, volcanoes and organics (e.g. pollen, spurs, bacteria, viruses). In addition, aerosols are formed from the gas phase by gas-particle conversion. SO_2, for instance, can react with oxygen to SO_3 and then with water to sulphuric acid (H_2SO_4), which is taken up by a condensation nucleus and forms an aerosol particle. The formed sulphuric acid droplets as well as nitric acid (HNO_3) formed by the reaction of NO_x (the x means any active NO_x species such as NO and NO_2) with water are responsible for acid rain.

A large contribution to the global aerosol amount comes from human activities. Human-made aerosols are industrial dust, soot, aerosols from biomass burning and windblown dust. All together, the mankind contributes with 1,065 – 1,365 Mt/yr to the global atmospheric aerosol content (Brasseur et al., 1999).

Sinks of aerosols are the dry and the wet deposit. Wet deposit is the washing out of aerosols from the atmosphere by rain. Dry deposit is the fall out of aerosol particles, which is more efficient for larger and heavier particles.

The size distribution of aerosols in the atmosphere is, e.g., a log-normal distribution, which is given by

$$n(r) = \frac{N}{\sqrt{2\pi}\log\sigma} \exp\left[-\frac{1}{2}\left(\frac{\log(r/r_M)}{\log\sigma}\right)^2\right]. \tag{2.14}$$

Here, $0 \leq r \leq \infty$ is the particle radius, r_M is the mode radius, σ is the standard deviation and N is the total particle density. The size distribution can be separated in aerosol size modes. The nucleation mode with particle radii of 0.001 - 0.1 µm, the accumulation mode with particle radii of 0.1 - 1.0 µm and the coarse mode with particle radii >1.0 µm. Figure 2.14 shows the size modes of mineral aerosols as an example. The aerosol particles grow by absorbing water vapour of the air. For this reason, aerosol radius and density is dependent on relative humidity.

The interaction of aerosols with electromagnetic radiation can be described by the Mie theory. This theory describes the interaction of electromagnetic radiation with

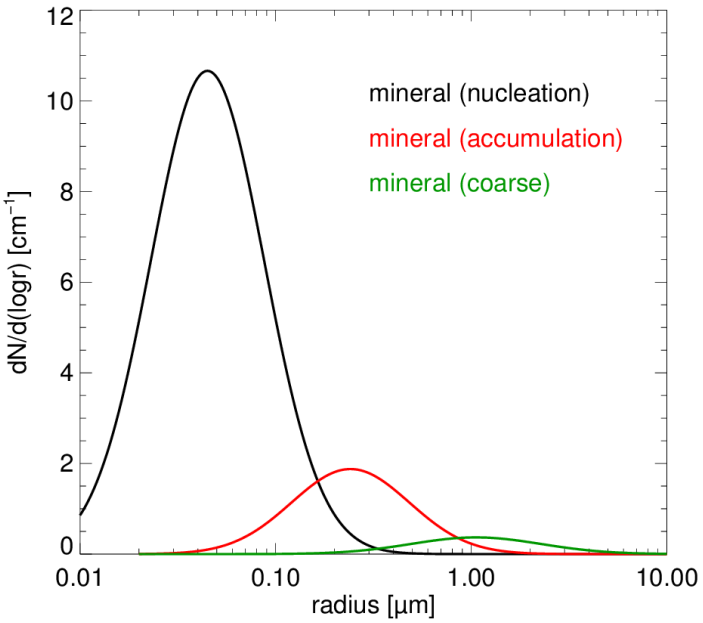

Figure 2.14: Size distributions for different size modes of mineral aerosols.

spherical particles ($2\pi r^2 \geq \lambda$). These spheres are characterised by a homogeneous complex refractive index, which consists of a real part and an imaginary part describing how strong an aerosol particle scatters and absorbs. A large imaginary part can be found for soot. The mathematical and theoretical background of the Mie theory goes beyond the scope of this thesis. More details can be found in, e.g., Mie (1908), Hoogen (1995), Kauss (1998) or in standard text books. However, the Mie theory is only an approximation because the form of various aerosol particles differs from a sphere.

The extinction coefficient of aerosols shows a less steeper wavelength dependence in comparison to Rayleigh and is typically proportional to λ^{-a}, where a is the Ångstrom exponent, which is typically 0 – 1.5. The single scattering albedo is the ratio of the scattering coefficient to the extinction coefficient. For strongly absorbing aerosols, the single scattering albedo is low. For non-absorbing aerosols, the single scattering albedo is 1. The extinction coefficient (ε), the scattering coefficient (k_s) and the single scattering albedo (ω) are related by the following ratio:

$$\omega_\lambda = \frac{k_{s,\lambda}}{\varepsilon_\lambda}. \tag{2.15}$$

An example of the phase function of aerosols according the Mie theory is shown

in Fig. 2.13. This phase function shows a larger forward peak in comparison to the Rayleigh phase function. For smaller aerosol particles the forward peak is less distinct pronounced.

For simulations of the radiative transfer through the atmosphere, a classification of aerosol compounds by their place of occurrence is very practicable. For instance, over urban areas more soot, over oceans more sea salt and over deserts more desert dust can typically be found. This is the reason why d'Almeida et al. (1991) have grouped tropospheric aerosols in ten main aerosol types: clean continental, averaged continental, polluted continental, clean maritime, polluted maritime, tropical maritime, urban, desert, Arctic and Antarctic. The aerosol types differ in their constituents, which are insoluble, water soluble, soot, minerals in different size modes, sea salt in different size modes and sulphate.

Figure 2.15 shows an example of an extinction coefficient profile and a single scattering albedo profile for an urban aerosol scenario. In the boundary layer, the aerosol types are mainly soot (68.6 %), water soluble (31.4 %) and insoluble aerosols (<1 %). The small single scattering albedo in this region indicates the strong absorption of light due to soot. In the free troposphere, the average continental type (54.2 % soot, 45.8 % water soluble, <1 % insoluble) is used. The stratospheric aerosol is 100 % sulphate and the mesospheric aerosol is meteoric dust.

2.6.3 Clouds

Clouds consist of water droplets and/or ice particles. They are located in the lower few kilometres and cover about 50 % of the Earth at any time (Kokhanovsky, 2006). Scattering by clouds is an important error source for satellite retrievals of atmospheric CO_2 concentrations just like aerosols. Therefore, most of the retrieval algorithms include restrictive cloud filtering, i.e., typically only nearly "cloud free" observations are used.

Clouds have a strong impact on the Earth's climate and influence it in many ways. These influencing processes are dependent on the macro- and microphysical characteristics of the clouds. They can reflect incident solar energy back to space, which results in a cooling of the Earth's surface. This depends among others on the cloud albedo and altitude. On the other hand, clouds warm the surface due to the fact that they prevent the energy in the Earth-atmosphere system from escaping. Polluted clouds, which are contaminated by soot, reflect less energy back to space, which results in a warming. However, contamination can also lead to a larger water droplet concentration and smaller particles, which increases the reflectance of the cloud resulting in a cooling.

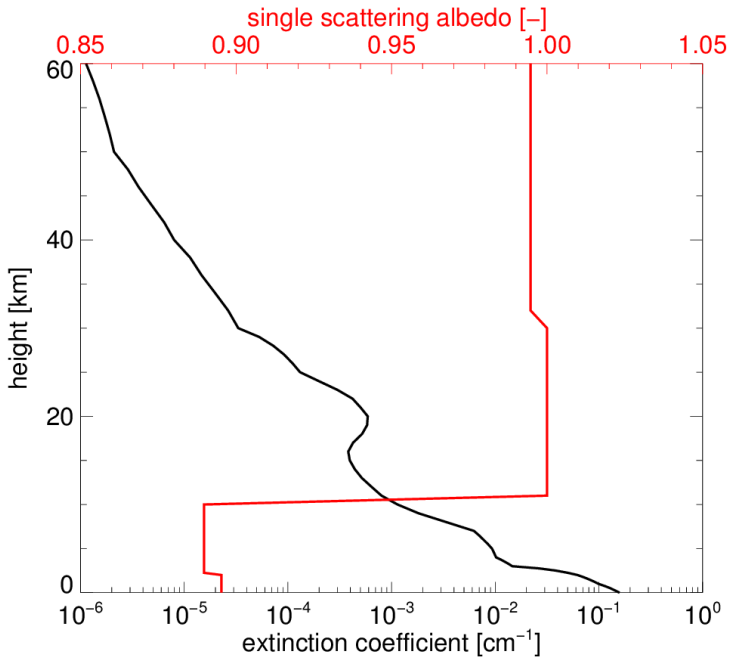

Figure 2.15: Extinction coefficient profile and single scattering albedo profile for an urban aerosol scenario (at 550 nm).

There are several different cloud types, which can be classified by their cloud base height (CBH). Low-level clouds (CBH < 2 km for mid-latitudes) are the Stratocumulus, the Stratus and the Nimbostratus. The Cumulus is also a low-level cloud, but has a large vertical extent (3 - 4 km). The Cumulonimbus can even reach the tropopause and stratosphere. Altostratus and Altocumulus are mid-level clouds and can be found between 2 and 6 km height for mid-latitudes. The high-level clouds are Cirrus, Cirrostratus and Cirrocumulus. They can be found at 6 - 8 km height for mid-latitudes and at 11 - 13 km in the tropics. The high-level clouds are composed of ice crystals because of the low temperature at these heights.

The influence of water clouds with spherical droplets within the radiative transfer can be described by the Mie theory. The phase function of water droplets show a large forward peak and a rainbow feature at around 138° (Fig 2.13). The size distribution of the particles within a cloud can be represented by a log-normal distribution. However, the shapes of ice particles are in comparison to the spherical water droplets more complex and the interaction with electromagnetic radiation cannot be described by the Mie theory. Usual ice particle shapes are plates, columns, needles, sheaths, dendrites, stars and bullets. Which particle shapes can be found at which height depends on temperature and pressure. An example for a phase func-

tion of a hexagonal ice column with length L = 100 µm and side length a = 25 µm is shown in Fig 2.13. The glory effect can be seen near the direct backward direction and the corona between 0° – 5°. The Halo (~22°) effect can be seen, e.g., when the Cirrusstratus is near the sun seen from the ground. The scattering coefficient for clouds is constant for wavelengths in the visible spectral region. This is the reason for the white to grey coloured clouds. Important parameters which are often used in connection with clouds are the liquid water content (LWC), which gives the amount of water per volume, and the liquid water path (LWP), which is the integrated LWC over the cloud thickness.

2.6.4 Surface Reflectance

Besides the scattering processes in the atmosphere, the reflectance of the surface plays an important role in the radiative transfer. Thereby, an important parameter is the albedo. The albedo (ϱ) of a surface is defined as the ratio of the reflected radiation flux density to the incident radiation flux density. The albedo depends on the wavelength and can be between 0 and 1. An albedo of 0 means, that no radiation is reflected while an albedo of 1 means that all incident radiation is reflected. Figure 2.16 shows the spectral dependence of the albedo of several surfaces. As an example, snow efficiently reflects radiation in the ultraviolet and visible spectral region, but is a poor reflector in the IR region.

The reflection of radiation from a surface depends also on the incident and reflection angles. This information is provided by the Bidirectional Reflectance Distribution Function (BRDF). However, this function is not known or is difficult to obtain. Therefore, the assumption of a diffuse reflecting surface is often used. This surface is referred to a Lambertian surface.

2.6.5 The Radiative Transfer Equation

The general radiative transfer equation, which describes the radiative transfer along a given light path ($\vec{s}$), is given by:

$$\frac{dI_\lambda(\vec{s})}{ds} = \varepsilon_\lambda(\vec{s}) \cdot (J_\lambda(\vec{s}, I) - I_\lambda(\vec{s})). \tag{2.16}$$

Here, ε_λ is the extinction coefficient and I_λ is the radiant intensity ($I_\lambda = \pi \cdot R/R_{\text{sun}}$, R is the radiance of the upwelling radiation measured at the top of the atmosphere and R_{sun} is the solar irradiance measured directly from the sun at the top of the atmosphere) given at wavelength λ. J_λ is the source function describing the gain of

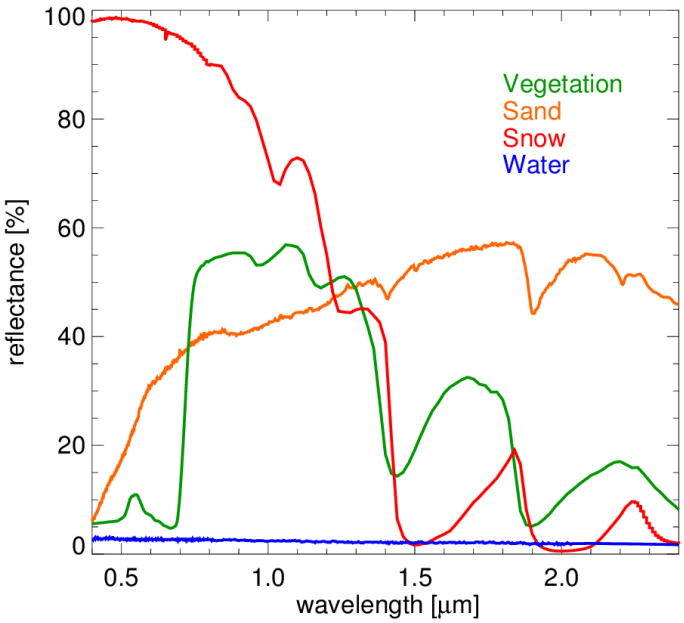

Figure 2.16: Spectral reflectance (albedo) of different surface types obtained from ASTER spectral library version 2.0 (Baldridge et al., 2009).

photons due to scattering into the light path and emissions. A gain of photons can be achieved, e.g., due to scattering caused by aerosols and thermal emission.

The radiative transfer equation can be solved by numerical methods. A radiative transfer code solving the radiative transfer equation is SCIATRAN, which is briefly described in the next subsection.

2.6.6 The Radiative Transfer Code SCIATRAN

The SCIATRAN radiative transfer code has been developed for fast and accurate simulations of spectra as measured by the SCIAMACHY satellite instrument (Sec. 2.7) in the wavelength range between 175 – 2,380 nm (Rozanov et al., 2005; Buchwitz et al., 2000a). SCIATRAN cannot only calculate the spectra for satellite observation geometries but also for other geometries (ground-based, air- and ballon-borne observations are possible).

In order to simulate spectral radiances, SCIATRAN can solve the radiative transfer equation for a plane-parallel atmosphere by three different methods: the discrete ordinate method, the finite difference scheme and the finite element approach. Besides the plan-parallel atmosphere assumption, the pseudo-spherical atmosphere

assumption can be used. By utilising this assumption, the light path for the direct solar beam in a spherical atmosphere is computed. After this, the radiative transfer equation is solved in the plan-parallel atmosphere assumption. In addition, a spherical atmosphere assumption can be used. Important simulation parameters have to be set, e.g., the surface albedo, surface elevation, the height of the measuring instrument and its observation direction. Other important parameters, which define the atmosphere are, e.g., the gas concentrations, the aerosol profile and cloud parameters. Finally, the radiative transfer equation is discretised and the equation is solved.

The absorption cross sections being important for the gas absorptions are temperature and pressure dependent and are computed from line parameters of all relevant optical transitions as mentioned in Sec. 2.5. These line parameters are the line position, the line intensity, the full width at half maximum (FWHM) of the line and other parameters. The HITRAN 2008 data base is the source of these line parameters (Rothman et al., 2009), which are determined by direct measurements and quantum mechanical models.

A method to approximate and consequently accelerate the radiative transfer simulation is the correlated-k method. This method is based on the sorting of mean spectral transmittances in a small wavelength interval according to the absorption cross section (σ_a). "Correlated" means that the sorting order of the absorption cross section is independent of altitude. For a detailed explanation of the correlated-k method see, e.g., Buchwitz (2000) and Buchwitz et al. (2000a).

2.7 SCIAMACHY

SCIAMACHY (SCanning Imaging Absorption spectroMeter for Atmospheric CHartographY) was a spectrometer and a multi-national contribution to the atmospheric chemistry payload of ESA's (European Space Agency) ENVISAT (ENVIromental SATellite) (see Fig. 2.17) (Burrows et al., 1995; Bovensmann et al., 1999). SCIAMACHY had operated for 10 years until ESA lost contact to ENVISAT on 8 April 2012 and finally had decided the official end of the ENVISAT mission at 9 May 2012.

The objectives of SCIAMACHY were and still are as the evaluation of the data is ongoing to improve our knowledge of global atmospheric composition and atmospheric processes and their change in response to natural and anthropogenic activities. Targets are gases (O_2, O_3, O_4, NO, NO_2, CO, CO_2, HCHO, CH_4, H_2O, N_2O, SO_2, BrO, OClO) as well as clouds, aerosols, the ocean colour and land parameters.

ENVISAT was launched in March 2002 into a sun-synchronous (descending) orbit with an equator crossing time of 10:00 am. The satellite, with a length of 25 m, was

Figure 2.17: The SCIAMACHY instrument on-board ESA's ENVISAT (from Gottwald and Bovensmann, 2011).

the largest satellite ever built by ESA. On an altitude of 799.8 km, ENVISAT performed $14\frac{11}{35}$ Orbits per day and achieved global coverage after 35 days (501 orbits).

The SCIAMACHY instrument was a passive imaging spectrometer, which consisted of a scan mirror system, a telescope and a spectrometer (see Fig. 2.18). SCIAMACHY was located on the upper right corner (referring to the flight direction) of the ENVISAT platform. The scan mirror system allowed several observation geometries: nadir, limb, solar and moon occultation. In nadir observation geometry, the mirror system scanned $\pm 32°$ across track relative to direct nadir viewing and provided a swath width of 960 km (see Fig. 2.19).

The spectrometer concept was based on a two stage dispersion system as shown by Fig. 2.18. Behind the entrance slit a pre-disperser prism was mounted to weakly disperse the incoming light. In addition, the prism directed fully polarised (perpendicular to the optical plane) light (due to Brewster angle reflection) to the seven different spectral bands of the Polarisation Measurement Device (PMD). The other part of the light was directed to the eight science channel detectors by di-chroic mirrors and further disperse the light by individual gratings. The detectors of science channels 1 – 5 (UV-VIS-NIR) were standard Silicon detectors with 1024 pixels. For science channels 6 – 8, Indium Gallium Arsenide detectors were used. In order to increase the sensit-

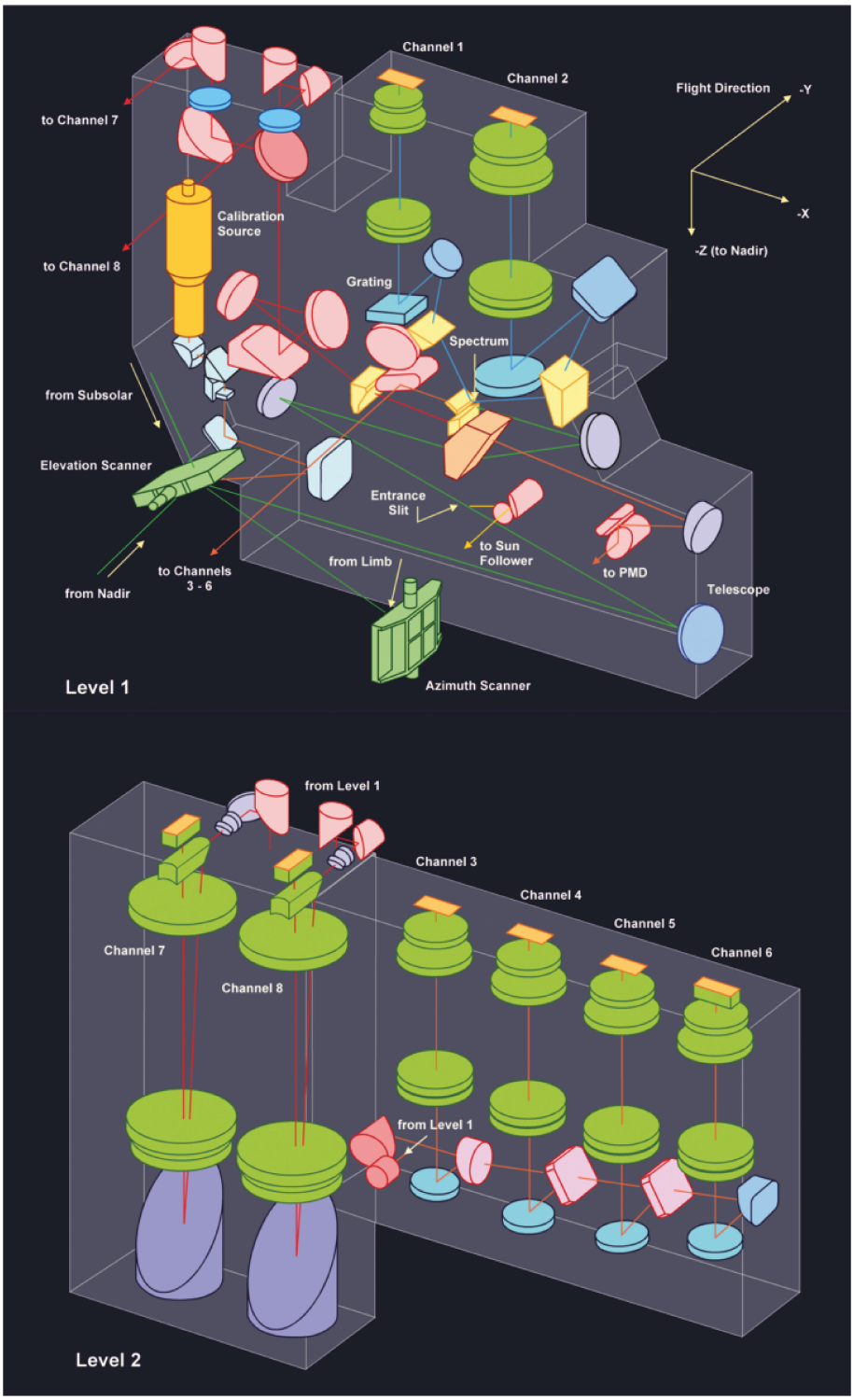

Figure 2.18: Instrumental design of the SCIAMACHY instrument (from Gottwald and Bovensmann, 2011).

ivity for measurements at a wavelength larger than 1,700 nm, the upper part of the channel 6 (6+) detector and the channel 7 and 8 detectors were grown with a larger fraction of Indium.

In the science channels, SCIAMACHY continuously measured reflected, backscattered and transmitted solar radiation covering the spectral regions 214 – 1,750 nm, 1,940 – 2,040 nm and 2,265 – 2,380 nm. The spectral resolution ranged from 0.2 to 1.4 nm. In addition to the eight main channels, seven PMD channels measured upwelling polarised broad band radiation with higher spatial resolution.

Within this thesis, nadir observations from channel 4 (605 – 805 nm; for O_2), channel 6 (1,000 – 1,750 nm; for CO_2 and water vapour) and PMD 1 (320 – 380 nm) are used. The integration time of the instrument in the used spectral regions of channels 4 and 6 was typically 0.25 s and provided a typical spatial resolution of 60 km across track by 30 km along track.

SCIAMACHY was in the period 2002 to 2009 the only satellite instrument, which observed backscattered near-infrared sunlight suitable for retrieval of CO_2 columns or XCO_2 with high sensitivity down to the Earth's surface (Buchwitz et al., 2005a,b, 2006, 2007; Houweling et al., 2005; Bösch et al., 2006; Barkley et al., 2006a,c,b, 2007; Schneising et al., 2008, 2011; Reuter et al., 2010). At the moment the only satellite with this characteristic is the Fourier transform spectrometer TANSO (Thermal And Near infrared Sensor for carbon Observation) on-board GOSAT (Greenhouse gases Observing SATellite) (Yokota et al., 2004; Kuze et al., 2009), launched in 2009.

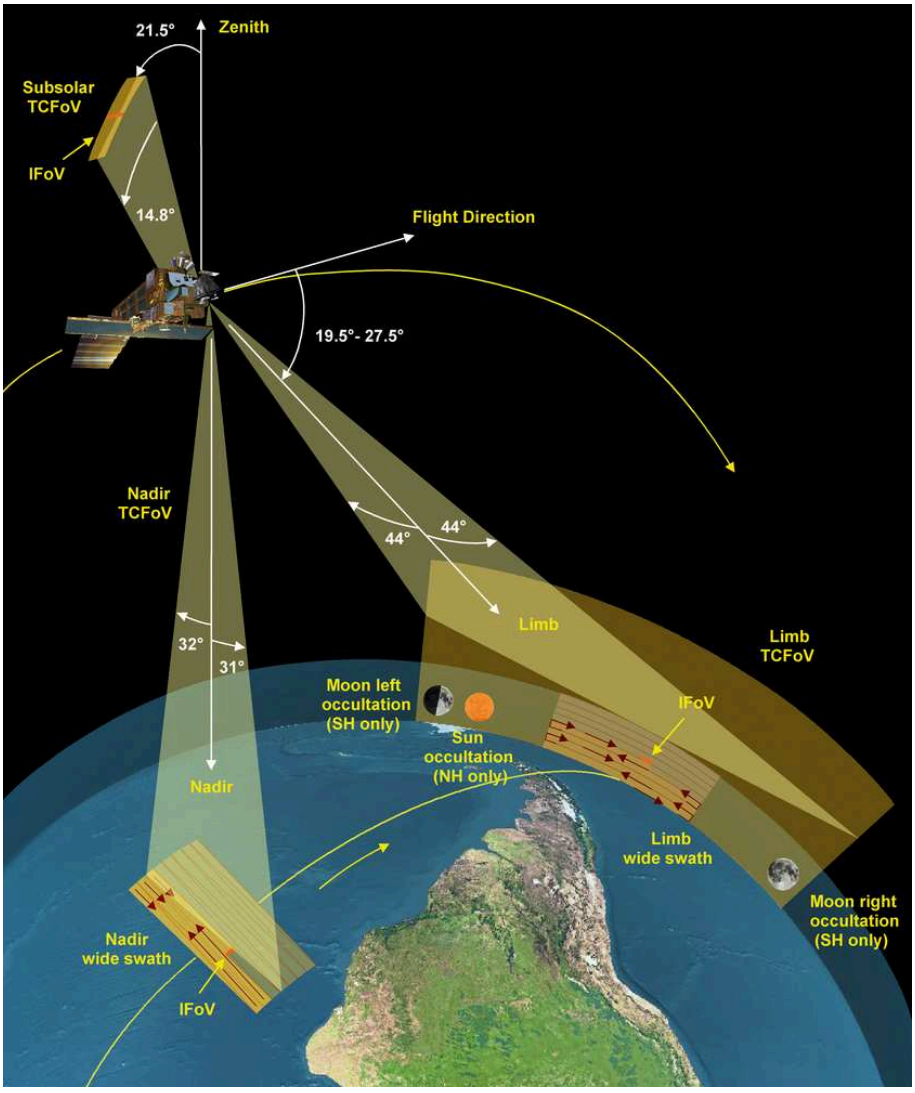

Figure 2.19: Viewing modes of SCIAMACHY (from Gottwald and Bovensmann, 2011).

3 SCIAMACHY WFM-DOAS Version 2.1 XCO_2

The Weighting Function Modified - Differential Optical Absorption Spectroscopy algorithm was developed at the University of Bremen to retrieve vertical columns of several atmospheric gases such as O_2, CO_2 and CH_4 from SCIAMACHY measurements (Buchwitz et al., 2000b). This algorithm has been further improved continuously to meet the needs of the data user community (Buchwitz and Burrows, 2004; Buchwitz et al., 2005a,b; Schneising et al., 2008, 2009, 2011, 2012). The initial WFM-DOAS (WFMD) data product, which is used for an investigation concerning retrieval errors due to unaccounted scattering by aerosols and clouds, is version 2.1 described in Schneising et al. (2011). An overview of the retrieval algorithm and its theoretical background follows with the focus on the retrieval of the O_2 and CO_2 columns.

The focus of this section is presenting results of (i) a sensitivity study of the WFM-DOAS included cloud detection algorithm and of (ii) a correction of a scan-angle-bias in the WFM-DOAS XCO_2 data product, which are partly adapted from Heymann et al. (2012a).

3.1 Inversion Theory

In order to obtain information about atmospheric gases, clouds and aerosols from SCIAMACHY measurements, several inversion methods can be utilised, e.g., DOAS, WFM-DOAS and optimal estimation. The spectral measurements of SCIAMACHY are in the UV, VIS and NIR spectral region. The advantage to use measurements in these spectral regions are that the atmosphere is nearly transparent and thermal emission can be neglected. In addition, the measurements give information from all atmospheric layers including the boundary layer.

The measurement technique, which is used to determine trace gas concentration from spectral measurements of SCIAMACHY is the Differential Optical Absorption Spectroscopy (DOAS). The idea behind DOAS is that the wavelength dependent absorption signal can be separated into a high frequency and a low frequency part. One

way to achieve this is to separate the optical depth in two parts:

$$\tau(\lambda) = \tau_{\mathrm{g}}(\lambda) + \tau_{\mathrm{s}}(\lambda). \tag{3.1}$$

The high frequency part (τ_{g}) stands for the atmospheric gas absorptions. The low frequency part ($\tau_{\mathrm{s}}(\lambda)$) considers broadband structures in the measured spectra. These structures can result from Rayleigh - and Mie scattering and also from instrumental issues. The low frequency part can be approximated by a low order polynomial:

$$\tau_{\mathrm{s}}(\lambda) \approx \sum_{\mathrm{k}=0}^{n} a_{\mathrm{k}} \lambda^{\mathrm{k}}. \tag{3.2}$$

Here, n is the order of the polynomial and a_{k} are the polynomial coefficients. The logarithm of the measured intensity can then be written as:

$$\ln I_\lambda = -\tau_{\mathrm{g}}(\lambda) + \tau_{\mathrm{s}}(\lambda), \tag{3.3}$$

which can be converted together with Eq. 2.12 and Eq. 3.2 to the DOAS equation

$$\ln I_\lambda = -\int_{l_1}^{l_2} \sigma_\lambda^{\mathrm{g}}(l) n(l) dl + \sum_{k=0}^{n} a_k \lambda^k. \tag{3.4}$$

Assuming that the absorption cross section of an atmospheric trace gas is considered to be independent of the altitude gives

$$\ln I_\lambda = -S\sigma_\lambda^{\mathrm{g}} + \sum_{k=0}^{n} a_k \lambda^k, \tag{3.5}$$

where

$$S = \int_{l_1}^{l_2} n(l) dl \tag{3.6}$$

is the slant column given in molecules per cm^2. In order to obtain the observation geometry independent vertical column (V) the slant column needs to be divided by the air mass factor (AMF):

$$V = \frac{S}{AMF}. \tag{3.7}$$

The air mass factor AMF is in plan-parallel geometry only dependent on the solar zenith angle (ϑ) and is given by

$$AMF = \frac{1}{\cos\vartheta}. \tag{3.8}$$

A weak trace gas absorption is needed otherwise the assumption that the logarithm of the intensity depends linearly on the trace gas vertical column is not fulfilled. In addition, the Lambert-Beer law is strictly valid only for monochromatic intensity measurements. This is invalid for radiation that strongly depends on wavelength within spectral intervals as defined by the instruments resolution. Furthermore, the assumption of an altitude independent absorption cross section is only valid if the cross section only slightly depends on temperature and pressure. The selection of one cross section valid for one altitude can introduce large vertical column errors if the cross section strongly depends on temperature and pressure. In the case that an assumption of DOAS is not fulfilled, a more general formalism can be utilised. For this purpose, weighting functions are needed, which describe the change of the measured radiation ($\ln I_\lambda$) by the variation of the fit parameter (x_i):

$$w_\mathrm{i}(\lambda) = \frac{\partial \ln I_\lambda}{\partial x_\mathrm{i}}. \tag{3.9}$$

The x_i can be the column density of absorbers (V_j) but also the surface albedo, temperature or an aerosol or cloud parameter. The logarithm of the intensity can then be developed in a Taylor expansion around a modelled intensity (I_0^mod) for a linearisation point ($\vec{x}_0$):

$$\ln I_\lambda = \ln I_0^\mathrm{mod} + \sum_\mathrm{i} w_\mathrm{i}(\lambda)(x_\mathrm{i} - x_{0,\mathrm{i}}) + \sum_{\mathrm{k}=0}^{n} a_\mathrm{k}\lambda^\mathrm{k}. \tag{3.10}$$

This equation is called the WFM-DOAS equation and was developed at the University of Bremen (Buchwitz et al., 2000b). In order to solve this equation and to determine the desired x_i, a least squares method can be used. Thereby, the following cost function has to be minimised:

$$\sum_{\mathrm{k}=1}^{n} \left(\ln I_{\lambda_\mathrm{k}} - \ln I_{\lambda_\mathrm{k}}^\mathrm{mod}(\vec{x},\vec{a})\right)^2 = ||\overrightarrow{\mathrm{RES}}||^2 \rightarrow \min. \tag{3.11}$$

Here, n is the number of wavelengths.

In a more general notation, the relation between the measurement ($\vec{y}$) and the model parameters ($\vec{x}$) of the forward model ($\vec{F}(\vec{x})$) can be formulated as follows:

$$\vec{y} = \vec{F}(\vec{x}) + \vec{\varepsilon}. \tag{3.12}$$

Here, $\vec{\varepsilon}$ is the vector of the measurement noise.

The Taylor expansion at the reference state $\vec{x}_0$ can then be expressed as

$$\vec{y} - \vec{F}(\vec{x}_0) = \frac{\partial \vec{F}(\vec{x})}{\partial \vec{x}}(\vec{x} - \vec{x}_0) + \vec{\varepsilon} = \vec{K} \cdot (\vec{x} - \vec{x}_0) + \vec{\varepsilon}, \tag{3.13}$$

where $\vec{K}$ is the weighting function matrix or Jacobian. This equation can also be solved by a least squares method, which can now be described by the minimisation of the quadratic norm

$$||\vec{y} - \vec{K}\vec{x}||^2 = \chi^2 \rightarrow \min. \tag{3.14}$$

The solution ($\hat{\vec{x}}$) is then given by

$$\hat{\vec{x}} = \hat{\vec{S}}\vec{K}^T\vec{y}, \tag{3.15}$$

where

$$\hat{\vec{S}} = \left(\vec{K}^T\vec{K}\right)^{-1} \tag{3.16}$$

is the error covariance matrix and describes the cross correlations of the retrieved state vector ($\hat{\vec{x}}$) elements. T denotes that a matrix or vector is transposed. The error of the retrieved columns ($\hat{V}_\mathrm{j}$) can be estimated by

$$s_{\hat{V}_\mathrm{j}} = \sqrt{\frac{(\hat{\vec{S}})_{\mathrm{jj}}\chi^2}{m-n}}, \tag{3.17}$$

where m is the dimension of the measurement vector $\vec{y}$ and n is the dimension of the state vector $\vec{x}$.

The height dependent response of the retrieved gas column ($\hat{V}$) to variations of the true gas column (V^t), the averaging kernel $A(z)$ can be obtained by

$$A(z) = \frac{\hat{V}_\mathrm{p} - \hat{V}_\mathrm{u}}{V_\mathrm{p}^\mathrm{t} - V_\mathrm{u}^\mathrm{t}}, \tag{3.18}$$

where V_u^t is the true column, V_p^t is the true column of a perturbed vertical profile, i.e., the true vertical profile but with an enhanced concentration at altitude z, $\hat{V}_\mathrm{p}$ is the retrieved column of the perturbed vertical profile and $\hat{V}_\mathrm{u}$ is the retrieved column of the unperturbed vertical profile. The WFMD averaging kernel and the a-priori CO_2 profile are shown in Fig. 3.1. As can be seen SCIAMACHY has a high sensitivity down to the surface.

A more general approach to determine atmospheric parameters from the spectral measurements is based on “optimal estimation”, which is here only briefly described (a detailed description is given in Rodgers, 2000). Optimal estimation considers a-priori knowledge. As a result the following cost function is minimised

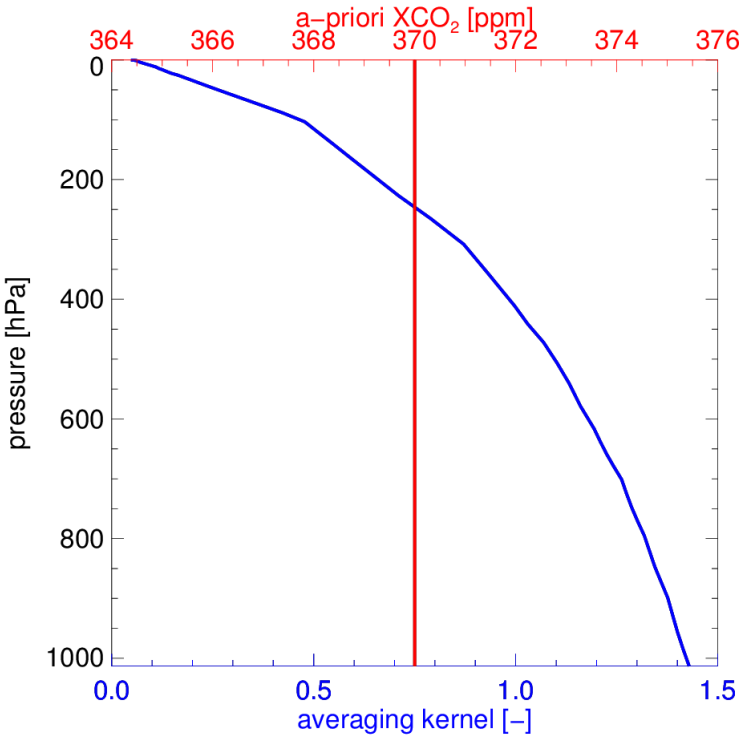

Figure 3.1: SCIAMACHY WFM-DOAS XCO_2 averaging kernel and a-priori XCO_2 profile.

$$\left(\vec{y}-\vec{F}(\vec{x})\right)^T \vec{S}_\varepsilon^{-1}\left(\vec{y}-\vec{F}(\vec{x})\right)+(\vec{x}-\vec{x}_\mathrm{a})^T \vec{S}_\mathrm{a}^{-1}(\vec{x}-\vec{x}_\mathrm{a})\,. \tag{3.19}$$

Here, $\vec{S}_\varepsilon$ is the error covariance matrix of the measurement, $\vec{x}_\mathrm{a}$ is the a priori state vector and $\vec{S}_\mathrm{a}$ is the a priori error covariance matrix. The solution ($\hat{\vec{x}}$) of this minimisation can be determined by using a Gauss-Newton iteration scheme

$$\vec{x}_{\mathrm{i}+1}=\vec{x}_\mathrm{i}+\hat{\vec{S}}_\mathrm{i}\left(\vec{K}_\mathrm{i}^T\vec{S}_\varepsilon^{-1}\left(\vec{y}-\vec{F}(\vec{x}_\mathrm{i})\right)\right)-\vec{S}_\mathrm{a}^{-1}(\vec{x}_\mathrm{i}-\vec{x}_\mathrm{a})\,, \tag{3.20}$$

where

$$\hat{\vec{S}}_\mathrm{i}=\left(\vec{K}_\mathrm{i}^T\vec{S}_\varepsilon^{-1}\vec{K}_\mathrm{i}+\vec{S}_\mathrm{a}^{-1}\right)^{-1}. \tag{3.21}$$

The iteration starts with the first guess state vector $\vec{x}_0$ and is often set to $\vec{x}_\mathrm{a}$. If convergence is achieved, $\vec{x}_{\mathrm{i}+1}$ is the most probable solution and is denoted as maximum a posteriori solution $\hat{\vec{x}}$.

Optimal estimation is used, e.g., by the SCIAMACHY XCO_2 retrieval algorithm, called BESD (Bremen optimal EStimation Doas), described in Reuter et al. (2010) and

Reuter et al. (2011).

3.2 The WFM-DOAS Retrieval Algorithm

The WFM-DOAS retrieval algorithm uses two spectral fit windows, which cover the O_2-A absorption band between 755 nm and 775 nm (an overlap of a weak and a strong electronic transition, see Sec. 2.5.3) and CO_2 absorption lines between 1,558 nm and 1,594 nm (vibrational-rotational structure, see Sec. 2.5.2). An example of sun-normalised radiances within these spectral regions and in SCIAMACHY resolution is shown in Fig. 3.2.

WFMD is a least-squares method, which scales and shifts pre-selected atmospheric vertical profiles. The logarithm of a linearised radiative transfer model is fitted to the logarithm of the measured sun-normalised radiance (see Eq. 3.11). The fit-parameters directly yield the desired vertical columns of CO_2 and O_2. The retrieved CO_2 and O_2 columns are the number of CO_2 and O_2 molecules per unit area integrated along the light path. Ideally, the light path is simple (no scattering), but in general the light path is not well known. Therefore, it is assumed that the light paths in the CO_2 and O_2 fit windows are the same and the retrieved O_2 column can be used as a proxy for the light path of CO_2 (therefore, this method is called light path proxy method). This is achieved by dividing the CO_2 by the O_2 column, which in first order results in the cancellation of light path modifications. In addition, the O_2 column is needed in order to obtain the dry air column required for the conversion of the CO_2 column into XCO_2 (Schneising et al., 2008), the final product of the WFMD algorithm.

Figure 3.3 shows the advantages of the conversion of the CO_2 column into XCO_2. The retrieved CO_2 column (CO_2^{col}) not only shows variations due to CO_2's sources and sinks but also due to high and low pressure systems, topography and scattering effects, which are also shown for the air column. Therefore, dividing the CO_2 by the air column reduces or even eliminates these influences and the small variations originating from the sources and sinks of CO_2 become visible. A good proxy for the air column is the O_2 column (O_2^{col}) because its concentration ($XO_2 = 0.2095$) is only subject to insignificantly variations compared to variations in the CO_2^{col}. The resulting XCO_2 is finally computed from

$$XCO_2 = \frac{CO_2^{col}}{O_2^{col}} \cdot XO_2 \tag{3.22}$$

The conversion of the CO_2 column into XCO_2 by using O_2 as light path proxy has also some limitations. The O_2-A band and the used CO_2 absorption lines are spec-

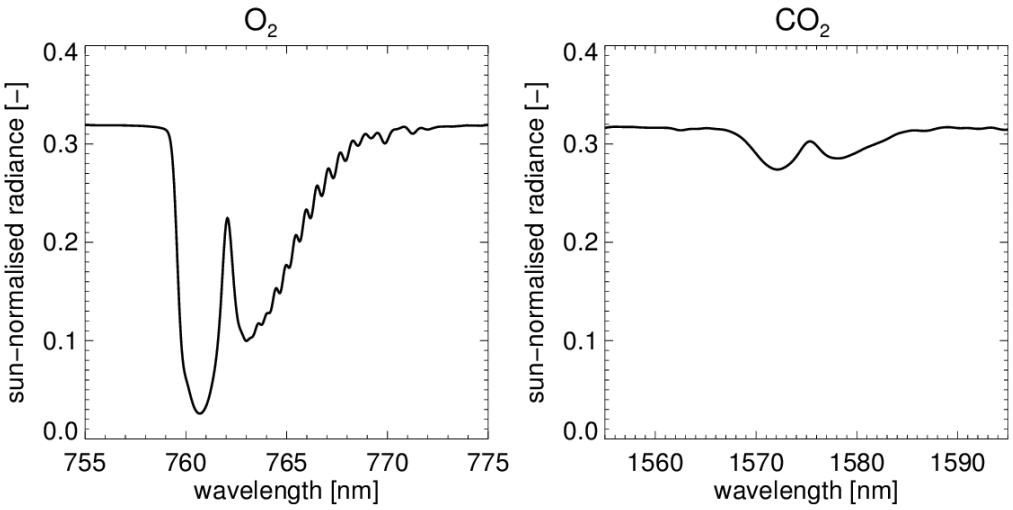

Figure 3.2: Sun-normalised radiances between 755 – 775 nm (O_2-A band, left) and between 1,555 – 1,595 nm (CO_2 absorption lines, right) in SCIAMACHY resolution. The radiances are simulated by using the radiative transfer code SCIATRAN.

trally distant. Therefore, variations of the wavelength dependent optical properties of scattering particles, e.g., aerosols and cloud particles, can lead to different light paths for O_2 and CO_2. In this case, using O_2 as light path proxy for CO_2 can only be a crude assumption, which can result in systematic XCO_2 retrieval errors. Therefore, WFM-DOAS has approaches to handle aerosols and clouds (see Sec. 3.3 and Sec. 3.4).

The SCIAMACHY XCO_2 retrieval algorithm not only has to be very accurate but also sufficiently fast in order to process the large amounts of data produced by SCIAMACHY. For this reason, a fast look-up-table (LUT) scheme has been developed to avoid computationally expensive radiative transfer (RT) simulations. The LUT consists of tabulated sun-normalised radiances and weighting functions, which are computed for different columns of O_2, CO_2 and water vapour, for different solar zenith angles (SZA), albedos, surface elevations and shifts of the temperature profile. The state vector of the inversion scheme includes parameters for the low order polynomial, the temperature shift and a scaling factor of the O_2 column for the retrieval of O_2. For the retrieval of CO_2 parameters for the low order polynomial, the temperature shift and scaling factors for the CO_2 and water vapour columns are included. The SZA is directly obtained from the SCIAMACHY measurements and the surface elevation is obtained from a topology data base. The albedo is determined by a WFMD included surface albedo retrieval assuming a default aerosol profile. The required radiances and weighting functions are obtained by linear interpolation within

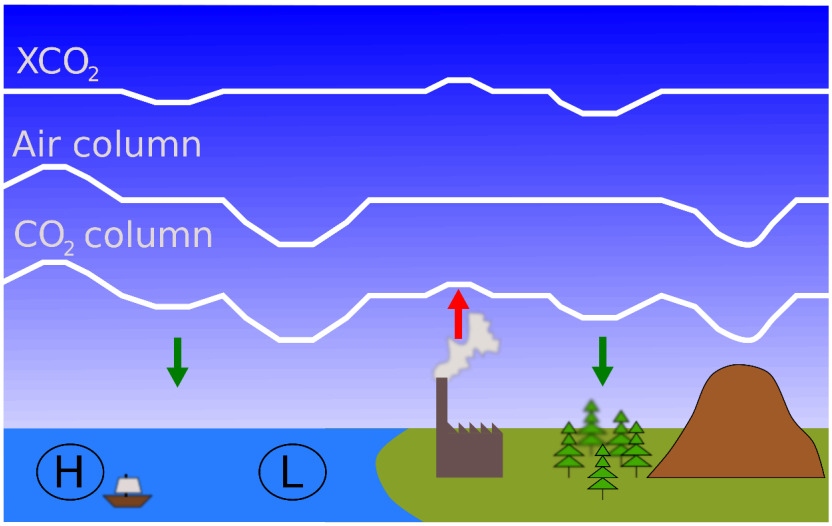

Figure 3.3: Possible spatial variations of the CO_2 column and the air column in comparison to the variations of the column-averaged dry air mole fraction of CO_2 (XCO_2). The green arrows indicate a CO_2 sink and the red arrow indicates a CO_2 source. The H and L denotes a high pressure and a low pressure system, respectively.

the LUT.

After the fit procedure, the quality of the retrieved XCO_2 is checked by using binary quality flags ("good/bad"), which are set a posteriori to identify successful retrievals. They are based on the following criteria: The first criterion concerns the quality of the spectral fits. In order to filter poor fits, the root-mean-square (RMS) of the fit residuum (relative difference between measurement and model after the fit) in the O_2 fit window have to be smaller than 2 % and in the CO_2 fitting window smaller than 0.25 % because the retrieved XCO_2 becomes unreliable if large differences between the measured and the fitted spectra remain. In addition, the CO_2 column fit error has to be less than 2.5 % (see Sec. 3.1). Due to low signals and saturation effects, the solar zenith angle have to be less than 75°. In addition, a plane parallel atmosphere assumption is used in the radiative transfer calculations, which results in significant errors for large solar zenith angles. The worse signal-to-noise ratio over water are the reason why the ground pixel have to be over land. Only forward scan pixels (60 km by 30 km) are analysed because backward scan pixel have only a poor resolution of 240 km by 30 km. LUT limitations are the reason why the surface elevation has to be smaller than 5 km. How WFMD handles aerosols and clouds is presented in the next sections.

3.3 WFM-DOAS and Aerosols

The scattering on unaccounted aerosols and clouds are important potential error sources for satellite retrievals (Tolton and Plouffe, 2001; O'Brien and Rayner, 2002; Kuang et al., 2002; Dufour and Bréon, 2003; Buchwitz et al., 2005a; van Diedenhoven et al., 2005; Barkley et al., 2006a; Aben et al., 2006; Bril et al., 2007; Reuter et al., 2010; Houweling et al., 2005; Schneising et al., 2008). Therefore, the retrievals typically include strict filtering approaches to minimise these errors.

WFMD uses a constant aerosol vertical profile for the RT simulations, which does not depend on time or location. Aerosol variability is taken into account as follows: (i) by using O_2 as proxy for the light path, (ii) by the low-order polynomial included in the WFMD spectral fits, which makes the retrieval insensitive to spectrally broadband radiance modifications resulting from, e.g., aerosols (the smooth wavelength dependence of aerosols described by the Ångstrom exponent), and (iii) by filtering out scenes contaminated by high loads of aerosols as identified using the SCIAMACHY Absorbing Aerosol Index (AAI) (Tilstra et al., 2007) data product, which is sensitive to elevated absorbing aerosols such as desert dust and biomass burning aerosols. Schneising et al. (2008) found that unrealistic enhanced CO_2 mole fractions are correlated with enhanced levels of absorbing aerosols.

The AAI depends on the difference of the slopes between two specific wavelengths (λ_0 and λ_1) of an observed reflectance spectrum and a simulated pure Rayleigh scattering reflectance spectrum (corresponding to an observation without aerosols and clouds) and is retrieved from SCIAMACHY measurements (Tilstra et al., 2007). The reflectance (ϱ) is the measured intensity at top of the atmosphere divided by the cosine of the sun zenith angle (SZA). The AAI is then determined from

$$\mathrm{AAI} = -100\,(\log_{10}(\frac{\varrho_{\lambda_1}}{\varrho_{\lambda_0}})^{\mathrm{meas}} - \log_{10}(\frac{\varrho_{\lambda_1}}{\varrho_{\lambda_0}})^{\mathrm{ray}}) \tag{3.23}$$

A scenes are filtered out if the AAI is larger than a certain threshold.

Nevertheless, aerosols are still a possible source of errors. Schneising et al. (2008) performed simulations to estimate the impact of aerosols on the WFMDv1.0 XCO_2 retrievals using several aerosol scenarios. They concluded that aerosol related XCO_2 errors are typically below 1%.

3.4 WFM-DOAS and Clouds

As mentioned, clouds are an important error source for the retrieval of XCO_2 from measurements of the upwelling solar electromagnetic radiation at the top of the at-

mosphere. Consequently, cloud contaminated ground scenes have to be identified and filtered out. For this purpose, WFM-DOAS includes a cloud detection algorithm, which is based on two cloud filtering criteria and filters out cloudy scenes if one of these criteria is met.

The first criterion, used to establish cloud free scenes, is based on subpixel information provided by SCIAMACHY's polarisation measurement device (PMD) 1. PMD 1 is mainly sensitive to radiation which is polarised perpendicular to the SCIAMACHY optical plane and covers the ultraviolet A (UVA) region between 310 nm and 365 nm. The spatial resolution is approximately 15 km by 30 km (Bovensmann et al., 1999) and is therefore four times higher than the typical SCIAMACHY resolution. In order to identify a cloud contaminated ground scene, the high cloud brightness in the UVA region is used. PMD 1 is one of seven SCIAMACHY PMD channels and has been selected because of its low sensitivity to surface albedo variations (Buchwitz et al., 2005a). If the normalised and solar zenith angle corrected PMD 1 signal of one subpixel exceeds a certain threshold, the ground pixel is classified as cloud contaminated (Buchwitz et al., 2005a).

The second criterion is based on a threshold for the retrieved O_2 column. The retrieved O_2 column has to be larger than 90% of the assumed a-priori O_2 column, which is determined from surface height, the barometric formula and the US standard atmosphere (Schneising et al., 2008). As the O_2 column is relatively well known, deviations from the reference O_2 column are an indicator for light path shortening or lengthening, e.g., due to scattering by clouds.

In the following section more details describing the cloud detection algorithm are presented along with a quantitative analysis of the sensitivity of this algorithm.

3.5 Sensitivity of the WFM-DOAS Cloud Detection Algorithm

In order to study the influence of clouds on WFMDv2.1 XCO_2, one has to know "which clouds" remain undetected after the application of the WFM-DOAS PMD 1 and O_2 based cloud detection algorithm. For this reason, the minimum detectable effective cloud optical depth (eCOD defined as cloud optical depth times cloud fractional coverage), which can be detected ("detection limit") using the WFMDv2.1 cloud detection algorithm, has been determined using simulations. In the following it is described how these PMD 1 and O_2 detection limits have been obtained and what their limit values are.

The SCIAMACHY PMD signals are not absolutely radiometrically calibrated. To be

able to determine the sensitivity of the PMD-based cloud detection algorithm using RT simulations, the PMD cloud detection threshold needs to be related to the corresponding radiance or sun-normalised radiance also called intensity.

The uncalibrated PMD 1 signal is normalised to a fixed maximum value and divided by the cosine of the solar zenith angle (SZA). If this reflectivity-like PMD signal, SR_{PMD}, exceeds a given threshold of SR_{PMD} = 0.7 for at least one PMD subpixel, the SCIAMACHY pixel is flagged as cloudy. The used maximum value and the threshold have been obtained by visual inspection of SCIAMACHY PMD images (Buchwitz et al., 2005a).

In order to simulate SR_{PMD} using RT simulations, the PMD 1 was calibrated, i.e., the corresponding intensity in absolute physical units was determined. For this purpose, the calibrated SCIAMACHY nadir intensity spectra in the corresponding wavelength region (using channel 2, cluster 9, covering the region 320 nm - 365 nm) have been used. As shown in Fig. 3.4, the relationship between the PMD 1 signal and the mean intensity as measured by SCIAMACHY's science channel in the UVA region is linear. As can also be seen, the intensity, R_{SCI}, which corresponds to the PMD threshold SR_{PMD} = 0.7 is R_{SCI} = 0.1074. This relationship has been used in the following to assess the sensitivity of the PMD-based cloud detection algorithm to various cloud scenarios using RT simulations.

Simulated O_2 column retrievals have been used to determine the sensitivity of the O_2 column based cloud detection algorithm. This cloud detection algorithm works as follows: If the deviation between the retrieved and the a-priori O_2 column, defined as P_{O_2} =1-$O^{col}_{2,retrieved}/O^{col}_{2,a\text{-}priori}$, is larger than P_{O_2} = 10%, the corresponding SCIAMACHY pixel is flagged as cloudy.

For the RT simulations of the SCIAMACHY spectra the SCIATRAN RT code (Rozanov et al., 2005) has been used. The RT simulations are based on a standard scenario with an ice cloud. This scenario has been defined as follows: a cloud with fractal ice particles based on a tetrahedron with an edge length of 50 µm. Aerosols are considered by a realistic aerosol scenario, which is based on the OPAC clean continental aerosol type. The aerosols in the boundary layer and in the free troposphere are 99.998 % water soluble aerosols. The same extinction coefficient profile as shown in Fig. 2.15 and a Mie phase function are used.

Figure 3.5 shows simulated R_{SCI} and O_2 column differences between retrieved and a-priori columns, P_{O_2}, for different cloud fractional coverages (CFC) as a function of cloud optical depth (COD). The simulations are valid for a surface albedo of 0.1 and a solar zenith angle (SZA) of 40°. The red lines show the PMD and O_2 cloud detection thresholds. The sensitivity of the cloud detection algorithm for several cloud scenarios are shown by the intersection between the simulations and the (red) PMD and

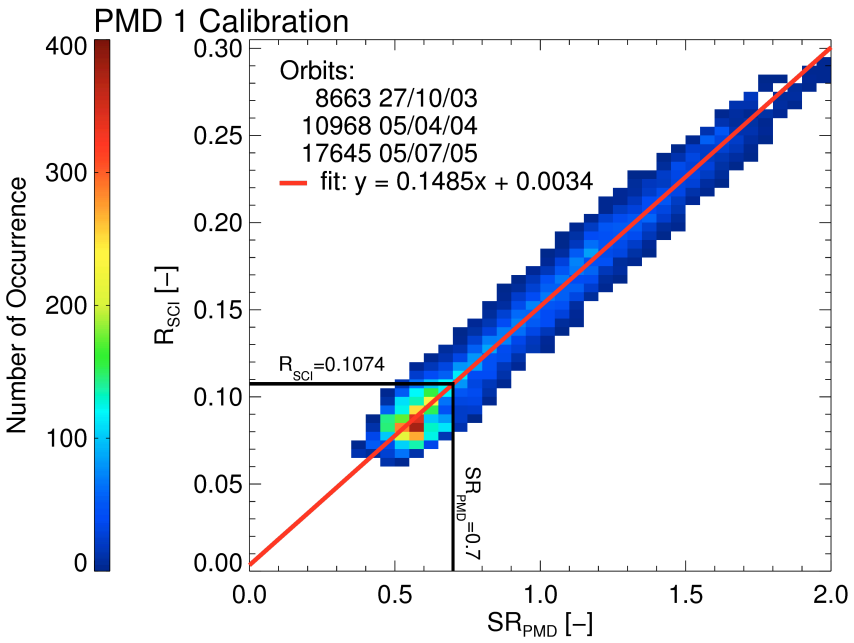

Figure 3.4: Calibration of the SCIAMACHY Polarisation Measurement Device number 1 (PMD 1) signal, covering the spectral region 310-365 nm based on three orbits (see annotation). SR_{PMD} is the uncalibrated normalised PMD 1 signal divided by the cosine of the solar zenith angle (SZA). R_{SCI} is the mean reflectivity (sun-normalised radiance divided by the cosine of the SZA) as measured by SCIAMACHY in a spectral region which corresponds to the spectral region covered by PMD 1.

O_2 threshold lines. As can be seen, minimum effective COD, i.e., the cloud detection thresholds, are 0.89 for the PMD algorithm and 0.07 for the O_2 algorithm.

This analysis has been repeated for different combinations of albedo, SZA and CTH. The results of these simulations are summarised in Tab. 3.1, which lists the sensitivities for different cloud and surface scenarios in terms of the minimum detectable eCOD. The surface scenarios correspond to the albedos of grass (UVA: 0.03; O_2-A: 0.46), water (UVA: 0.04; O_2-A: 0.02), sand (UVA: 0.01; O_2-A: 0.25) and snow (UVA: 0.97; O_2-A: 0.92) estimated from the ASTER (Advanced Spaceborne Thermal Emission and Reflection Radiometer) spectral library version 2.0 (Baldridge et al., 2009) and from the Digital Spectral Library 06 of the U.S. Geological Survey. In addition, a constant albedo of 0.1 has been used.

The simulations yield the following results: The PMD-based algorithm filters out thick clouds and bright surfaces in the UVA region like snow. The O_2 column based algorithm is typically more sensitive especially to high thin clouds. It needs to be

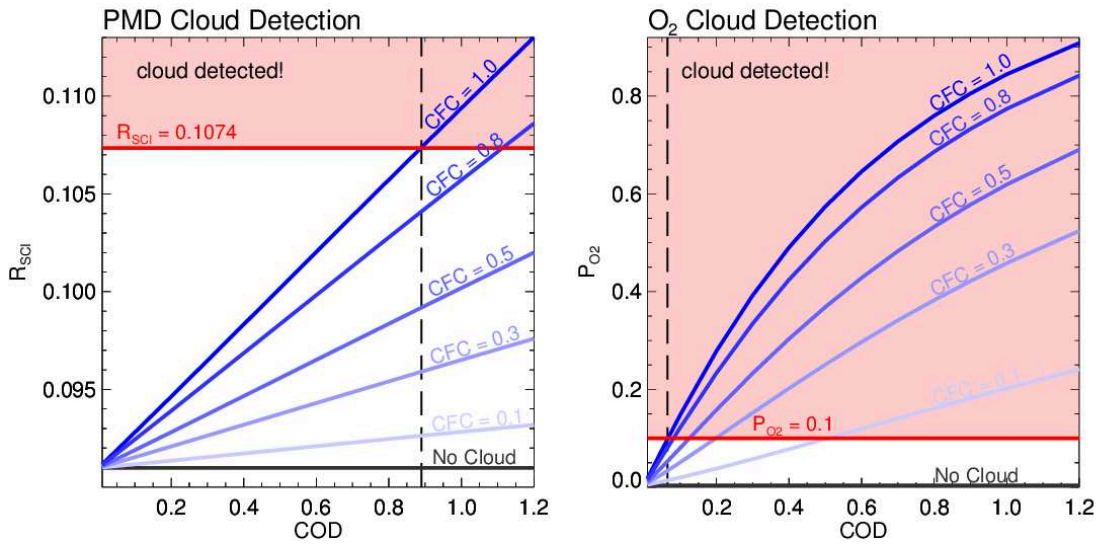

Figure 3.5: PMD (given as reflectivity, left) and O_2 (right) cloud detection thresholds (red lines) compared to results obtained from radiative transfer simulations and simulated retrievals for various cloud scenarios. The left panel shows simulated reflectivity R_{SCI} for the spectral region covered by PMD 1, as a function of cloud optical depth (COD) for different cloud fractional coverages (CFC). The results are valid for a surface albedo of 0.1, the default aerosol scenario, a cloud top height (CTH) of 10 km and a cloud geometrical thickness (CGT) of 0.5 km. The red line shows the PMD cloud detection criterion of R_{SCI} = 0.1074 and the black dashed line shows the minimum detectable COD for CFC = 1.0. The panel on the right shows the simulated deviation of the retrieved O_2 column to the a-priori O_2 column, i.e., P_{O2}, for the same parameters as used for the left hand side. The red line shows the O_2 cloud detection threshold P_{O2} = 0.1 and the black dashed line shows the minimum detectable COD for CFC = 1.0.

pointed out that this analysis is restricted to homogeneously cloud covered ground pixels as the focus of the investigation in Chap. 4 is on (horizontally extended) thin cirrus clouds. Because a SCIAMACHY main channel ground pixel includes several PMD subpixel, the PMD algorithm is typically more sensitive for cloud detection than indicated in Tab. 3.1. The PMD algorithm enables to detect optically thick but spatially small (i.e., subpixel) clouds (Buchwitz et al., 2005a). This aspect is not considered here. Table 3.1 shows that the sensitivity of the filter algorithms depends on the scene and on the SZA. As can be seen, thin clouds with eCOD of approximately less than 0.1 may remain undetected. This means that although a pixel is classified as cloud free by the WFMD cloud detection algorithm it may be contaminated by optically thin clouds such as subvisual cirrus clouds.

Minimum effective COD				
Scenario		CTH [km]		
Albedo/SZA		4	10	16
0.1/20°	PMD:	1.16	1.20	1.23
	O_2:	0.34	0.10	0.07
0.1/40°	PMD:	0.89	0.89	0.89
	O_2:	0.23	0.07	0.04
0.1/60°	PMD:	0.42	0.40	0.39
	O_2:	0.11	0.03	0.02
Grass/40°	PMD:	1.32	1.32	1.32
	O_2:	1.00	0.28	0.18
Sand/40°	PMD:	1.27	1.26	1.26
	O_2:	0.08	0.02	0.02
Water/40°	PMD:	1.43	1.42	1.42
	O_2:	0.53	0.15	0.10
Snow/40°	PMD:	0.00	0.00	0.00
	O_2:	∞	0.69	0.43

Table 3.1: Minimum detectable effective cloud optical depth (eCOD) for the PMD and O_2 based WFM-DOAS cloud detection algorithms for various scenarios as defined by surface albedo and solar zenith angle (SZA). The following settings have been used for all scenarios: aerosols: default scenario (see main text); clouds: cloud geometrical thickness CGT = 0.5 km and cloud fractional coverage CFC = 1.0. "∞" means that even clouds with large eCOD are not detected. "0.00" means that clouds are "detected" even if the scene is cloud free.

3.6 Viewing Geometry Correction

During the investigation of the impact of scattering by aerosols and clouds on the SCIAMACHY WFMDv2.1 XCO_2 data product, a scan-angle-dependent bias has been found. As explained, WFM-DOAS uses a fast LUT approach to avoid time consuming RT simulations. In order to generate a manageable LUT, it is needed to limit the number of LUT dimensions. For this reason, the LUT was computed for exact nadir viewing conditions (see Fig. 2.19), i.e., only a constant viewing zenith angle (VZA), also referred to as line of sight angle (LOS), of 0° is used. To correct for a scan-angle dependent airmass factor, a geometrical VZA correction has been implemented for the CO_2 and O_2 columns (Buchwitz and Burrows, 2004), but this does not correct the XCO_2, as this correction cancels out when the CO_2 to O_2 column ratio is computed.

As shown in Fig. 3.6 simulated WFM-DOAS retrievals have been used to investigate if the retrieved XCO_2 suffers from a scan-angle dependent bias. Figure 3.6 shows the systematic XCO_2 retrieval error as a function of VZA for different SZAs, albedos and AODs. As can be seen, the error can be as large as several ppm, especially for ground pixels with large positive VZAs (i.e., ground pixels west of the nadir position). As can also be seen, the simulations show an approximately quadratic dependence of the systematic error on the VZA. The reason for this dependence is the nonconsideration of the wavelength dependent scattering along the longer light paths at larger VZAs. The resulting systematic errors on the gas columns cannot be fully compensated by the normalisation of CO_2 by O_2.

The SCIAMACHY retrievals have been analysed based on measured satellite data to find out if this error can also be observed in the WFMDv2.1 XCO_2 data product. Figure 3.7 shows that this is the case. Figure 3.7a shows global, northern and southern hemispheric WFMDv2.1 XCO_2 for the years 2003 – 2009 as a function of the VZA. The 2D-histograms show the expected quadratic relation between the XCO_2 and the VZA. A similar result was also found for smaller regions (not shown here). As can also be seen, the magnitude of the difference between the most westwards and most eastwards XCO_2 amounts to several ppm and is on the same order of magnitude as also found using simulations (see above).

In the next subsection a method to correct for this bias is presented. In the following the (original, i.e., uncorrected) SCIAMACHY XCO_2 data set is denoted as XCO_2^S, the scan-angle-corrected SCIAMACHY XCO_2 is denoted $XCO_2^{S^*}$.

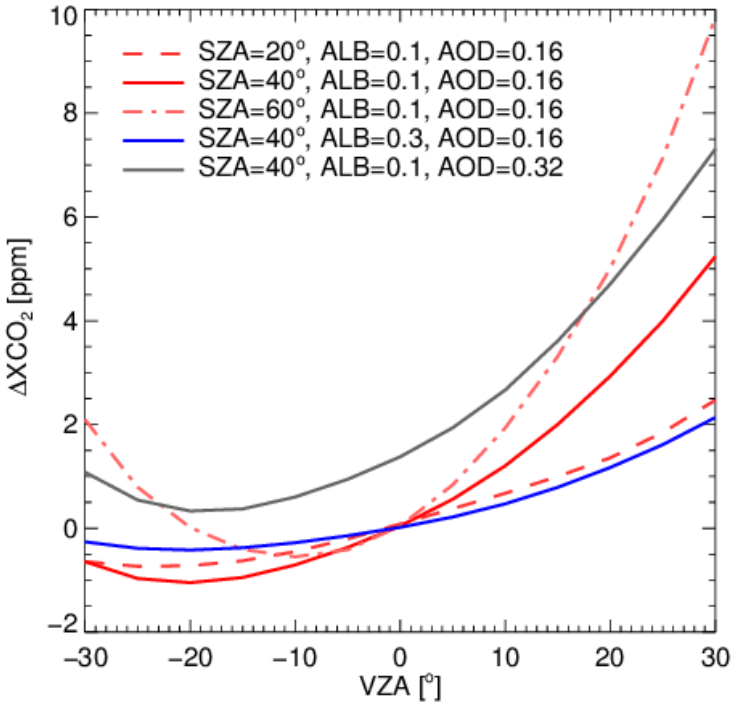

Figure 3.6: Simulated systematic WFM-DOAS XCO_2 errors (ΔXCO_2) for different viewing zenith angles (VZA). The simulations are for scenarios with different solar zenith angles (SZA), surface albedos (ALB) and aerosol optical depths (AOD) at 550 nm.

3.6.1 Correction Method

SCIAMACHY scans in nadir mode across-track with viewing zenith angles (VZA) between ±32° covering a total swath width of about 960 km. The VZA as given in the WFMDv2.1 Level 2 data product is between 0° and 32°, i.e., it is a positive number. The negative VZAs shown in Fig. 3.7 correspond to relative azimuth angles less than 100° (note that the azimuth angle is also given in the WFMDv2.1 XCO_2 L2 data product and that the SZA is less than 75° for WFMD after quality filtering). Negative VZAs correspond to ground pixels east of the nadir position ("east pixel"), positive VZAs correspond to ground pixels west of the nadir position ("west pixel").

A quadratic function depending on the (signed) VZA is fitted to XCO_2^S. Other functions have also be tried, e.g. a simple linear function, but the best fit is obtained with a quadratic function. The fit shown as blue curve in Fig. 3.7a is used to correct XCO_2^S in the following way:

$$XCO_2^{S^*} = XCO_2^S + \Delta XCO_2^{S^*-S} \tag{3.24}$$

$$\Delta XCO_2^{S^*-S} = C1 + C2 \cdot (VZA - C3)^2 \tag{3.25}$$

The VZA is given in degree and XCO_2 in ppm. The numerical values of the three parameters are: C1 = 7 ppm, C2 = $-0.003\ \frac{\text{ppm}}{\text{deg}^2}$ and C3 = -47.3 deg. They have been obtained from the global fit result (shown in Fig. 3.7a). The quality of this method is analysed in the next section.

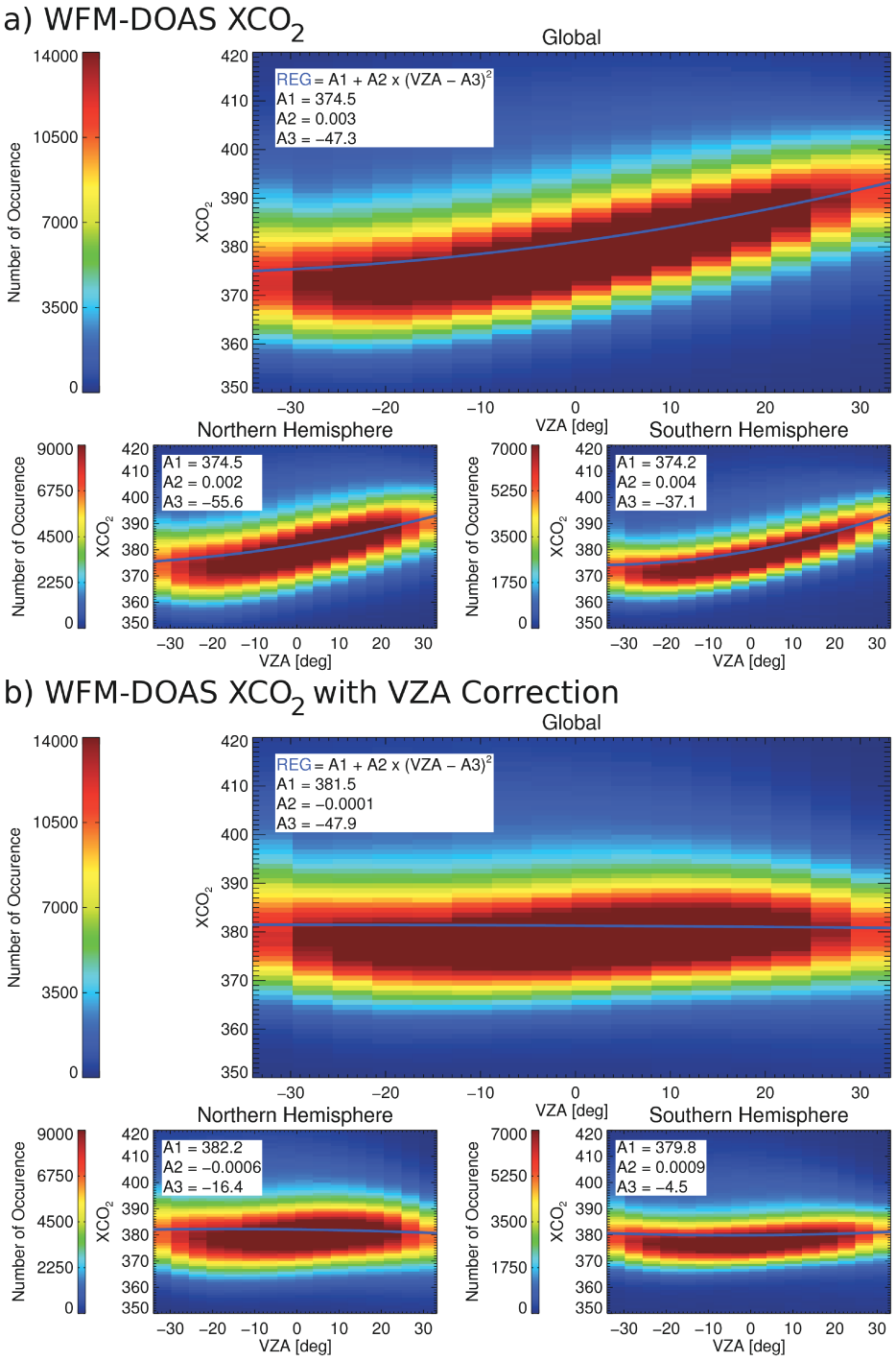

Figure 3.7: WFM-DOAS XCO_2 v2.1 VZA dependency before (a) and after (b) the scan-angle-bias correction. a) 2D-histogram of WFMDv2.1 XCO_2 versus the VZA using all data between 2003 and 2009. The blue curve is a quadratic fit. The fit parameter A1 is given in ppm, A2 in ppm/deg^2 and A3 is given in deg. b) As a) but after the bias correction.

3.6.2 Results

The scan-angle-bias corrected XCO_2 is shown in Fig. 3.7b. As can be seen, the dependency of XCO_2 on the VZA is reduced considerably, both on global (a reduction of the range of the scan-angle-dependent bias from ±9 ppm to ±1 ppm) and on hemispheric scales.

In order to investigate if the scan-angle-bias correction improves the SCIAMACHY WFMDv2.1 XCO_2 data set also on smaller scales, a regional comparison of corrected and uncorrected XCO_2 with NOAA's modelling and assimilation system, CarbonTracker (for more details see Sec. 4.1.1), XCO_2 has been performed. Here, CarbonTracker XCO_2 is denoted XCO_2^C.

For this purpose, sixteen regions have been defined, which are shown in Fig. 3.8 and listed in Tab. 3.2. Monthly means of the difference between SCIAMACHY WFMDv2.1 XCO_2 and CarbonTracker XCO_2 (ΔXCO_2^{S-C}) are used to determine the influence of the scan-angle-bias correction. Figure 3.9 shows the impact of the scan-angle-bias correction on ΔXCO_2^{S-C} for Southern Africa. As can be seen, the time series of $\Delta XCO_2^{S^*-C}$ (red curve with corrected XCO_2) and ΔXCO_2^{S-C} (black curve with uncorrected XCO_2) differ by up to about 1 ppm and show a significant correlation (linear correlation coefficient $r = 0.89$), which indicates that the phase of the seasonality of the XCO_2 difference does not change due to the scan-angle-bias correction. The correlation coefficient between $\Delta XCO_2^{S^*-S}$ and ΔXCO_2^{S-C} is also large (-0.76). The standard deviation of the difference to CarbonTracker is smaller for the corrected (1.05 ppm) than for the uncorrected XCO_2, i.e. the agreement with CarbonTracker is better for the corrected XCO_2 for this region. The variances of the standard deviations and the square of the correlation coefficient between $\Delta XCO_2^{S^*-S}$ and ΔXCO_2^{S-C} ($r^2 = 58$ %) show that about 60 % of ΔXCO_2^{S-C} can be explained by the scan-angle-bias for this region.

The seasonality of the scan-angle-bias correction in Southern Africa, as shown by the time series of $\Delta XCO_2^{S^*-S}$, can be explained by the following: The scan-angle-bias correction only depends on the VZA (Eq. 3.25). This means, that a seasonality of the scan-angle-bias correction is due to a seasonality of the VZA, which originates from the quality filtering. In the winter months (large SZA), more measurements under "large" VZA conditions are filtered out than in summer (small SZA). This may be related to a higher sensitivity under "large" SZA and "large" VZA conditions (longer light path) to scattering by aerosols and clouds and/or larger noise of the spectra. Together with the VZA asymmetry of the scan-angle-bias correction (Eq. 3.25 and Fig. 3.7), this can result in the observed seasonality.

The comparison results for the other regions are summarised in Tab. 3.3. The fig-

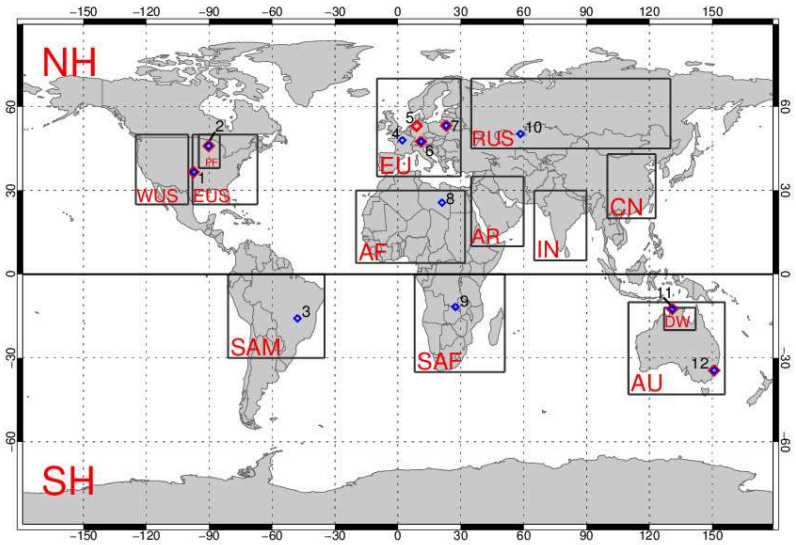

Figure 3.8: Regions and locations analysed in this manuscript (see also Tab. 3.2 and Tab. 3.4).

Region	ID	Latitude Range			Longitude Range		
Northern Hemisphere	NH	0°	–	90°	-180°	–	180°
Western USA	WUS	25°	–	50°	-125°	–	-100°
Eastern USA	EUS	25°	–	50°	-98°	–	-67°
Park Falls	PF	38°	–	50°	-95°	–	-85°
Europe	EU	35°	–	70°	-10°	–	30°
Northern Africa	AF	4°	–	30°	-20°	–	32°
Arabia	AR	10°	–	35°	35°	–	60°
Russia	RUS	45°	–	70°	35°	–	130°
India	IN	5°	–	30°	65°	–	90°
China	CN	20°	–	43°	100°	–	123°
Southern Hemisphere	SH	-90°	–	0°	-180°	–	180°
South America	SAM	-30°	–	0°	-81°	–	-35°
Southern Africa	SAF	-35°	–	0°	8°	–	51°
Australia	AU	-43°	–	-10°	110°	–	156°
Darwin	DW	-20°	–	-12°	127°	–	142°
Global	G	-90°	–	90°	-180°	–	180°

Table 3.2: Latitudes and longitudes of the regions used in this study (see also Fig. 3.8).

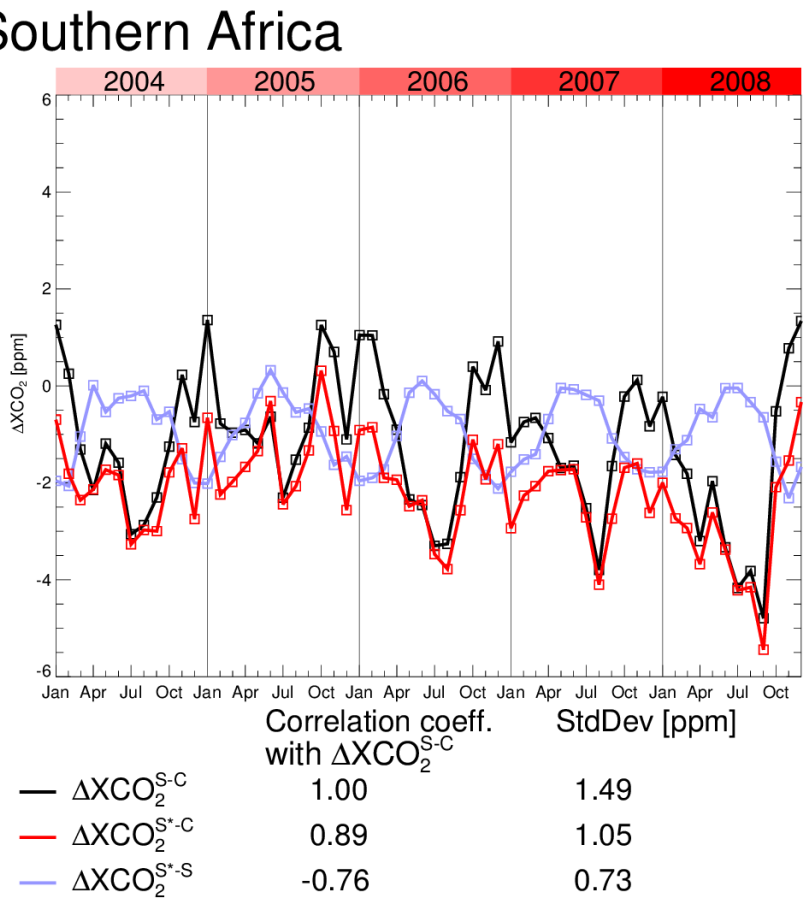

Figure 3.9: Results of the comparison between CarbonTracker XCO_2 and WFMDv2.1 XCO_2 with and without scan-angle-bias correction for Southern Africa. Top: The difference between WFMDv2.1 XCO_2 and CarbonTracker XCO_2 ($\Delta XCO_2^{S\text{-}C}$) is shown in black and the difference between the scan-angle-bias corrected WFMDv2.1 XCO_2 and CarbonTracker XCO_2 ($\Delta XCO_2^{S^*\text{-}C}$) is shown in red. The light blue curve represents the difference between scan-angle-bias corrected WFMDv2.1 XCO_2 and uncorrected XCO_2 ($\Delta XCO_2^{S^*\text{-}S}$). Bottom: Correlation coefficients (r) between these differences and $\Delta XCO_2^{S\text{-}C}$ and corresponding standard deviations.

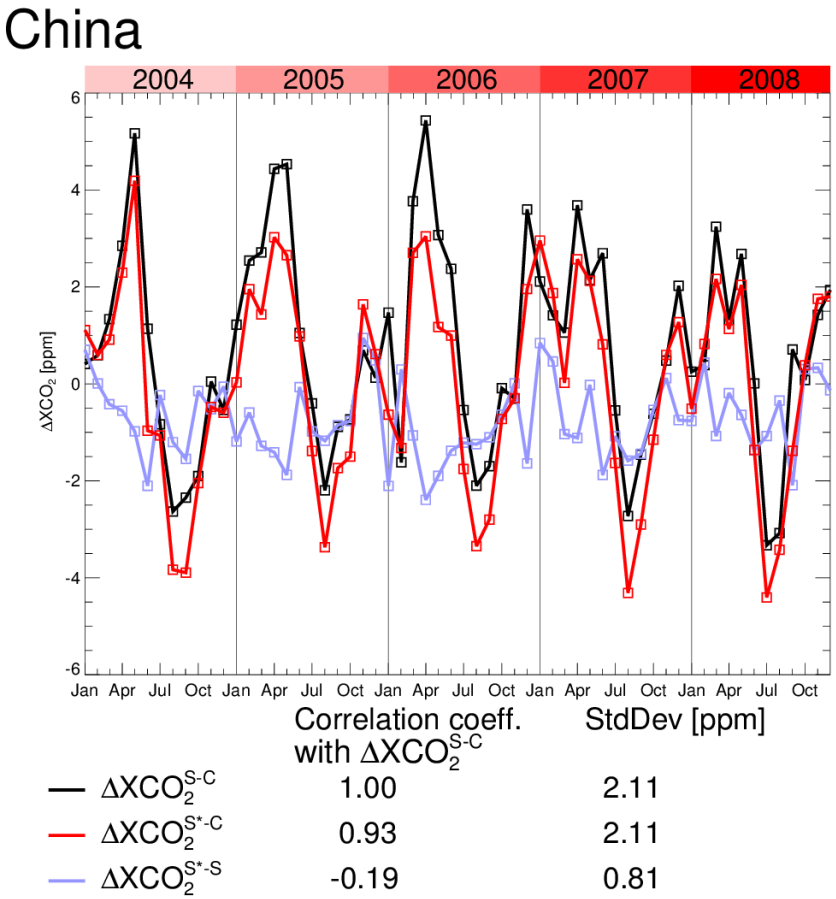

Figure 3.10: As Fig. 3.9 but for China.

ures to this comparison can be found in App. A. The time dependence of $\Delta XCO_2^{S^*-C}$ is similar as ΔXCO_2^{S-C} for all regions. This is shown by the large correlation coefficients, which are between 0.68 and 0.99. The correlation with $\Delta XCO_2^{S^*-S}$ is large for many regions, but for several northern hemispheric regions very small and/or non-significant. An example is China, shown in Fig. 3.10, where the large difference to CarbonTracker cannot be explained by the scan-angle related bias. The global correlation and standard deviation shows that the scan-angle-correction affects the XCO_2 data set mostly on smaller regional scales. The standard deviations of XCO_2^{S-C} are improved using the correction over all southern hemispheric regions and for most northern hemispheric regions.

To further quantify the improvements due to the scan-angle-bias correction, the standard deviation of all XCO_2 single ground pixel measurements within a radius of 350 km around several locations for each month were computed. The location

Region	Correlation of ΔXCO_2^{S-C} with $\Delta XCO_2^{S^*-C}$	Correlation of ΔXCO_2^{S-C} with $\Delta XCO_2^{S^*-S}$	Standard deviation [ppm] ΔXCO_2^{S-C}	Standard deviation [ppm] $\Delta XCO_2^{S^*-C}$	Standard deviation [ppm] $\Delta XCO_2^{S^*-S}$
NH	0.90	*0.04*	1.11	1.26	0.56
WUS	0.82	−0.30	1.86	1.85	1.10
EUS	0.84	−0.82	2.77	1.72	1.63
PF	0.68	−0.86	2.51	1.30	1.88
EU	0.84	*0.01*	1.43	1.72	0.94
AF	0.77	−0.64	1.17	0.90	0.75
AR	0.90	−0.45	1.59	1.42	0.68
RUS	0.80	−0.58	2.00	1.62	1.19
IN	0.99	−0.85	4.86	3.97	1.10
CN	0.93	*−0.19*	2.11	2.11	0.81
SH	0.90	−0.82	1.62	1.06	0.82
SAM	0.92	−0.67	1.96	1.54	0.80
SAF	0.89	−0.76	1.49	1.05	0.73
AU	0.71	−0.80	1.87	1.14	1.34
DW	0.95	−0.78	4.00	2.99	1.50
G	0.98	−0.23	1.14	1.11	0.22

Table 3.3: Results of the comparison of the scan-angle-bias corrected (S*) and uncorrected (S) SCIAMACHY WFMDv2.1 XCO_2 with CarbonTracker (C). Listed are correlation coefficients (r, left) and standard deviations (right). Italic correlation coefficients are non-significant. The results shown are based on monthly data.

of these sites are shown in Fig. 3.8 and listed in Tab. 3.4. The mean values of these standard deviations may be interpreted as an upper limit of the single measurement precision (random error). The real precision is likely smaller because the standard deviations are not only due to instrument and retrieval noise but also affected by real atmospheric XCO_2 variability (note that variations due to the seasonal cycle have largely been filtered out by using standard deviations of all data in a given month) and varying systematic errors, e.g., due to the scan-angle-dependent bias. Table 3.4 shows absolute (in ppm) and relative (percentage) standard deviations of WFMDv2.1 XCO_2 with and without scan-angle-bias correction. As can be seen, the standard deviation is somewhat smaller for the scan-angle-bias corrected data for all locations. The intra-monthly standard deviation of XCO_2 is on average 9.04±1.51 ppm for the uncorrected data and is reduced to 7.42±1.29 ppm for the corrected data.

Monthly regional-scale scatter of the data							
ID	Location	Lat [°]	Lon [°]	XCO_2^S		$XCO_2^{S^*}$	
				[ppm]	[%]	[ppm]	[%]
1	Lamont	36.6	−97.5	9.24	2.43	7.56	1.99
2	Park Falls	46.0	−90.3	9.68	2.54	7.65	2.01
3	Brasilia	−15.8	−47.9	9.75	2.55	8.26	2.16
4	Orleans	48.0	2.1	7.69	2.01	6.28	1.64
5	Garmisch	47.5	11.1	9.53	2.51	8.09	2.14
6	Bialystok	53.2	23.0	7.62	1.99	6.09	1.59
7	Tazirbu	25.7	21.4	5.60	1.47	4.95	1.30
8	Lubumbashi	−11.7	27.5	10.72	2.82	9.09	2.39
9	Khromtau	50.3	58.5	10.77	2.83	9.23	2.43
10	Darwin	−12.4	130.9	9.42	2.47	7.21	1.89
11	Wollongong	−34.4	150.9	9.38	2.47	7.17	1.89
	Mean			9.04 ± 1.51	2.37 ± 0.40	7.42 ± 1.29	1.95 ± 0.34

Table 3.4: Monthly regional-scale scatter (in ppm and %) of the scan-angle-bias corrected (S*) and uncorrected (S) WFMDv2.1 XCO_2 data obtained from analysing all individual XCO_2 retrievals within a radius of 350 km around various locations. The numerical values are the mean standard deviations of all SCIAMACHY retrievals per month (to remove the seasonal cycle).

Schneising et al. (2012) validated the scan-angle-corrected SCIAMACHY XCO_2 data product against FTS measurements of TCCON. They found a regional precision (defined as the mean standard deviation of the monthly differences to the TCCON FTS measurements within a radius of 500 km) of 2.1 ppm and a regional accuracy of 1.1 ppm. However, the difference to the validation results of the uncorrected XCO_2 data is not significant.

4 Comparison of SCIAMACHY and CarbonTracker XCO_2 Focusing on Aerosols and Thin Clouds

In this chapter, results of a comparison between the SCIAMACHY WFM-DOAS version 2.1 (WFMDv2.1) XCO_2 data set covering the period 2003 – 2009 and CarbonTracker version 2010 is presented, which is partly adapted from Heymann et al. (2012a). In an initial comparison of WFMDv2.1 XCO_2 with CarbonTracker, Schneising et al. (2011) and Schneising et al. (2012) have already showed good agreements between the observed and modelled global increase of atmospheric CO_2 and a good reproduction of the seasonal cycle over the Northern Hemisphere. A comparison of the boreal forest uptake during the growing season by analysing longitudinal gradients shows also good agreements with the model. However, the observed amplitude of the northern hemispheric seasonal cycle is larger than for CarbonTracker. This corroborates the findings of Yang et al. (2007), Keppel-Aleks et al. (2012), Messerschmidt et al. (2012) and Reuter et al. (2012b). The reason for this difference can be an underestimation of the net ecosystem exchange (NEE) between the atmosphere and the biosphere by the CASA (Carnegie-Ames Stanford Approach) biosphere model, which is used for CarbonTracker.

A comparison with the FTS measurements from TCCON shows good agreements over the Northern Hemisphere (Schneising et al., 2012). Over the Southern Hemisphere large differences to CarbonTracker and also to TCCON were observed. The phase of the seasonal cycle over the Southern Hemisphere shows a shift between the SCIAMACHY measurements and CarbonTracker XCO_2. Furthermore, the satellite measurements, e.g., over Darwin show large differences to the TCCON FTS measurements. The reason for this discrepancies can be scattering due to aerosols and unaccounted thin clouds.

In order to explain these differences to TCCON, the focus of the comparison presented in this chapter is on the identification and quantification of systematic retrieval errors caused by aerosols and unaccounted clouds. Schneising et al. (2008) presented an initial assessment of XCO_2 errors due to aerosols and clouds mostly based on

simulated retrievals using WFMDv1.0. Here, an analysis of the difference between measured satellite data (WFMDv2.1) and model output are presented and the difference is compared with global aerosol and cloud data sets based on measurements.

4.1 Description of Global Data Sets

In this section the global data sets which have been used for the comparison with the SCIAMACHY WFM-DOAS XCO_2 data product are described.

4.1.1 CarbonTracker XCO_2

In order to obtain estimates for CO_2 surface fluxes and global atmospheric CO_2 distributions from NOAA's highly accurate and precise greenhouse gas air sampling network, NOAA has developed the global CO_2 assimilation and modelling system CarbonTracker (Peters et al., 2007).

The CarbonTracker model includes atmospheric transport based on weather forecast, a biosphere module for the consideration of photosynthesis and respiration, a module for the sea-air exchange and a module for CO_2 released from fires and from the combustion of fossil fuel. Within the assimilation process, the model results of CarbonTracker are compared with the measurements from the air sampling network. The differences are interpreted as differences from the a-priori model fluxes to the real fluxes. The adaptation of the model fluxes to the observations leads typically to improved and less uncertain fluxes. However, this depends not only on the amount and uncertainty of the assimilated observations but also on the quality of the model. The assimilation process can be used to estimate the anthropogenic and natural contributions to the atmospheric CO_2 concentration and leads to predictions of atmospheric CO_2 mole fractions and fluxes from CO_2 sources and sinks.

CarbonTracker version 2010 data of the years 2003 – 2009 obtained from http://carbontracker.noaa.gov is used for the comparisons with SCIAMACHY XCO_2. In order to consider the altitude sensitivity of the SCIAMACHY WFMD XCO_2 retrievals, the WFMD XCO_2 averaging kernels are applied to the CarbonTracker CO_2 vertical profiles. These profiles are integrated vertically to obtain appropriate CarbonTracker XCO_2. The corresponding CarbonTracker seasonal XCO_2 averages are shown in
Fig. 4.1. The daily CarbonTracker XCO_2 data set has been regridded on a $0.5°\times0.5°$ longitude/latitude grid and sampled like SCIAMACHY.

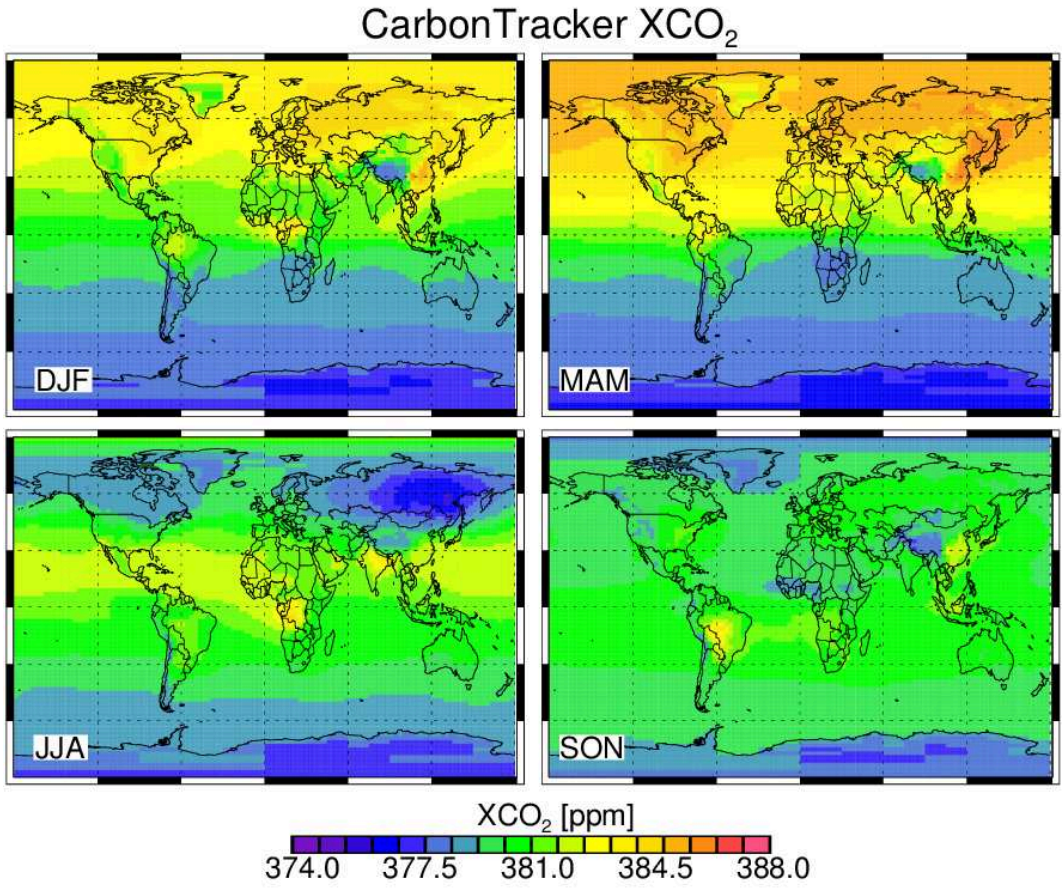

Figure 4.1: Seasonal averages of NOAA's CarbonTracker XCO_2 for 2004 – 2008, modified to take SCIAMACHY's CO_2 column averaging kernels into account.

4.1.2 Global Information on Aerosols

For global information on aerosols, a data set generated within the European GEMS (Global and regional Earth-system Monitoring using Satellite and in-situ data) project (Benedetti et al., 2009; Morcrette et al., 2009) is used.

The GEMS aerosol product is based on the 4D-VAR (four-dimensional variational) assimilation of MODIS (MODerate resolution Imaging Spectroradiometer) (Barnes et al., 1998) information into a global model (Benedetti et al., 2009; Morcrette et al., 2009). The model includes emissions of dust, sea-salt, black carbon, organic carbon and sulphate aerosols. In addition, also weather dependent sources of dust and salt and fire emissions estimated from satellite measurements are included.

The data set has been obtained from the web page http://data-portal.ecmwf.int/data/d/gems_reanalysis/. It covers the years

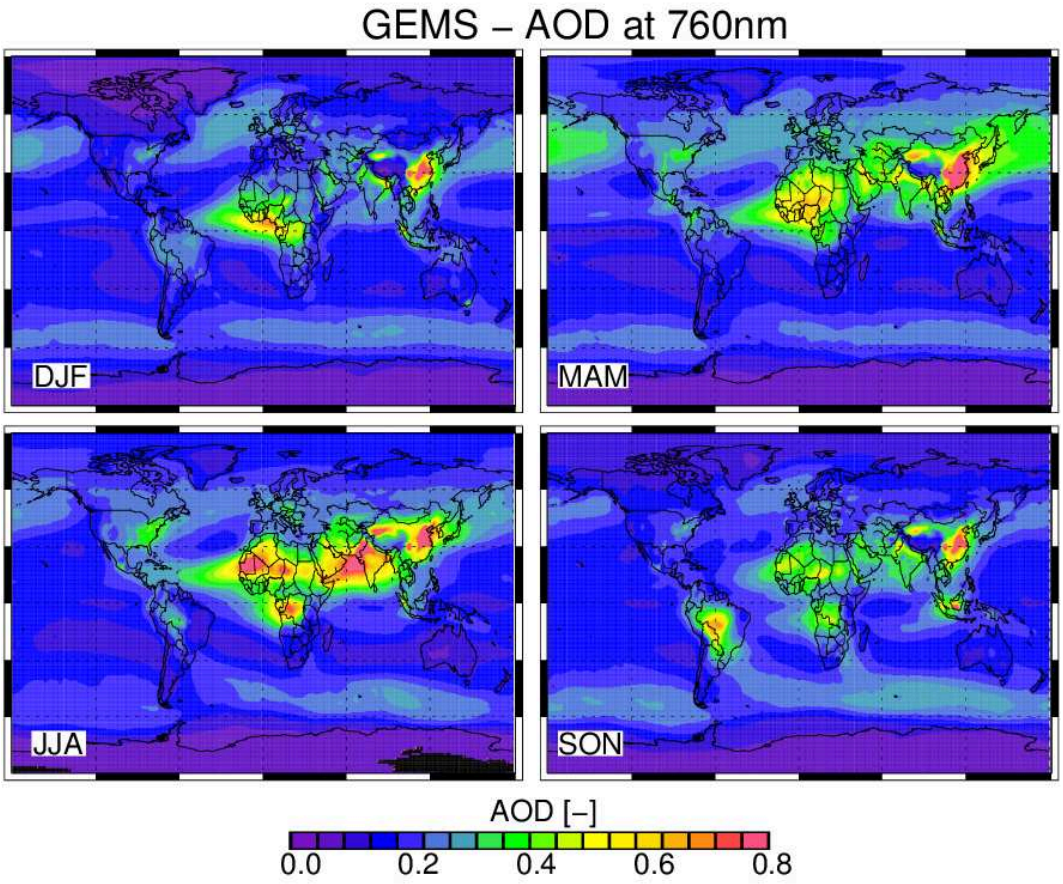

Figure 4.2: Seasonal averages of aerosol optical depth (AOD) at 760 nm based on the GEMS aerosol data product of the years 2004 – 2008.

2004 – 2008 and provides homogeneous and consistent aerosol information in 12 hourly time steps with full global coverage. For the analysis, the data set has been prepared to coincide temporally with SCIAMACHY by linear temporal interpolation. Ångstrom coefficients have been calculated using the original GEMS wavelengths (550 nm, 670 nm and 865 nm) and utilised to estimate aerosol optical depth (AOD) at 760 nm as needed for this study. The spatial resolution of the original data set is 1.125°×1.125°. This data set has been regridded on a 0.5°×0.5° longitude/latitude grid as also done for the CarbonTracker XCO_2 as described above. Seasonal averages of the resulting AOD at 760 nm are shown in Fig. 4.2. For the comparison with the difference between SCIAMACHY and CarbonTracker XCO_2, the aerosol data have also been sampled like SCIAMACHY.

4.1.3 Global Information on Clouds

Global information on thin clouds derived from CALIOP (Cloud-Aerosol Lidar in Orthogonal Polarisation) on-board CALIPSO (Cloud-Aerosol Lidar and Infrared Pathfinder Satellite Observations) has been used in this study because CALIOP is sensitive to subvisual cirrus clouds (Vaughan et al., 2004; Winker et al., 2007, 2009). CALIPSO is a satellite in the A-Train constellation and was launched in April 2006. CALIPSO delivers information about the global distribution and properties of aerosols and clouds. The CALIOP instrument is a near-nadir viewing two-wavelength (1064 nm and 532 nm) polarisation-sensitive LIDAR, which provides active measurements of these aerosol and cloud properties night and day.

The CALIPSO data product (CAL_LID_L2_05kmCLay-Prov-V3-01) provides information on COD with a horizontal resolution of 5 km by 70 m. A two-year daytime data set has been used for this study (2007 and 2008). The cloud statistics based on a two-year daytime CALIOP data set (2007 and 2008) is used primarily due to the narrow swath of CALIPSO (70 m) compared to SCIAMACHY (960 km) and the lower resolution of SCIAMACHY (30 km by 60 km). In addition, CALIPSO flies on a different orbit and was launched later than SCIAMACHY.

The investigation of the sensitivity of the WFM-DOAS cloud detection algorithm presented in Sec. 3.5 showed that ground pixels classified cloud free may still be contaminated by thin clouds with an effective optical depth of up to approximately eCOD = 0.1. Therefore, the CALIPSO data have been filtered to keep only scenes with COD = 0.1 or less. Using averaging and interpolation, monthly maps of cloud parameters (COD) have been generated with global coverage and a spatial resolution of 0.5°×0.5°. The CALIPSO data set only provides binary information about cloud coverage. Consequently, the relative frequency of cloud occurrence has been computed for every gridbox and is used as CFC data set. Using CALIPSO derived COD and CFC, eCOD (= COD·CFC) has been computed. The corresponding seasonal averages of CALIPSO derived eCOD are shown in Fig. 4.3. In order to obtain daily cloud information without gaps, the monthly data are used as daily data in the respective month. These daily CALIPSO data are sampled in the same manner as the daily data of the other data sets. The monthly means of the years 2007 – 2008 are used for the years 2004 – 2006, where no CALIPSO data are available. Note that due to the interpolation and averaging of the CALIPSO data only statistical evidence can be given and the data set should not be used on single measurement scale.

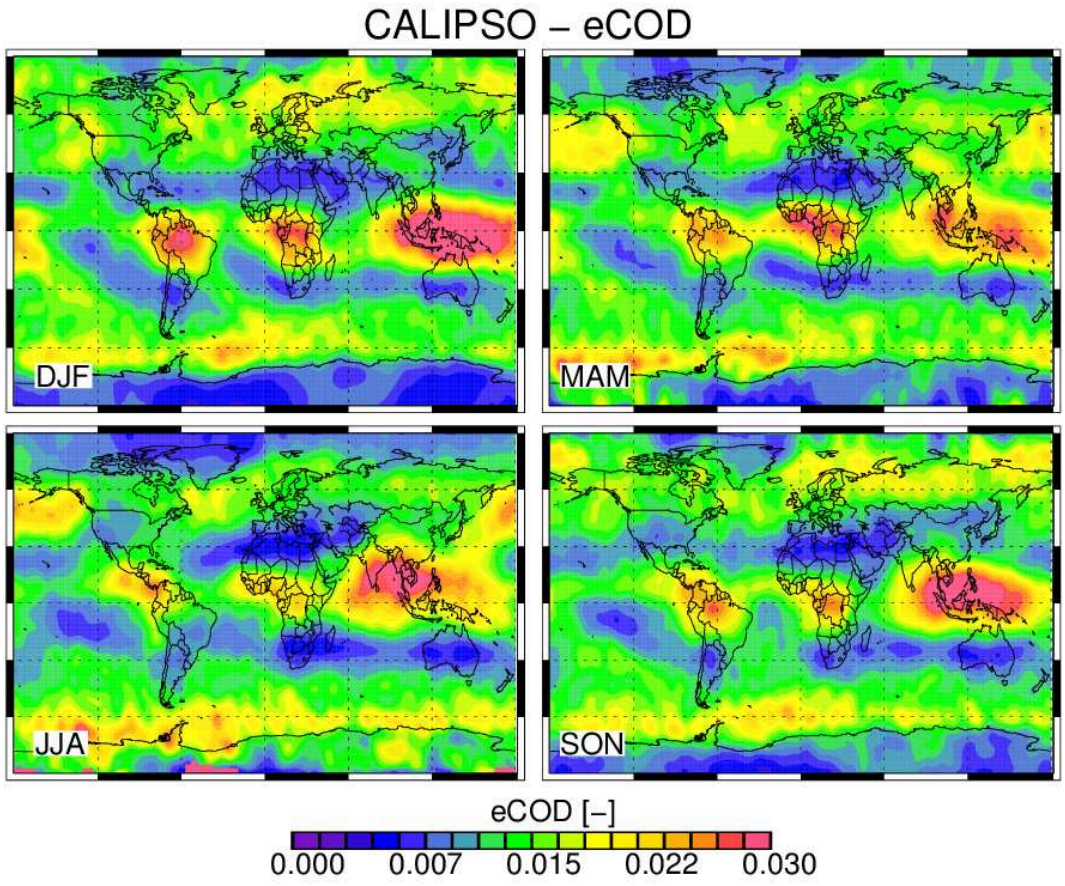

Figure 4.3: Seasonal averages of effective cloud optical depth (eCOD) obtained from 2007/2008 CALIPSO/CALIOP data for clouds with COD less than 0.1.

4.2 Analysis Method

The investigation method is a temporal and spatial correlation analysis. For this analysis, the SCIAMACHY WFMDv2.1 XCO_2 Level 2 data product of Schneising et al. (2011) is used, which cover the time period 2003 – 2009. For the investigation of SCIAMACHY minus CarbonTracker differences, only data from the time period 2004 – 2008 are used. 2003 data are not utilised because of instrumental issues at the beginning of 2003 (Schneising et al., 2011). 2009 is excluded because the used aerosol reference data is only available until mid 2009.

The three global data sets described in Sec. 4.1 and Sec. 3.6 have been used for a temporal and spatial correlation analysis: (i) the scan-angle-bias corrected SCIAMACHY - CarbonTracker difference, denoted $XCO_2^{S^*-C}$, (ii) the AOD at 760 nm

as derived from the GEMS aerosol product, and (iii) CALIPSO derived eCOD.

Monthly averages are the input for the temporal correlation analysis. For the spatial analysis, averages of the four meteorological seasons (DJF, MAM, JJA and SON) of the five years 2004 – 2008 are used instead of monthly averages for a better spatial coverage. These averages were used to reduce the scatter of the satellite data. In addition, the resolution has been reduced to 1°×1° for the spatial analysis.

In order to test whether a correlation is significant or not, a t-test is being performed. For this reason, a test statistic t' based on the number of the data points n and the correlation coefficient r is computed:

$$t' = \frac{r\sqrt{n-2}}{\sqrt{1-r^2}} \tag{4.1}$$

To decide whether the correlation coefficient is significant or not, the resulting t' is compared with the t from a t-table, $t(f,p)$, which depends on the degree of freedom $f = n-2$ and the probability value p. p is the probability that the correlation is statistically firm and is set to 95%. If t' is greater than $t(f,p)$, the correlation coefficient is regarded to be significant.

4.3 Analysis Results

The results of the temporal and spatial correlation analysis for China are shown in Fig. 4.4. The amplitude of the seasonal cycle is larger for SCIAMACHY compared to CarbonTracker. To a minor extent (r^2 = 9.2 %), the difference may be due to retrieval errors caused by thin clouds. The spatial analysis shows that in autumn 33 % of the variability of $\Delta XCO_2^{S^*-C}$ may be explained by eCOD, i.e. clouds related retrieval errors. The AOD over China is the highest of all investigated regions, therefore one would expect to find also the largest correlation. However, this analysis only shows low temporal and spatial correlations with aerosols. This may indicate that aerosols are not a significant problem for the WFMDv2.1 algorithm in this region. On the other hand it needs to be considered that CarbonTracker is not perfect, e.g., the mentioned indications for an underestimation of the net ecosystem exchange (NEE) between the atmosphere and the biosphere by the underlying CASA (Carnegie-Ames Stanford Approach) biosphere model. In order to investigate the impact of this underestimation on the results, the same analysis with a 40 % scaled CarbonTracker amplitude for all regions have been performed. It was found that the correlations are similar for most regions and the conclusions are the same as for the unscaled CarbonTracker

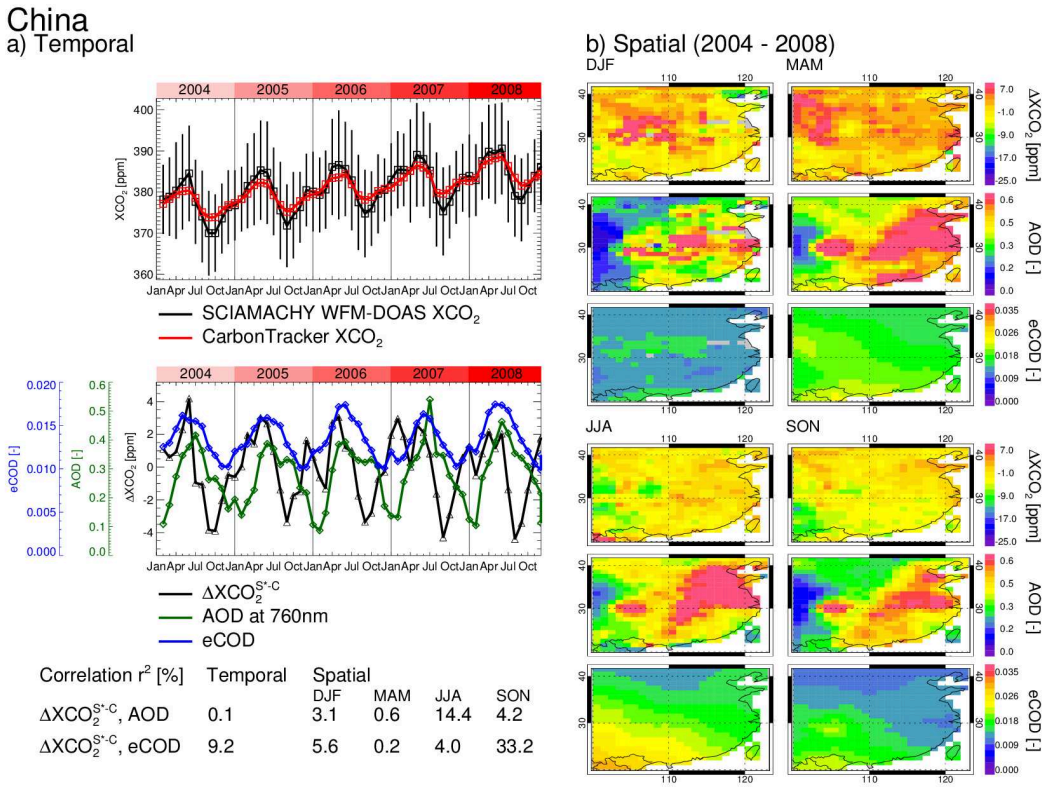

Figure 4.4: Results of the temporal and spatial correlation analysis of the difference between scan-angle-corrected SCIAMACHY and CarbonTracker XCO_2, i.e., $\Delta XCO_2^{S^*\text{-}C}$, and aerosols and thin clouds for China. a) Temporal analysis part: Top: The monthly means and standard deviations of the WFMDv2.1 XCO_2 are shown in black and CarbonTracker XCO_2 is shown in red. Middle: $\Delta XCO_2^{S^*\text{-}C}$ (black) compared with GEMS-derived AOD at 760 nm (green) and CALIPSO-derived eCOD (blue). Bottom left: The squares of the linear correlation coefficients, r^2, of the temporal and spatial correlation analysis. b) Spatial analysis part: Three-year seasonal averages of $\Delta XCO_2^{S^*\text{-}C}$, AOD and eCOD.

amplitude.

Figure 4.5 shows the corresponding results for Southern Africa. As can be seen, the amplitude of the difference is about 4 ppm. Neither a "U-shape", as mentioned by (Schneising et al., 2008) for the seasonal cycle of the southern hemispheric WFMDv1.0 XCO_2, nor an evident phase shift between the seasonal cycle of $XCO_2^{S^*}$ and XCO_2^{C} can be seen in this region. However, Fig. 4.5 shows that 31 % of the temporal variability of $\Delta XCO_2^{S^*-C}$ may be explained by thin clouds. A larger temporal correlation ($r^2 = 55\%$) has been found for the time period 2007 – 2008 (the cloud statistics are based on CALIPSO measurements from these years). The temporal correlation of $\Delta XCO_2^{S^*-C}$ with aerosols is statistically not significant in this region. The spatial correlation analysis shows that there are some correlations between $\Delta XCO_2^{S^*-C}$ and eCOD and also with AOD. The largest influence of clouds and aerosols on the difference is during spring (MAM).

The corresponding results of the spatial and temporal correlation analysis for all regions investigated are summarised in Table 4.1 and are presented in App. B. Many regions over the Northern Hemisphere show low spatial correlations with aerosols and clouds ($r^2 < 25$ %). Due to high aerosol loads not only in China, as can be seen by the yellow to red areas in Fig. 4.2, e.g., over Africa, Southern Africa, Arabia and India, one would expect high spatial and temporal correlations over these regions. However, the only regions, where large spatial correlations can be found are Arabia (35 % during summer), Africa (26 % during summer) and Southern Africa (34 % during spring). A large temporal correlation with aerosol can only be found for India (54 %). Large spatial correlations with thin clouds are found over the Northern Hemisphere, e.g., for Africa during spring (MAM). For the Southern Hemisphere, the spatial correlations with thin clouds often exceed 25 %. The largest spatial correlation is found for Australia (48 % during DJF) indicating that a large part of the spatial variability of the XCO_2 difference in this season can be explained by thin clouds.

Temporal correlations with eCOD are typically large for several regions over the Southern Hemisphere and typically low over the Northern Hemisphere with the exception of India. Figure 4.3 shows that thin clouds often occur in the tropics. Therefore, one would expect the largest impact of thin clouds on the XCO_2 difference over tropical regions. This is confirmed by the correlations over India and especially over the Southern Hemisphere (most of the landmasses of the Southern Hemisphere are in the tropics). The results also corroborate the assumption of Schneising et al. (2011) that the differences between SCIAMACHY WMFDv2.1 and CarbonTracker XCO_2 over the Southern Hemisphere are likely due to unaccounted thin clouds. The low temporal and spatial correlations with aerosols for many regions show that aerosols likely only marginally contribute to the observed difference to CarbonTracker.

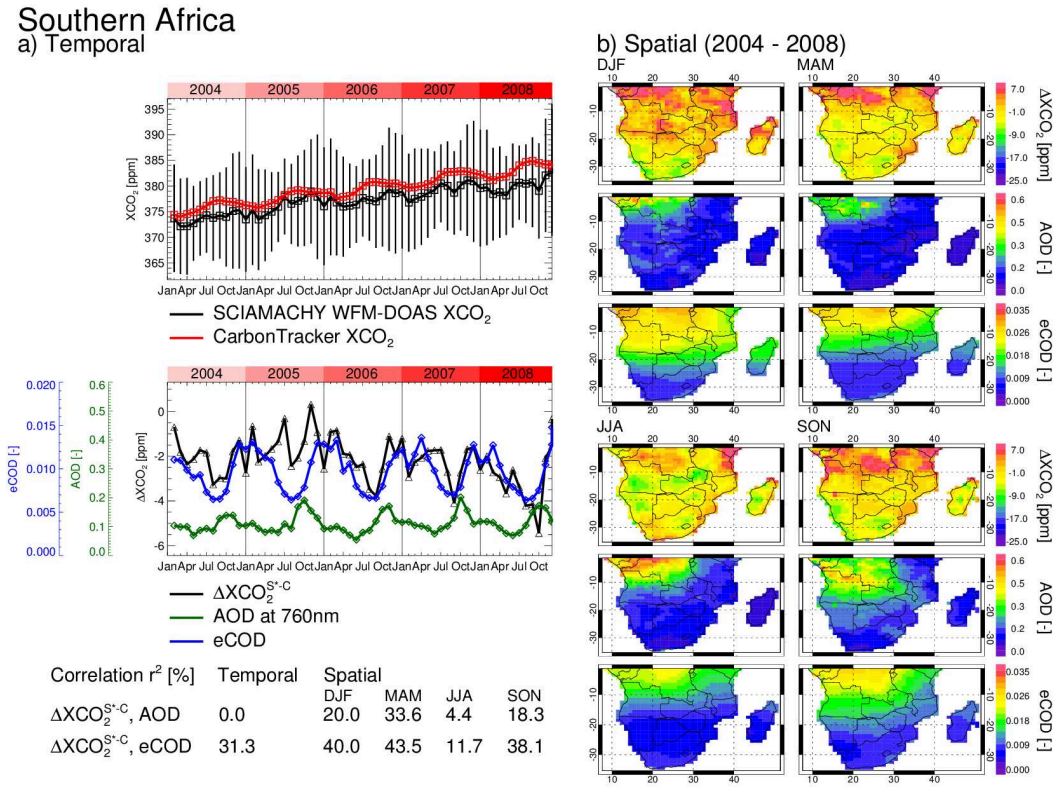

Figure 4.5: As Fig. 4.4 but for Southern Africa.

Correlation coefficients r^2 [%]						
Region	Correlation of $\Delta XCO_2^{S^*-C}$ with	Temporal	Spatial			
			DJF	MAM	JJA	SON
Northern Hemisphere						
WUS	AOD:	9.0	1.7	8.4	**25.0**	5.3
	eCOD:	*3.2*	4.4	**30.3**	2.0	6.2
EUS	AOD:	7.5	7.8	1.1	0.8	4.3
	eCOD:	*1.7*	5.5	*0.2*	0.8	0.8
PF	AOD:	6.9	*1.2*	*1.1*	14.1	9.0
	eCOD:	*2.3*	*0.0*	**29.7**	**30.2**	**32.9**
EU	AOD:	*0.8*	*0.7*	1.5	*0.3*	0.6
	eCOD:	*0.4*	22.4	*0.1*	3.4	*0.3*
AF	AOD:	15.0	14.7	6.5	**26.1**	3.7
	eCOD:	*0.5*	17.3	**38.2**	2.5	0.4
AR	AOD:	18.3	*0.0*	*0.3*	**34.5**	*0.0*
	eCOD:	15.8	6.0	*0.0*	**32.9**	2.6
RUS	AOD:	20.3	*0.8*	14.6	0.4	2.4
	eCOD:	17.4	**25.0**	7.6	0.3	0.2
IN	AOD:	**54.0**	8.2	1.5	12.8	21.9
	eCOD:	**67.9**	2.0	2.5	4.9	6.9
CN	AOD:	*0.1*	3.1	0.6	14.4	4.2
	eCOD:	9.2	5.6	*0.2*	4.0	**33.2**
Southern Hemisphere						
SAM	AOD:	19.2	2.5	3.4	9.8	9.5
	eCOD:	**42.9**	19.5	15.5	1.8	14.8
SAF	AOD:	*0.0*	20.0	**33.6**	4.4	18.3
	eCOD:	**31.3**	**40.0**	**43.5**	11.7	**38.1**
AU	AOD:	*0.3*	1.4	17.3	**36.2**	19.0
	eCOD:	**28.4**	**48.4**	2.2	0.8	10.2
DW	AOD:	16.7	12.4	3.5	10.3	**34.9**
	eCOD:	**53.7**	**29.5**	**30.6**	3.4	**45.7**

Table 4.1: Results of the spatial and temporal correlation analysis of $\Delta XCO_2^{S^*-C}$ related to aerosols (AOD) and clouds (eCOD). Italic coefficients are statistically non-significant. The coefficients, which indicate that aerosols or clouds can explain more than 25% of the variability of $\Delta XCO_2^{S^*-C}$, are shown in bold. The results shown are based on monthly data.

5 SCIAMACHY WFM-DOAS Version 2.2 XCO_2

The results of the last chapter show that the presence of thin clouds potentially explain a significant fraction of the difference between SCIAMACHY WFMDv2.1 XCO_2 and CarbonTracker especially over the Southern Hemisphere. This indicates that the quality of the satellite derived XCO_2 will significantly benefit from a reduction of scattering related retrieval errors. This is the focus of this chapter, which is partly adapted from Heymann et al. (2012b). In order to reduce the scattering related errors of the SCIAMACHY WFM-DOAS XCO_2 retrieval algorithm, an improved version (2.2) of this algorithm is developed, which is based on a new filtering and correction method for thin clouds.

5.1 Improved Cloud Filtering and Correction Method

The cloud filter as implemented in the WFMDv2.1 XCO_2 algorithm is based on two approaches: (i) A filtering method based on sub-pixel information of SCIAMACHY's polarisation measurement device (PMD) 1 and (ii) a threshold technique for the ratio of the retrieved to the reference O_2 column. Both approaches are described in detail in Sec. 3.5.

For the new version of the SCIAMACHY WFM-DOAS XCO_2 algorithm, version 2.2, these filtering approaches are extended by (i) a threshold technique based on the radiance from the saturated water vapour absorption band at 1.4 µm, (ii) by using stricter thresholds for the ratio of the retrieved O_2 column to the reference column and (iii) a restriction to surface elevations of less than 4 km, which is done due to LUT limitations. In addition, a correction method of XCO_2 based on the statistics of the O_2 column ratio is applied. Overall, the new filtering approach identifies about 25% more observations as contaminated with clouds (from a total amount of about $5.65 \cdot 10^6$ cloud-free ground pixels for WFMDv2.1 for the years 2003 - 2009 to about $4.24 \cdot 10^6$ for WFMDv2.2).

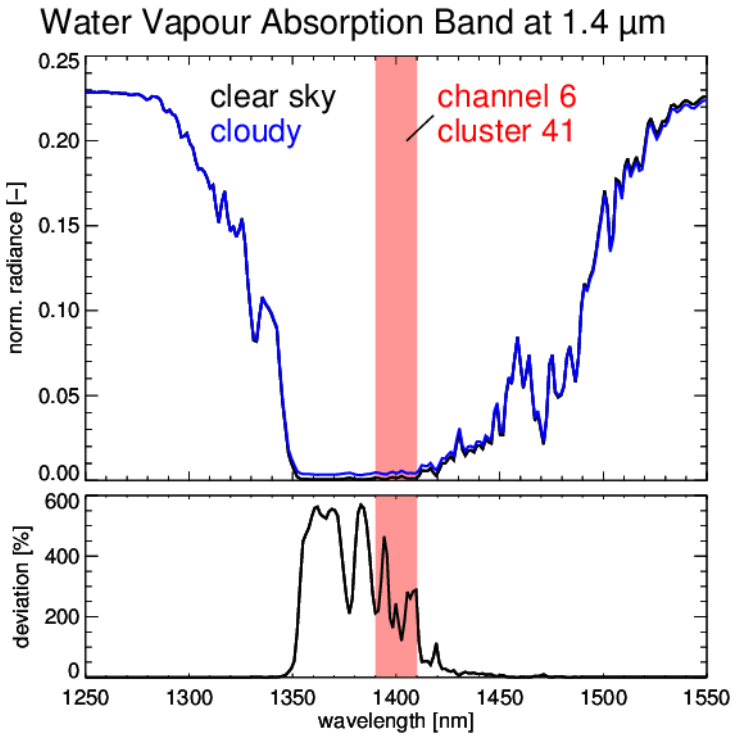

Figure 5.1: Radiances from the water vapour absorption band at 1.4 µm in SCIAMACHY resolution. Comparison between simulated clear sky (black) and cloudy sky (blue) radiances. The highlighted channel 6 cluster 41 (red) of SCIAMACHY has the same integration time as the region used for the retrievals of the O_2 and CO_2 columns.

5.1.1 Use of the Saturated Water Vapour Absorption Band at 1.4 µm

In this section, the threshold technique based on the saturated water vapour absorption band at 1.4 µm (shown in Fig. 5.1) is described. Gao et al. (1993) showed that the saturated water vapour band is sensitive to high thin cirrus clouds and can be used for cirrus cloud detection. This is because in the clear-sky case the amount of radiation measured from space in nadir mode is very small as essentially all photons are absorbed by tropospheric water vapour as shown in Fig. 5.2. When a cirrus cloud located above almost all of the atmospheric water vapour is present, a significant amount of radiation can be backscattered and measured. Our implementation of this detection method is as follows:

Sun-normalised radiance ("intensity") spectrally averaged between 1.395 – 1.41 µm measured by 20 detector pixel of SCIAMACHY channel 6 is used as shown in Fig. 5.1. The intensity is spectrally averaged to reduce the measurement error to about 0.1 %.

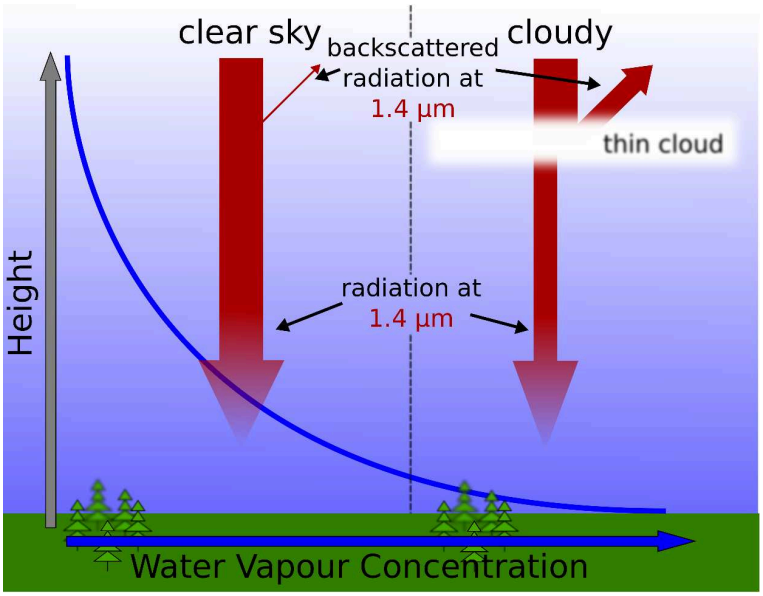

Figure 5.2: Basic principle of the cloud filter, which is based on the radiances from the water vapour absorption band at 1.4 µm (red). The decrease of the water vapour concentration with increasing height is shown in blue. The incoming solar radiation at 1.4 µm is mainly absorbed near the surface. In the clear sky case only a small amount of radiation is backscattered and measured. If a cloud is located above nearly all of the atmospheric water vapour, a large amount of radiation will be backscattered and measured. The difference in measured radiation between the clear sky and cloudy case is used for the cloud filtering.

Within this interval, the integration time of the detector is the same as in the O_2 and CO_2 fit windows used by WFM-DOAS. If the measured intensity (I_{meas}) of a ground pixel is 3-times larger than a reference intensity (I_0, corresponding to the clear sky case), the ground pixel will be flagged as cloudy. The left panel of Fig. 5.3 shows the deviation of the measured intensity from a reference intensity for SCIAMACHY WFM-DOAS v2.1. The cloud filtering threshold is shown in the right panel (the deviation has to be larger than $P_{H_2O} = 2.0$, shown by the red line), which represents a compromise between cloud filtering and the loss of too many data. Figure 5.4 shows the used reference intensity as a function of the water vapour vertical column amount (H_2O^{VCA}) and the number of occurrences for WFMDv2.1 between 2003 and 2009. To ensure that we only use cloud-free measurements for the statistical assessment of the reference intensity, we have averaged the 40 % lowest intensities within each H_2O^{VCA} interval. As can be seen, the reference intensity is nearly constant if the H_2O^{VCA} is larger than 1 g cm^{-2}. With decreasing H_2O^{VCA}, the reference intensity increases and

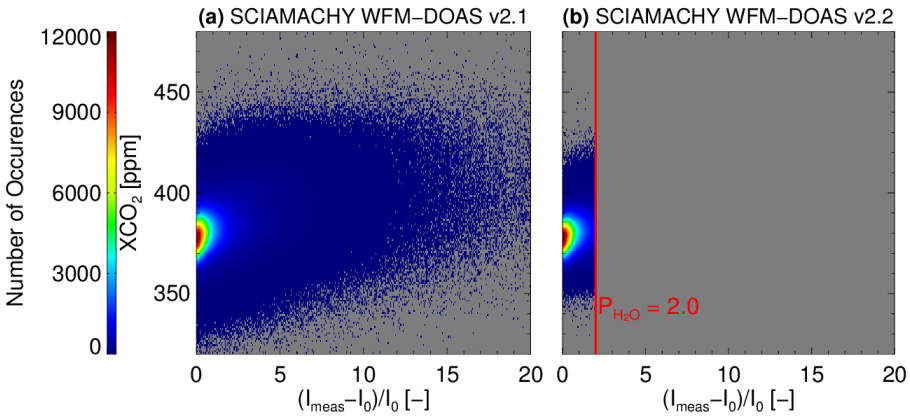

Figure 5.3: Deviations between measured intensity spectrally averaged between 1.395 – 1.41 µm (I_{meas}) and the reference intensities (I_0) for SCIAMACHY WFM-DOAS using all data of the years 2003 – 2009. **(a)** A 2-D-histogram of WFMDv2.1 XCO_2 as a function of the deviation between I_{meas} and I_0. **(b)** as **(a)** but for WFMDv2.2. The red line indicates the cloud filtering threshold ($P_{H_2O} = 2.0$).

its standard deviation as well. However, only a small fraction of the retrieved (H_2O^{VCA} is lower than 1 g cm^{-2} and the relaxed filtering threshold prevents from flagging too many clear-sky data as cloudy. The distribution of the WFMDv2.1 data shows a maximum for H_2O^{VCA} between 1.4 and 1.6 g cm^{-2}, which is similar to the 1.42 g cm^{-2} of the US standard atmosphere.

The H_2O^{VCA} used in this study is computed from the WFM-DOAS simultaneously retrieved water vapour column in the CO_2 fit window, which is given in the Level 2 (L2) data product of WFMDv2.1. Figure 5.5 shows a comparison with water vapour vertical column amounts obtained from ECMWF. A global offset (d) of −0.31 g cm^{-2}, a standard deviation of the difference of the data sets (s) of 0.53 g cm^{-2} and a correlation coefficient of 0.89 shows reasonable agreements between the two data sets. This indicates that reasonable cloud-free H_2O columns can be retrieved from the CO_2 fit window of WFM-DOAS at 1.6 µm and can be used for the filtering approach.

A more quantitative estimation of the sensitivity of this filtering method has been performed by using radiative transfer simulations. Figure 5.6 shows deviations of simulated intensities to simulated clear-sky intensities for various cloud scenarios with different water vapour vertical column amounts. The scenario of the radiative transfer simulations has been defined as follows: Only direct nadir conditions (viewing zenith angle of 0°) are considered. In order to simulate cirrus clouds, an ice cloud with fractal particles based on a tetrahedron with an edge length of 50 µm, with a

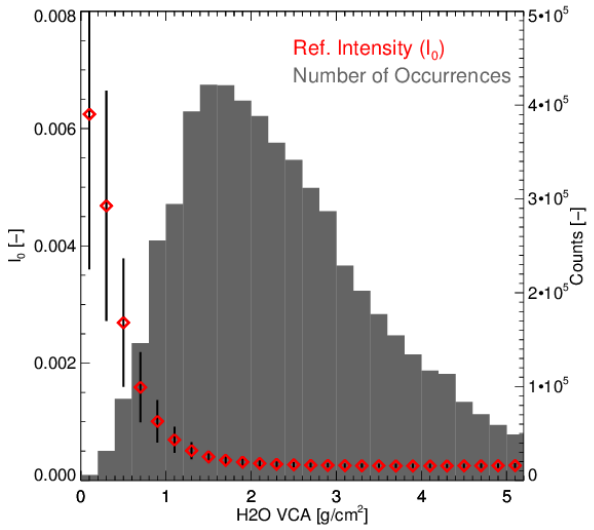

Figure 5.4: Analysis of 1.4 µm (1,395 nm - 1,410 nm) radiances as measured by SCIAMACHY for the years 2003 - 2009. The red diamonds show the "Reference Intensity" (I_0) as a function of the water vapour vertical column amount (H_2O VCA). The "Reference Intensity" is defined as the mean of the 40% lowest values of the (sun-normalised) radiances (corresponding to scenes with no clouds or very small effective cloud cover). The black vertical lines are the corresponding standard deviations. The grey histogram shows the number of occurrences as a function of the water vapour vertical column amount.

cloud top height (CTH) of 10 km and a geometrical thickness of 0.5 km is used (same cloud scenario as used in Sec. 3.5). The used aerosol profile (default aerosol profile) is based on the aerosol scenario described in Sec. 3.5. For Fig. 5.6 an albedo of 0.1 and a solar zenith angle (SZA) of 40° has been used. The intersections with the filtering threshold $P_{H_2O} = 2.0$ represent the minimum detectable cloud optical depth (COD; note that homogeneous cloud cover is assumed). For increasing water vapour vertical column amounts the minimum detectable COD decreases and the sensitivity increases slightly for column amounts larger than 1 g cm^{-2}. The filtering approach is insensitive to clouds if only a very small amount of water vapour is present in the atmospheric column.

Table 5.1 summarises the results of all simulation scenarios. For the case of water vapour vertical column amounts being larger than 1.14 g cm^{-2}, the filter becomes insensitive to SZA, CTH (assuming CTH > 4 km) and albedo. For column amounts below 1.14 g cm^{-2} the sensitivity decreases and the filter is more dependent on geometry and surface albedo. The filter is insensitive for low thin clouds (CTH < 4 km). In

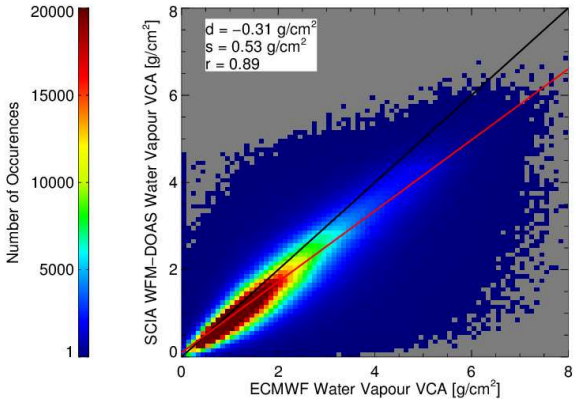

Figure 5.5: Comparison of seven years (2003 – 2009) of SCIAMACHY WFM-DOAS and ECMWF water vapour vertical column amount (VCA). The SCIAMACHY WFM-DOAS water vapour VCA is computed from the water vapour column retrieved in the CO_2 fitting window (1,558 – 1,594 nm) as a by-product of the WFM-DOAS CO_2 column retrieval. The red line shows a linear fit. Also shown in the top left inlet: The mean difference to ECMWF water vapour VCA (d), the standard deviation of the differences (s) and the correlation coefficient (r).

this case, the absorption band becomes already saturated above the cloud if enough water vapour is in the atmospheric column. This can also effect the sensitivity for high clouds but only for large H_2O^{VCA}.

The saturated water vapour absorption band based cloud filter is sensitive to thin (COD > 0.05) and high (CTH > 4 km) clouds if the observed atmospheric column contains "enough" water vapour (H_2O^{VCA} > 1.14 g cm^{-2}). The WFM-DOAS XCO_2 data set suffers from thin and high clouds in the tropics (H_2O^{VCA} typically larger than 4 g cm^{-2}, Noël et al., 2005) especially in the Southern Hemisphere, as shown by Heymann et al. (2012a) and in Sec. 4. For this reason, this filter approach is an appropriate extension to the existing cloud filtering criteria.

5.1.2 Use of O_2 Column Ratios

In combination with the cloud filter based on the radiances from the saturated water vapour absorption band at 1.4 µm, it has also been investigated to what extent a more restrictive O_2 column ratio threshold can improve the quality of the XCO_2 data product. As described in Sec. 3.4 and Sec. 3.5 for WFMDv2.1 ground pixels with deviations of the retrieved O_2 column to the reference O_2 column ("O_2-ratio") smaller than 0.9 are identified and flagged as cloudy. Here, the reference O_2 column (O_2^{ref})

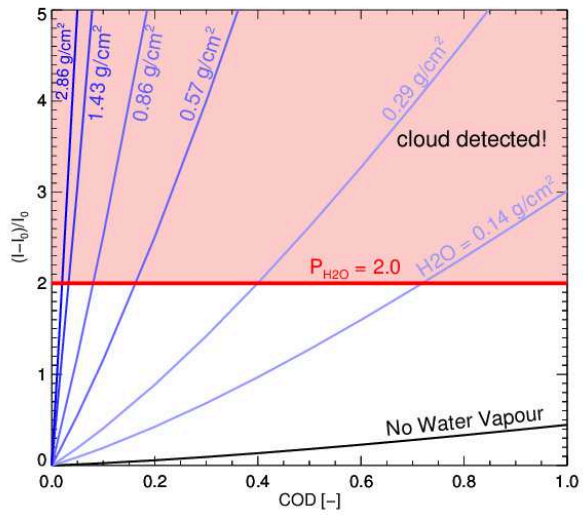

Figure 5.6: The cloud detection threshold (red horizontal line) based on strong water vapour absorption lines covering the spectral region 1395 – 1410 nm compared to results obtained from radiative transfer simulations. Deviations of simulated intensities (I) for various cloud scenarios to the reference intensities (I_0) simulated without cloud are shown as a function of cloud optical depth (COD) and different water vapour column amounts (H_2O [g/cm^2]) . The simulations are valid for a solar zenith angle of 40°, a surface albedo of 0.1, the default aerosol scenario, a cloud top height of 10 km and a cloud geometrical thickness of 0.5 km. The red line indicates the cloud detection threshold $P_{H2O} = 2.0$.

is determined from the US standard atmosphere O_2 column by accounting for the surface elevation variations and using the barometric formula in order to obtain the same O_2-ratio as used by Schneising et al. (2011).

A geometrical viewing geometry correction has been implemented for the O_2 and CO_2 column in WFM-DOAS in order to correct for a scan-angle dependent air-mass factor (Buchwitz and Burrows, 2004). For this reason, the O_2 vertical column ratio should be independent of the viewing geometry. However, it was found that the O_2-ratio exhibits a scan-angle-dependent bias. In order to improve the geometrical correction, this bias was corrected using an empirical correction. A quadratic function depending on the (signed) viewing zenith angle (VZA) (as defined in Sec. 3.6) was fitted to the O_2-ratio and used for the correction:

$$(O_2^{ret}/O_2^{ref})^{cor} = O_2^{ret}/O_2^{ref} + A_2 \cdot (VZA - A_3)^2. \quad (5.1)$$

Minimum detectable COD											
SZA [°]	ALB [–]	CTH [km]	Water vapour vertical column amount [g cm^{-2}]								
			0.00	0.14	0.29	0.57	0.86	1.14	1.43	2.86	4.29	7.15
20	0.1	10	4.76	0.98	0.58	0.25	0.13	0.08	0.05	0.03	0.03	0.03
40	0.1	10	3.68	0.72	0.40	0.16	0.08	0.05	0.03	0.02	0.02	0.02
60	0.1	10	2.40	0.34	0.16	0.06	0.03	0.02	0.01	0.01	0.01	0.01
40	0.3	10	23.74	2.04	1.04	0.41	0.19	0.10	0.06	0.02	0.02	0.02
40	0.6	10	∞	4.76	2.08	0.74	0.33	0.16	0.09	0.02	0.02	0.02
40	0.1	16	3.68	0.70	0.39	0.15	0.07	0.04	0.03	0.02	0.02	0.01
40	0.1	13	3.68	0.71	0.39	0.15	0.08	0.04	0.03	0.02	0.02	0.02
40	0.1	7	3.68	0.81	0.48	0.21	0.11	0.07	0.05	0.04	0.04	0.05
40	0.1	4	3.68	1.17	0.80	0.44	0.27	0.19	0.16	0.19	0.31	0.73

Table 5.1: Minimum detectable cloud optical depth (COD) for the cloud detection algorithm based on a threshold method for the radiance of the saturated water vapour absorption band at 1.4 µm for various simulation scenarios as defined by solar zenith angle (SZA), surface albedo (ALB), cloud top height (CTH) and water vapour vertical column amount. The default aerosol scenario and a cloud geometrical thickness of 0.5 km have been used for all scenarios. "∞" means that even clouds with large COD are not detected.

Here, O_2^{ret} corresponds to the retrieved and O_2^{ref} to the reference O_2 column. A_2 is $3.26 \cdot 10^{-5} \frac{1}{(°)^2}$ and A_3 is $-12.3°$. These values are adapted from the fit shown in the top left panel of Fig. 5.7. This figure shows the scan-angle dependency before the scan-angle-bias correction of the O_2-ratio of WFMDv2.1 in the top left panel and after the scan-angle-bias correction for WFMDv2.2 in the bottom left panel.

The scan-angle-bias corrected O_2-ratio is used for cloud filtering in the following way: If the O_2-ratio of a ground pixel exceeds 1.1 or is smaller than 0.95, the ground pixel is flagged as cloudy. O_2-ratios smaller than 1 indicate a light path shortening (e.g., due to cloud shielding) as described in Sec. 3.4, whereas O_2-ratios larger than 1 indicate a light path lengthening (e.g., due to multiple scattering). For this reason, the lower threshold of 0.9 of WFMDv2.1 to 0.95 is increased and the upper threshold of 1.1 is added.

Various simulations to study the relation of XCO_2 and the O_2-ratio in the presence of thin clouds and aerosols have been performed. A strong and nearly linear dependency of XCO_2 on the O_2-ratio for simulation scenarios (same default scenario as used in Sec. 3.6) with different SZA, surface albedos and COD are found. The reason for this dependency are different light paths in the O_2 and CO_2 spectral regions due to scattering by aerosols and thin clouds. Therefore, we have investigated if an O_2

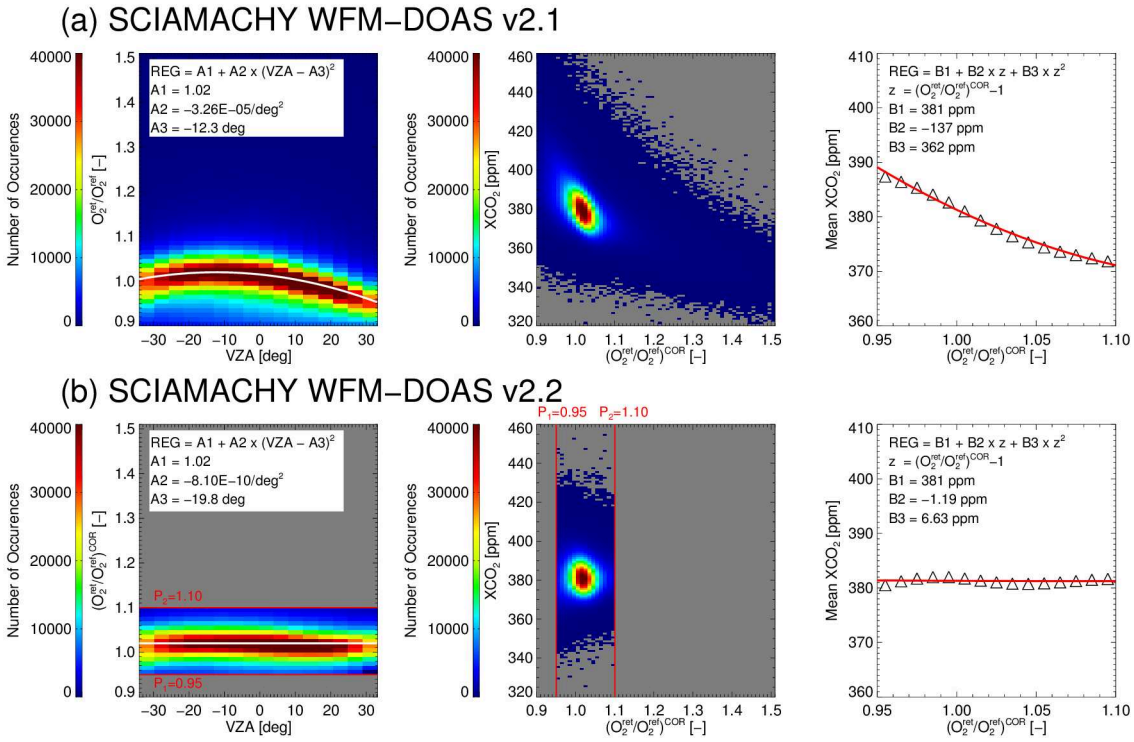

Figure 5.7: Comparison of the O_2 column ratio (O_2^{ret}/O_2^{ref}) for SCIAMACHY WFM-DOAS version 2.1 (a) and 2.2 (b) using all data of the years 2003 - 2009. (a) The left panel shows a 2D-histogram of the O_2-ratio as a function of the viewing zenith angle (VZA). The white curve is a quadratic fit. The middle panel shows a 2D-histogram of XCO_2 as a function of the O_2-ratio. The right panel shows XCO_2 averaged over scan-angle-bias corrected O_2-ratio intervals. The red curve is a polynomial fit. (b) as (a) but for WFM-DOAS version 2.2. The red lines in the left and middle panel indicate the new O_2-ratio thresholds ($P_1 = 0.95$ and $P_2 = 1.1$).

column obtained from ECMWF (European Centre for Medium-Range Weather Forecasts) surface pressure and used for the normalisation of the CO_2 column improves the quality of the XCO_2 data product. However, we find large regional patterns, a much larger intra-monthly scatter, larger seasonal cycle amplitudes and significant lower yearly increases over the Northern and Southern Hemisphere. Overall we find, that using ECMWF O_2 columns for the normalisation of the retrieved CO_2 columns reduces the quality of the SCIAMACHY WFM-DOAS XCO_2 data product. Therefore, we keep on using the retrieved O_2 column for the normalisation of the CO_2 column and correct for the bias between XCO_2 and the O_2-ratio using a statistical method. It is assumed that other features responsible for the O_2-ratio dependent bias in XCO_2 than scattering by aerosols and thin clouds can be neglected. A polynomial fitted to averaged XCO_2 and O_2-ratios is used:

$$XCO_2^c = XCO_2 + B_1 + B_2 \cdot z + B_3 \cdot z^2 \tag{5.2}$$

$$z = (O_2^{fit}/O_2^{ref} - 1)$$

Here B_1 is -0.8 ppm and accounts for a global offset. B_2 is 137 ppm and B_3 is -362 ppm. The fit parameters shown in Fig. 5.7 top-right are used for this correction. The mid- and right-bottom panels in this figure show the resulting dependency of XCO_2 on the O_2-ratio after applying the improved filter method. As can be seen, the stricter O_2-ratio thresholds remove unrealistic high and low values of XCO_2 and the remaining O_2-ratio dependent bias in XCO_2 is very small.

5.2 Single Measurement Precision

In Sec. 3.6.2 the monthly regional-scale scatter of the SCIAMACHY WFMDv2.1 XCO_2 data product of about 7.42±1.29 ppm is determined. The same method has been used to determine this value for the new version 2.2 data product.

The scatter is derived as follows: The standard deviation of all XCO_2 measurements within a radius of 350 km around several locations for each month is computed. The locations used for this assessment are shown in Fig. 3.8 and their latitudes and longitudes are listed in Tab. 5.2. The mean of the monthly standard deviations is derived for all locations. The overall value of the scatter is the mean of the scatter of all locations. This value is not only determined by instrumental and retrieval noise. Atmospheric XCO_2 variability and systematic (but varying) errors can also affect this value (note that the seasonal cycle is filtered out by using the standard deviations of the monthly

Monthly regional-scale scatter of the data								
ID	Location	Country	Lat [°]	Lon [°]	WFMDv2.1		WFMDv2.2	
					abs [ppm]	rel [%]	abs [ppm]	rel [%]
1	Lamont	USA	36.6	−97.5	7.56	1.99	4.01	1.05
2	Park Falls	USA	46.0	−90.3	7.65	2.01	5.29	1.39
3	Brasilia	Brazil	−15.8	−47.9	8.26	2.16	4.52	1.19
4	Orleans	France	48.0	2.1	6.28	1.64	4.48	1.17
5	Garmisch	Germany	47.5	11.1	8.09	2.14	5.56	1.46
6	Bialystok	Poland	53.2	23.0	6.09	1.59	4.61	1.21
7	Tazirbu	Libya	25.7	21.4	4.95	1.30	3.48	0.91
8	Lubumbashi	Congo	−11.7	27.5	9.09	2.39	4.68	1.23
9	Khromtau	Kazakhstan	50.3	58.5	9.23	2.43	4.68	1.23
10	Darwin	Australia	−12.4	130.9	7.20	1.88	3.80	1.00
11	Wollongong	Australia	−34.4	150.9	7.17	1.89	4.52	1.19
MEAN					7.42 ± 1.29	1.95 ± 0.34	4.51 ± 0.60	1.18 ± 0.16

Table 5.2: Scatter of the WFMDv2.1 and v2.2 XCO_2 data products at several locations and overall ("MEAN").

data). However, the computed monthly regional-scale scatter of the data can be regarded as an upper limit of the single measurement precision.

The standard deviations of WFMDv2.1 and WFMDv2.2 XCO_2 are listed in Tab. 5.2. As can be seen, the standard deviation is smaller for version 2.2. The monthly regional-scale scatter is reduced to 4.51 ± 0.60 ppm for WFMDv2.2 compared to 7.42 ± 1.29 ppm for WFMDv2.1.

In addition, the single measurement precision is estimated using the same approach as used in the publication of Schneising et al. (2011). They estimated the precision by averaging daily standard deviations of the retrieved XCO_2 for 8 locations distributed around the globe. This estimation shows a reduction of the single measurement precision from 5.4 ppm (1.4%) of WFMDv2.1 to 3.8 ppm (1%) of WFMDv2.2.

5.3 Validation with TCCON FTS Measurements

In order to investigate whether the filtering and correction method improves the quality of the SCIAMACHY XCO_2 data product, the new WFMDv2.2 data set has been compared with the independent TCCON FTS measurements and the results are intercompared with validation results for WFMDv2.1. In this section, the result of this inter-comparison are discussed.

5.3.1 TCCON

The independent measurements from the ground-based Fourier transform spectrometers of the Total Carbon Column Observing Network are used for the validation of the SCIAMACHY WFMDv2.2 XCO_2 data product. TCCON is a global network of ground-based FTS instruments and provides measurements of CO_2 and other greenhouse gases (Wunch et al., 2011). The FTS measurements are the most important validation source for measurements from satellite instruments like SCIAMACHY and GOSAT and future satellite missions like OCO-2 (Crisp et al., 2004; Bösch et al., 2011) and CarbonSat (Bovensmann et al., 2010). A stable and robust commercial high-resolution FTS, the Bruker IFS 125/HR, is used as standard instrument and common data processing and analysis software is utilised to determine XCO_2 with a high accuracy of approximately 0.2% (Wunch et al., 2011).

The FTS data are obtained from the TCCON website (http://www.tccon.caltech.edu). Here, monthly means are used.

5.3.2 Validation Method

The validation of WFMDv2.2 XCO_2 is performed in the same way as described in the publication of Schneising et al. (2012) for WFMDv2.1. This implies that monthly means for the time period 2003 – 2009 computed using a sufficiently large number of measurements within a radius of 500 km around the analysed TCCON sites (Bialystok, Bremen, Garmisch, Park Falls, Lamont, Darwin and Wollongong) are used. The locations of the TCCON sites are shown in Fig. 3.8 and the corresponding latitudes and longitudes are listed in Tab. 5.3.

From the monthly time series of the satellite and FTS data statistical quantities are determined for every FTS site: The regional bias (d) (mean difference to FTS measurements), the mean standard deviation of the difference (s) and the linear correlation coefficient (r) with the FTS measurements. From these values the offset, the monthly regional-scale precision (the mean standard deviation of the difference to FTS), the mean correlation and the regional-scale relative accuracy (the standard deviation of the station-to-station biases) are determined.

The comparison between retrieved CO_2 columns from measurements of different instruments is not trivial because of the different averaging kernels and a-priori information. In order to ensure that the differences between the measurements are not from the differences of the averaging kernels and from the differences of the a-priori information, Rodgers (2000) recommend the adjustment of the measurements by using a common a-priori profile and accounting for the averaging kernels. The WFMD averaging kernel, which shows the sensitivity of the measurement to the atmospheric

layers, and the a-priori CO_2 profile are shown in Fig. 3.1.

For the total column of CO_2 ($\hat{c}$), the adjustment (c_{adj}) is the following(Schneising et al., 2011):

$$c_{\mathrm{adj}} = \hat{c} + \frac{1}{p_0} \sum_{\mathrm{l}} (1 - A^{\mathrm{l}})(x^{\mathrm{l}}_{\mathrm{mod}} - x^{\mathrm{l}}_{\mathrm{a}}) \cdot \Delta p^{\mathrm{l}} \tag{5.3}$$

Δp^{l} is the pressure difference between the upper and lower boundary of the l-th layer and p_0 is the surface pressure. A^{l} is the value of the l-th layer of the averaging kernel. $x^{\mathrm{l}}_{\mathrm{mod}}$ is the l-th layer of the common a-priori CO_2 profile and $x^{\mathrm{l}}_{\mathrm{a}}$ is the l-th layer of the a-priori profile.

In order to compare the SCIAMACHY WFMD XCO_2 data product with CarbonTracker XCO_2 and the TCCON FTS measurements, shown in Sec. 5, the WFMD XCO_2 data are adjusted to use CarbonTracker XCO_2 as the common a-priori. For the FTS measurements the CO_2 averaging kernels are often close to unity and the used a-priori profiles only marginally differ from the corresponding CarbonTracker profiles. For this reason, the difference between the measured FTS XCO_2 values and the adjusted ones are only small. Reuter et al. (2011) found that adjusting the FTS measurements as described above results in only small modifications of about 0.1 ppm. This is small compared to SCIAMACHY's precision. Therefore and for the reason of simplification, the FTS measurements are not adjusted.

5.3.3 Validation Results

The results of the comparison of the WFMDv2.1 and WFMDv2.2 XCO_2 data product with the TCCON FTS measurements are shown in Fig. 5.8 and summarised in Tab. 5.3.

The comparison of WFMDv2.1 XCO_2 with the FTS measurements for Darwin, Australia, shows a large monthly scatter of the data (7.5 ppm, shown in Tab. 5.2) and large differences to the FTS (3.9 ppm). This is improved for the new WFMDv2.2 XCO_2 data product. The scatter is reduced to 3.8 ppm. The large deviation to the FTS is improved by nearly a factor of 2 (from 3.9 ppm to 2.0 ppm). The improvement is also shown by a higher correlation (0.75) between the satellite and the FTS data.

The results of the comparison for a location on the Northern Hemisphere, Lamont USA, shows also a reduced scatter (from 1.75 ppm to 1.29 ppm) and an improved correlation (from 0.73 to 0.85).

Overall, the comparison of WFMDv2.2 XCO_2 with FTS shows much better agreement than for WFMDv2.1. The monthly regional-scale precision has been improved from 2.1 ppm for WFMDv2.1 to 1.6 ppm for WFMDv2.2. The regional-scale relative accuracy has been improved from 1.1 ppm to 0.8 ppm and the mean correlation has

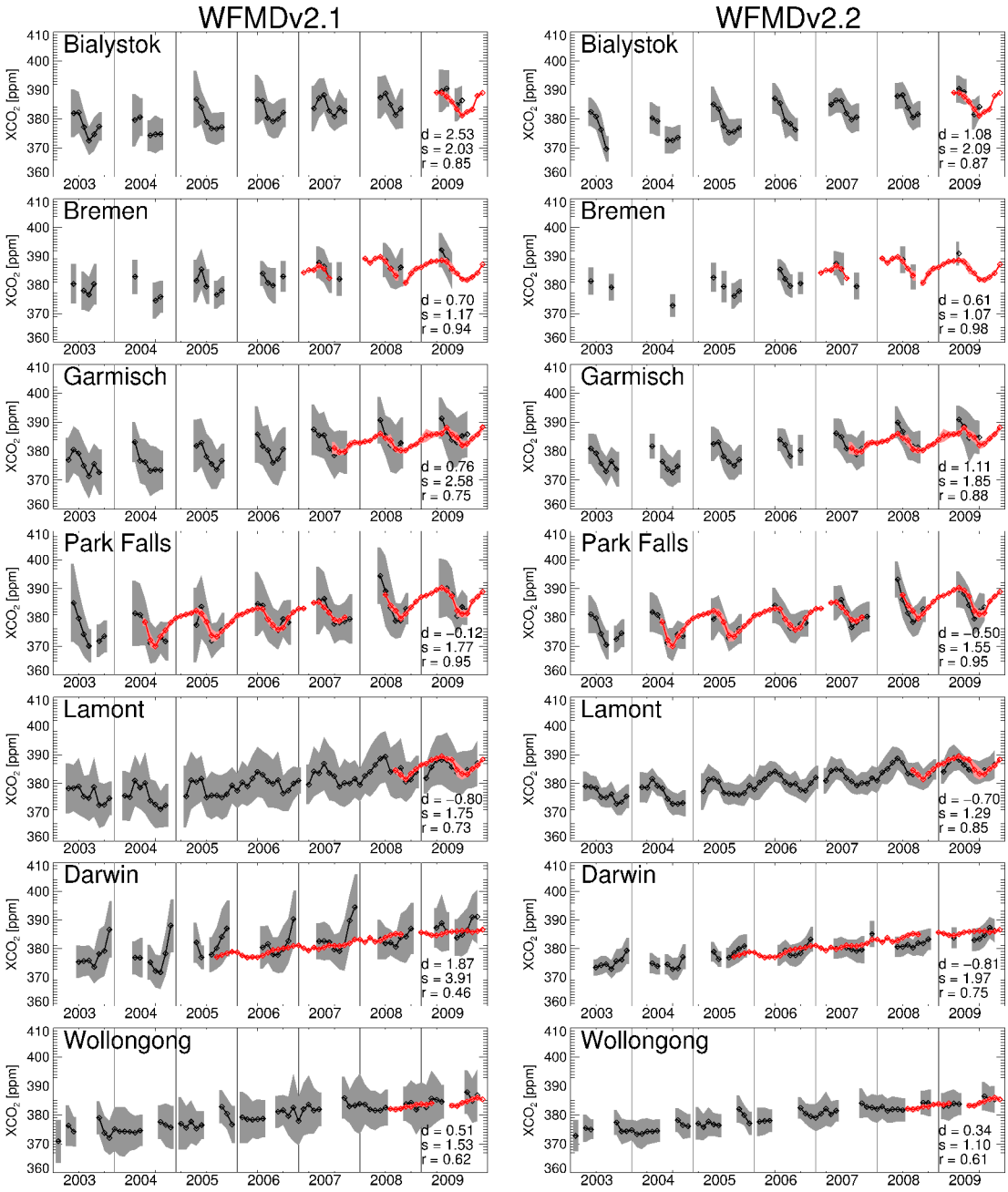

Figure 5.8: Comparison of monthly averaged SCIAMACHY WFM-DOAS version 2.1 (left) and 2.2 (right) XCO_2 (black) with Fourier Transform Spectroscopy (FTS) measurements (red) at various TCCON sites for the years 2003 - 2009. The monthly standard deviations are represented by the shaded areas (grey: WFMD; light red: TCCON). In addition, the mean difference (d), the standard deviation of the difference (s) and the correlation (r) between the satellite and ground based data are shown (see also Tab. 5.3).

TCCON Site	Lat [°]	Lon [°]	WFMDv2.1				WFMDv2.2			
			n [–]	d [ppm]	s [ppm]	r [–]	n [–]	d [ppm]	s [ppm]	r [–]
Bialystok	53.2	23.0	4	2.53	2.03	0.85	4	1.08	2.09	0.87
Bremen	53.1	8.8	9	0.70	1.17	0.94	5	0.61	1.07	0.98
Garmisch	47.5	11.1	14	0.76	2.58	0.75	13	1.11	1.85	0.88
Park Falls	46.0	−90.3	35	−0.12	1.77	0.95	35	−0.50	1.55	0.95
Lamont	36.6	−97.5	16	−0.80	1.75	0.73	16	−0.70	1.29	0.85
Darwin	−12.4	130.9	31	1.87	3.91	0.46	28	−0.81	1.97	0.75
Wollongong	−34.4	150.9	9	0.51	1.53	0.62	7	0.34	1.10	0.61
MEAN			–	0.78 ± 1.13	2.11	0.76	–	0.16 ± 0.83	1.56	0.84

Table 5.3: Results of the comparison of WFMDv2.1 and v2.2 XCO_2 data with ground based FTS measurements at various TCCON sites. The comparison is based on monthly data. Shown are the number of months used for the comparison (n), the mean difference to FTS (d), the standard deviation of the difference (s) and the correlation (r). In addition, the following quantities are given in the bottom row ("MEAN"): The averaged mean difference (global offset), the standard deviation of the mean differences (relative regional-scale accuracy), the mean standard deviation of the differences (monthly regional-scale precision) and the mean correlation.

been improved from 0.76 to 0.84.

These results show that the improved cloud filtering and correction method for WFMDv2.2 significantly improves the quality of the XCO_2 data product. This is also shown in Tab. 5.4, which is a summary of the validation results.

5.4 Comparison with CarbonTracker

In addition to the comparison with the limited number of TCCON sites, a comparison of WFMDv2.2 XCO_2 with global model results using NOAA's CarbonTracker has also been performed.

Figure 5.9 shows three-monthly averaged (April to June and July to September) global maps of WFMDv2.2 and CarbonTracker XCO_2 for the years 2003 and 2009. The data are gridded on a $0.5° \times 0.5°$ latitude/longitude grid. Furthermore, the data has been smoothed by using a 2D-Hann window with a width of $10° \times 10°$ because some grid boxes have not sufficient data to remove the statistical error. For a comparison, Fig. 5.10 shows global maps for WFMDv2.1 and CarbonTracker. The SCIAMACHY WFMDv2.2 XCO_2 maps show that also with the much stricter cloud filtering and correction method good coverage of most land surfaces is achieved. There are however some gaps, e.g., Sahara and Himalayas, similar as for WFMDv2.1. In comparison

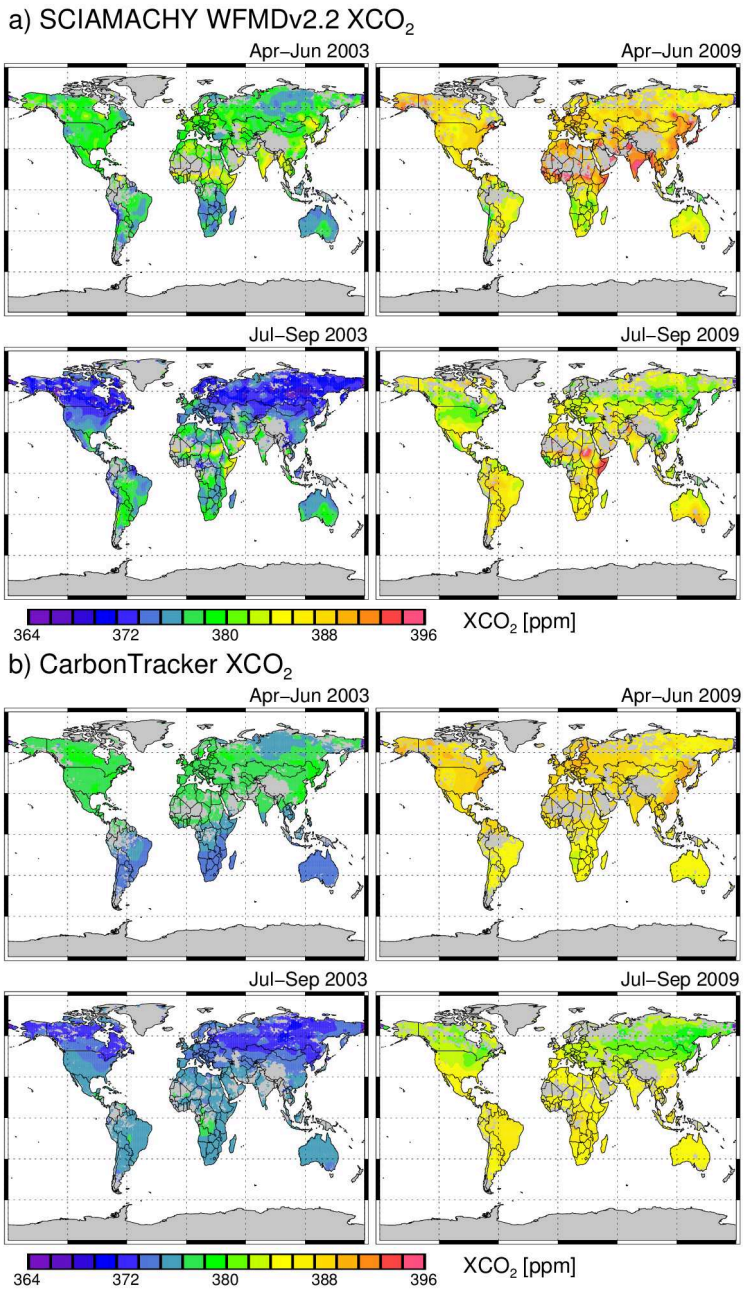

Figure 5.9: Comparison between global SCIAMACHY WFMDv2.2 and CarbonTracker XCO_2. a) Global SCIAMACHY WFMDv2.2 XCO_2 maps for the time periods April to June and July to September in 2003 and 2009. The data have been gridded on a 0.5°×0.5° latitude/longitude grid and smoothed by using a 2D-Hann window with a width of 20×20 (10°×10°). b) as a) but for CarbonTracker XCO_2 sampled as the SCIAMACHY measurements.

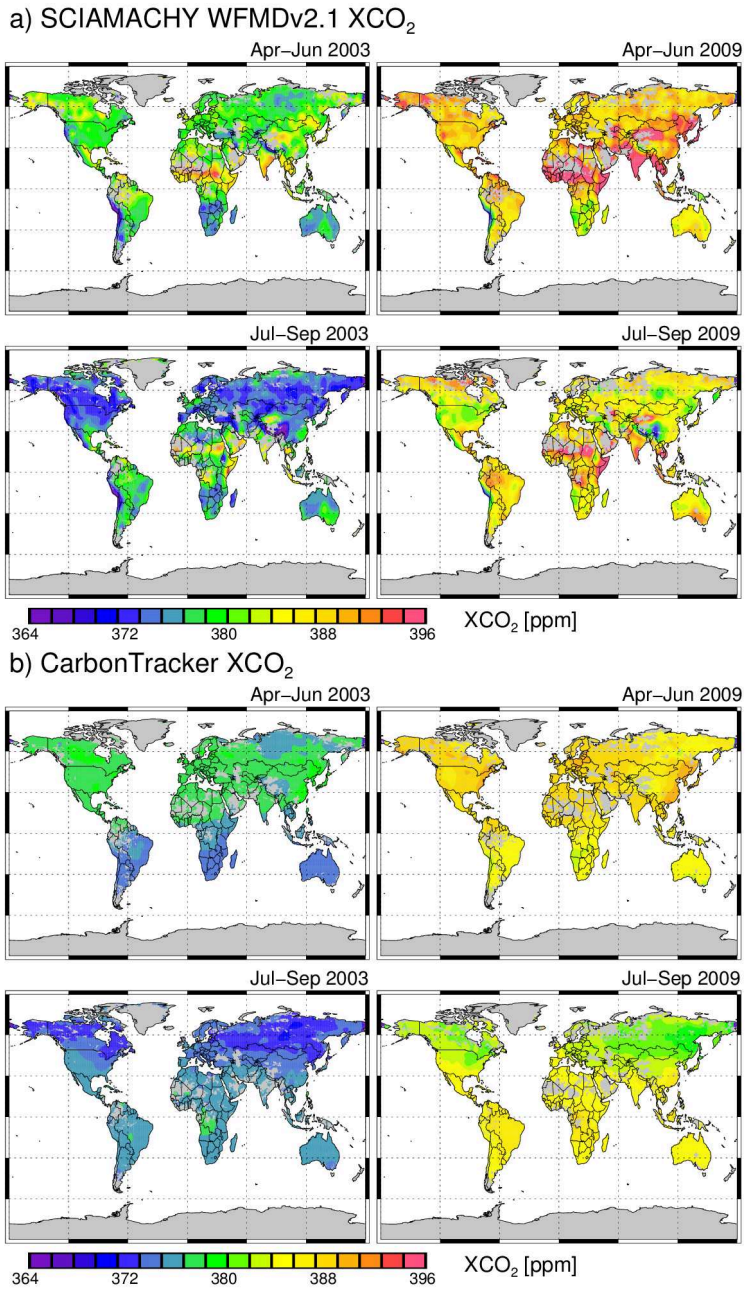

Figure 5.10: As Fig. 5.9 but for WFMDv2.1.

	WFMDv2.1 [ppm]	WFMDv2.1^C [ppm]	WFMDv2.2 [ppm]
Global Bias	1.07♣	0.78	0.16
Intra-monthly standard deviation	9.04	7.42	4.51
Estimated monthly regional-scale* precision	2.24♣	2.11	1.56
Estimated single measurement precision	6♠	5.4♣	3.8
Estimated monthly regional-scale* accuracy	1.15♣	1.13	0.83

Table 5.4: Summarised validation results. The validation results marked with a ♣ are from Schneising et al. (2012) and the result marked with a ♠ is from Schneising et al. (2011). The * indicates a regional scale of 500 km radius around the investigated locations. WFMDv2.1^C is the scan-angle-bias corrected SCIAMACHY XCO_2 data product. All values are given in ppm.

to WFMDv2.1, high XCO_2 values over Central Africa and India and low XCO_2 values over mountain flanks (e.g., over the Andes and over the Himalayas) are removed or corrected due to the improved cloud filtering and correction method of WFMDv2.2. The maps of the SCIAMACHY and CarbonTracker XCO_2 also show the northern hemispherical terrestrial vegetation induced carbon uptake in summer as shown by higher XCO_2 values in April – June compared to lower XCO_2 values in July – September in 2003 and 2009. In addition, the increase of the global CO_2 concentration is seen by the higher XCO_2 in 2009 compared to 2003. The WFMDv2.2 and CarbonTracker data sets show reasonable agreement. There are, however, also significant differences for WFMDv2.2, e.g., over India and the Horn of Africa, which need further investigation.

For a more quantitative investigation, WFMDv2.2 and CarbonTracker XCO_2 are compared using hemispheric monthly means between 2003 and 2009. In order to investigate if the improved cloud filtering and correction method reduces the difference to CarbonTracker, it is compared with WFM-DOAS v2.1 XCO_2. However, it has to be noted that CarbonTracker, as already mentioned in Sec. 4.3, is affected by errors of its own like, e.g., incorrect accounting for the vertical transport and the ageing of air and uncertainties in the biosphere fluxes (Basu et al., 2011).

Important parameters for the comparison are determined in the following way: The annual increase is determined by smoothing the time series with a twelve-month boxcar function and computing the mean from the derivative of the smoothed time series. The seasonal cycle amplitude is determined from a detrended time series between 2004 and 2008 by averaging the yearly difference of maximum and minimum XCO_2. The error of the increase and the amplitude is estimated by a bootstrap

method, which was introduced by Efron (1979). The idea of bootstrap is using the sample (the time series) as a "surrogate population". This population is used for a resampling with replacement in order to create a large number of new samples. The standard deviation of the increases and of the amplitudes of the samples can be utilised as an estimation for the uncertainty of the increase and amplitude, respectively.

The correlation with CarbonTracker and the standard deviation of the difference to CarbonTracker has been determined. In addition, the "detrended" correlation coefficient (r) to CarbonTracker is computed from the detrended time series of WFMDv2.1 and WFMDv2.2 and is an indicator for (phase) shifts between the time series.

Figure 5.11 shows the result of this comparison. As can be seen, the scatter is reduced from 10.2 ppm for WFMDv2.1 to 5.8 ppm for WFMDv2.2 for the Northern Hemisphere and from 9.2 ppm to 4.6 ppm for the Southern Hemisphere. The correlation with CarbonTracker is for both WFM-DOAS versions and for both hemispheres nearly the same. The standard deviation of the differences is slightly worse for the Northern Hemisphere (from 1.3 ppm to 1.5 ppm) and slightly better for the Southern Hemisphere (from 1.3 ppm to 0.9 ppm). The annual increase, the seasonal cycle amplitude and the detrended correlation of the Northern Hemisphere are not changed significantly. For the Southern Hemisphere, the annual increase of WFMDv2.2 is also not changed significantly. However, the seasonal cycle amplitude is lower for WFMDv2.2 and agrees better with CarbonTracker compared to WFMDv2.1. The phase shift of the seasonal cycle of WFMDv2.1 shown by the detrended correlation of -0.19 was significantly improved for WFMDv2.2 shown by the detrended correlation of 0.72.

Overall, the SCIAMACHY WFM-DOAS v2.2 XCO_2 data product shows much better agreements with CarbonTracker compared to WFMDv2.1.

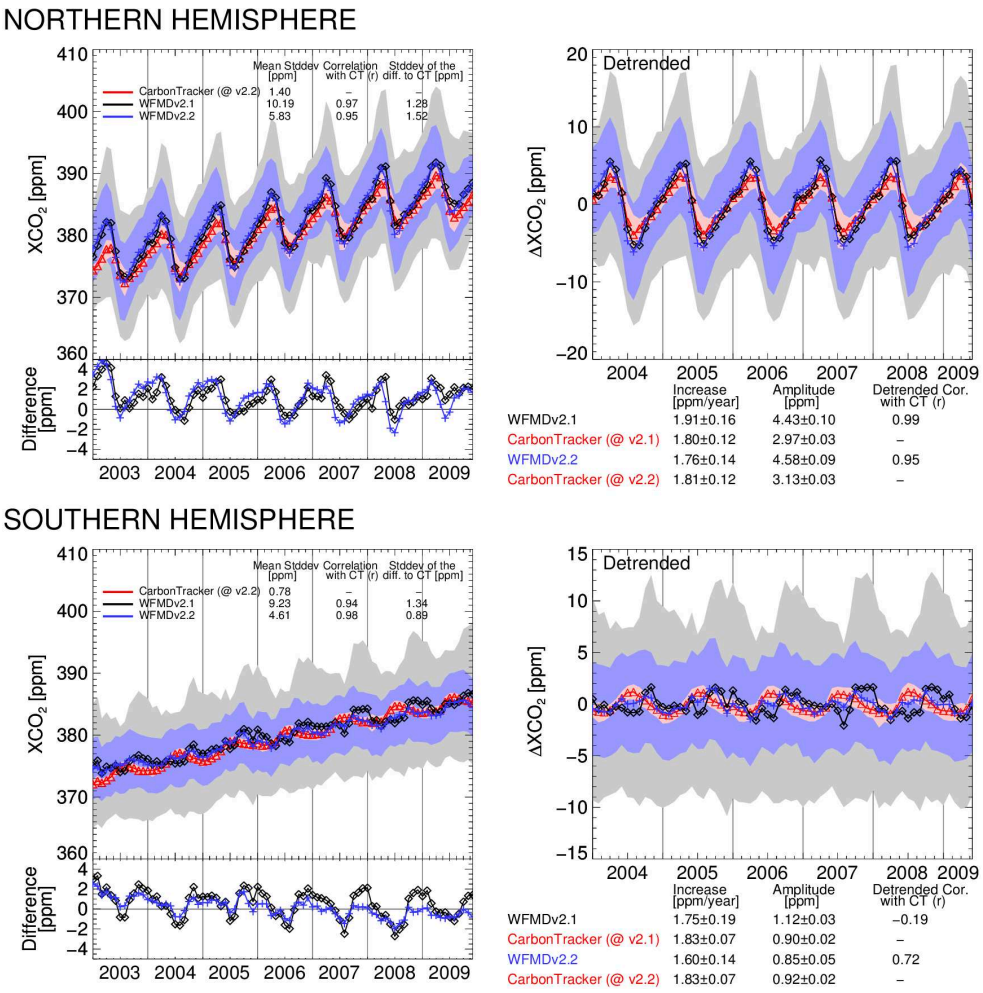

Figure 5.11: Comparison of SCIAMACHY WFM-DOAS version 2.1 (WFMDv2.1) and 2.2 (WFMDv2.2) with CarbonTracker XCO_2 for the Northern (top) and Southern (bottom) Hemisphere for the years 2003 - 2009. CarbonTracker was sampled as WFMDv2.1 (@v2.1) for the comparison with WFMDv2.1 and sampled as WFMDv2.2 (@v2.2) for the comparison with WFMDv2.2. Top: The left panel shows the time-series of monthly means of WFMDv2.1 (black), WFMDv2.2 (blue) and CarbonTracker (red) XCO_2 and the difference to CarbonTracker for the Northern Hemisphere. The shaded areas represent the monthly standard deviations of WFMDv2.1 (grey), WFMDv2.2 (light blue) and CarbonTracker (red). In addition, the averaged monthly standard deviation, the correlation with CarbonTracker and the standard deviation of the difference to CarbonTracker are shown. The right panel shows the detrended time-series. Furthermore, the annual increase, the seasonal cycle amplitude and the detrended correlation (correlation between the detrended satellite time-series and CarbonTracker) are shown. Bottom: As top panels but for the Southern Hemisphere.

6 Summary, Conclusions and Future Work

The reduction of scattering related retrieval errors is one of the most important issues in the field of XCO_2 retrievals from observations of satellite remote sensing instruments measuring in the short wave infrared spectral region. Therefore, the main objectives of the work presented in this thesis were to assess the quality of an existing satellite-based XCO_2 data set focussing on the investigation of systematic errors due to unaccounted scattering by aerosols and clouds and to generate and validate an improved XCO_2 data set. For this purpose, the existing SCIAMACHY WFM-DOAS XCO_2 data set (WFMDv2.1) has been investigated. It has been found that this data set suffers especially from cloud related errors. This was the reason why an improved version of the WFM-DOAS retrieval algorithm has been developed in the framework of this thesis and a new SCIAMACHY WFM-DOAS XCO_2 data set (WFMDv2.2) has been generated. In order to investigate if the new version of the retrieval algorithm improves the XCO_2 data product, the data set has been validated against measurements from a network of ground-based Fourier Transform Spectrometers (FTS) and has been compared with output of a state-of-the-art global CO_2 model. In the following, the results of these investigations are summarised and conclusions are given. Finally, possible future work is outlined.

6.1 Summary and conclusions

In order to understand the differences between satellite-derived and modelled XCO_2, a comparison between SCIAMACHY WFM-DOAS XCO_2 and output from NOAA's assimilation and modelling system CarbonTracker has been performed. The focus of this comparison has been to find out to what extent the observed differences between these two CO_2 data sets are influenced by systematic retrieval errors due to aerosols and unaccounted (thin) clouds. For this reason, the WFMDv2.1 SCIAMACHY XCO_2 data product of Schneising et al. (2011) has been used, which covers the years 2003 – 2009, and CarbonTracker version 2010.

During this investigation, a scan-angle-dependent bias of the WFMDv2.1 XCO_2 data product has been identified. Simulated retrievals have indicated that this error is caused by not fully accounted scattering related light path modifications. To correct for this error, an empirical correction scheme based on a parabolic function has been developed. It has been shown that this correction removes the scan-angle-dependent bias to a large extent.

It has also been investigated to what extent the SCIAMACHY minus CarbonTracker XCO_2 differences are spatially and temporally correlated with global aerosol and cloud data sets. For this purpose, a global aerosol data set generated within the European GEMS project, which is based on assimilated MODIS satellite data, has been used. For clouds, a data set derived from CALIPSO/CALIOP has been utilised.

Significant temporal correlations between the SCIAMACHY and CarbonTracker XCO_2 difference and CALIPSO/CALIOP effective cloud optical depth (eCOD) over the Southern Hemisphere have been found. Over the Northern Hemisphere the temporal correlations with eCOD were lower or non-significant (with one exception, India). Temporal correlations with aerosol optical depth (AOD) were typically lower or non-significant compared to eCOD. The spatial correlation analysis has not shown a clear picture for the Northern Hemisphere. Over the Southern Hemisphere, spatial correlations with clouds were often larger than 25%.

The correlation with thin clouds over the Southern Hemisphere corroborates the conclusion of Schneising et al. (2011) that the seasonal cycle of WFMDv2.1 XCO_2 over the Southern Hemisphere presumably suffers from unconsidered scattering due to thin clouds. This investigation has provided more quantitative evidence that the quality of the SCIAMACHY WFMD-derived XCO_2 data product benefits from algorithm improvements aiming at reducing cloud related retrieval errors.

Therefore, an improved version of the SCIAMACHY WFM-DOAS XCO_2 retrieval algorithm has been developed. This new algorithm version utilises an improved cloud filtering and correction method using the 1.4 µm water vapour absorption and the 0.76 µm O_2-A band to identify and select cloud free scenes. A new SCIAMACHY XCO_2 data set (WFMDv2.2) covering the years 2003 – 2009 has been generated by using this new version. In order to validate this data product, ground-based FTS observations from TCCON have been used, which are the validation standard for satellite XCO_2 data products.

The validation has shown a significant improvement of the new SCIAMACHY WFMDv2.2 XCO_2 data product in comparison to the previous product WFMDv2.1. For example, the large time dependent deviation from the FTS measurements at Darwin has been reduced from a standard deviation of 4 ppm to 2 ppm. The monthly regional-scale scatter of the data (defined as standard deviation of all monthly qual-

ity filtered XCO_2 retrievals within a radius of 350 km around various locations) has also been improved typically by a factor of about 1.5. Overall, the single measurement precision has been improved from 5.4 ppm for WFMDv2.1 to 3.8 ppm for WFMDv2.2, the monthly regional-scale precision has been improved from 2.1 ppm to 1.6 ppm, the regional-scale relative accuracy has been improved from 1.1 ppm to 0.8 ppm and the mean correlation has also been improved from 0.76 to 0.84.

Rayner and O'Brien (2001) found that a precision of 2.5 ppm for $8^\circ \times 10^\circ$ large regions on a monthly basis is a prerequisite for the surface flux inversion application. The WFMDv2.2 monthly regional-scale precision of 1.6 ppm (~1000 km radius) is considerably smaller than the required one. Houweling et al. (2004) showed that for SCIAMACHY a single measurement precision of 1 % (3 – 4 ppm) is needed. This has been achieved by the single measurement precision of 3.8 ppm. The accuracy requirements are more challenging because small regional biases of a few tenth of a ppm can already hamper the inversion application (e.g., Miller et al., 2007, Chevallier et al., 2007). The presented analysis has shown that a monthly relative regional-scale accuracy of 0.8 ppm has been achieved. Therefore, additional improvements concerning the accuracy of the XCO_2 data product are necessary before it can be used for the surface flux inversion application.

An investigation of the differences between the new SCIAMACHY WFMDv2.2 XCO_2 data set and CarbonTracker XCO_2 has been performed. Reduced differences in the southern hemispheric seasonal cycle of atmospheric CO_2 compared to the previous SCIAMACHY XCO_2 version (WFMDv2.1) have been found. Nevertheless, the northern hemispherical seasonal cycle amplitude is still larger compared to the model.

In summary, this thesis has contributed to a better understanding of scattering related retrieval errors. This has led to the development of a new method for reducing these errors. As a result, the quality of the SCIAMACHY XCO_2 data product has been improved and the precision and accuracy have moved closer to the demanding requirements of the CO_2 surface flux inversion application.

6.2 Future Work

The new SCIAMACHY XCO_2 data product has already been used for interesting applications such as the investigation of anthropogenic CO_2 source regions (shown in Fig. 6.1). Schneising et al. (2012b) compared XCO_2 enhancements and anthropogenic CO_2 emissions from the Emission Database for Global Atmospheric Research (EDGAR) over three major anthropogenic source regions, namely the Rhine-Ruhr metropolitan region, the East Coast of the United States and the Yangtze River Delta.

Focussing on regional variations due to anthropogenic emissions they also applied an additional correction based on a multivariate linear regression, which minimises residual systematic retrieval biases. The resulting data set is referred to WFMDv2.3. The results of this analysis showed significant XCO_2 enhancements over the source regions. The order of magnitude of these enhancements is in reasonable agreement with what is expected. Furthermore, a significant positive trend of the XCO_2 enhancements over the Yangtze River Delta has been identified, which is quantitatively consistent with the anthropogenic CO_2 emissions from EDGAR. This investigation demonstrates that anthropogenic CO_2 emissions and emission trends can be detected by using satellite observations.

In addition, the SCIAMACHY XCO_2 data product is used as part of the Ensemble Median Algorithm (EMMA) (Reuter et al., 2012b). EMMA combines the advantages of several independently developed retrieval algorithms by using a median approach and generates a new satellite based XCO_2 data set with reduced spatial and temporal bias patterns. The high precision and accuracy of EMMA are the reason why this XCO_2 data product is a promising candidate for the CO_2 surface flux inversion application.

In the future, the new version of the SCIAMACHY WFM-DOAS v2.2 retrieval algorithm will be utilised to retrieve XCO_2 from the complete period of the ENVISAT mission, which started in March 2002 and abruptly ended at the 8 April 2012. This is possible because a new version of the SCIAMACHY level 1 product has been generated covering the entire time period.

An extended XCO_2 data set will allow to use more TCCON stations for the validation because some TCCON sites became operational in the last few years of the ENVISAT mission. However, important regions are not covered like tropical rainforests and deserts. Therefore, complementary validation resources for satellite observations like NOAA's AirCore system, which is currently under development, can additionally be utilised in the future (Karion et al., 2010; Reuter et al., 2012b).

An updated version of the spectroscopic line parameters, which are used for the radiative transfer simulations needed for the generation of the look-up-table of WFM-DOAS, could potentially further improve the retrieval algorithm. However, this will need precise and accurate spectroscopic laboratory measurements in the future. Furthermore, the impact of chlorophyll fluorescence of vegetation, which results in an in-filling of O_2 absorption lines in the O_2-A band (see e.g., Joiner et al., 2011), on the SCIAMACHY XCO_2 can be investigated. As the consideration of fluorescence could further improve the quality of the retrieval results.

An application of a modified version of the WFM-DOAS retrieval algorithm can be the evaluation of the observations from TANSO on-board GOSAT in order to ex-

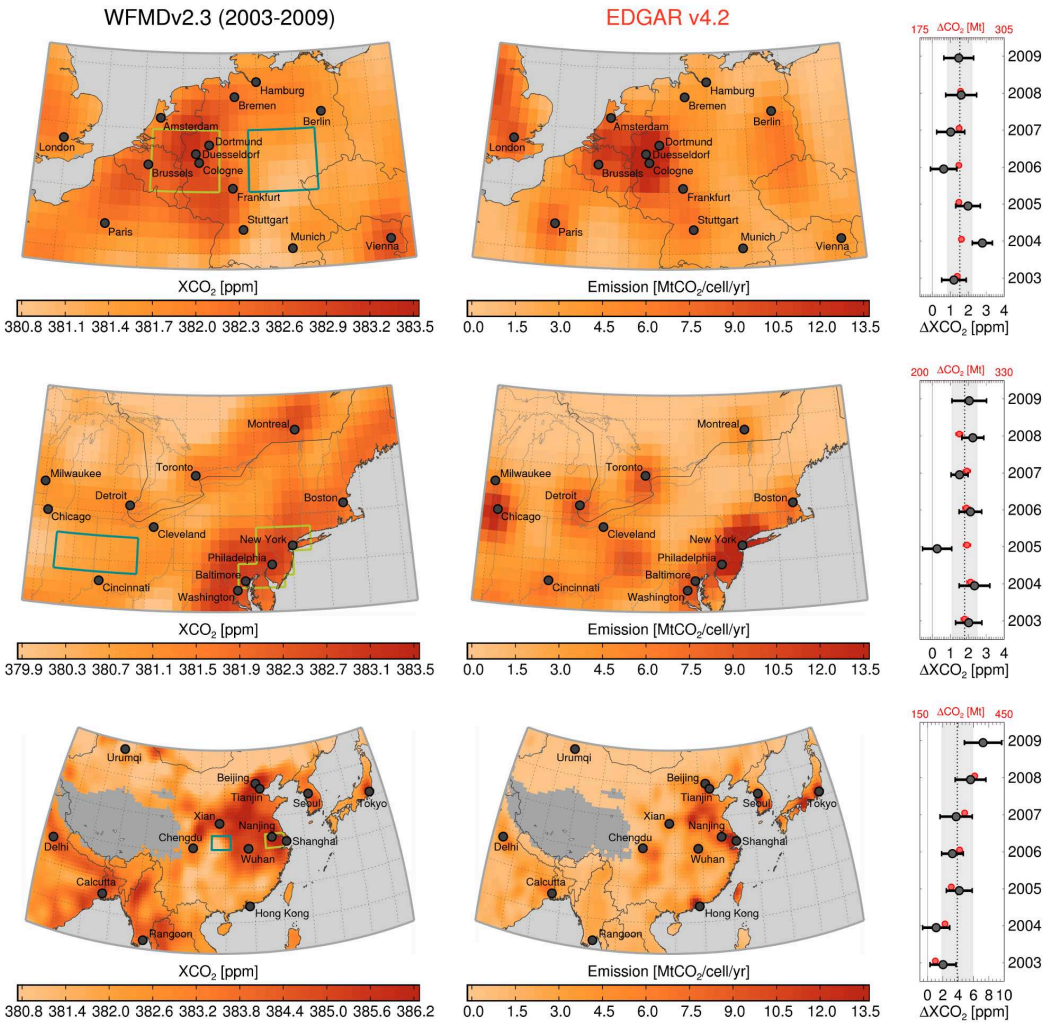

Figure 6.1: SCIAMACHY XCO_2 and EDGAR anthropogenic CO_2 emissions for three regions (from top to bottom: Rhine-Ruhr metropolitan region, East Coast of the United States and the Yangtze River Delta). Source regions (yellow rectangles) and background regions (teal rectangles) are defined in order to quantify regional XCO_2 enhancements. The right panel shows yearly XCO_2 source region enhancements (grey) with error bars compared to the yearly anthropogenic CO_2 emissions (red). The dotted lines are the mean enhancement and the shaded area the corresponding standard deviation.

pand the XCO_2 time series. In addition, a modified version of the algorithm can be utilised to evaluate observations of future satellite missions such as OCO-2 and CarbonSat. These instruments deliver order of magnitude of more observations than SCIAMACHY. Therefore, high processing speed such as provided by WFM-DOAS is besides high accuracy and precision a prerequisite for retrieval algorithms in order to evaluate the large amounts of data delivered by future satellites.

Appendix

A Impact of the Scan-Angle-Bias Correction on SCIAMACHY XCO_2 - Additional Figures

This part of the appendix shows the results of the comparison between the scan-angle-bias corrected and uncorrected SCIAMACHY WFM-DOAS XCO_2 data products, which is presented in Sec. 3.6.2, for all regions (see Fig. 3.8 and Tab. 3.2). The results of this comparison are also summarised in Tab. 3.3.

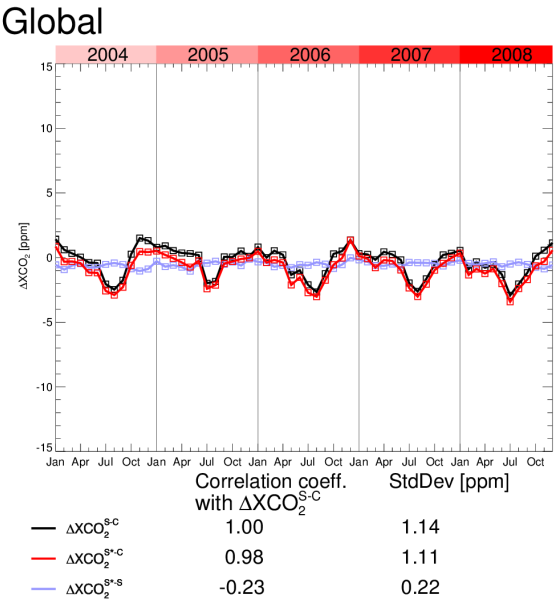

Figure A1: As Fig. 3.9 but global. Note that the range of the ΔXCO_2 axis is changed.

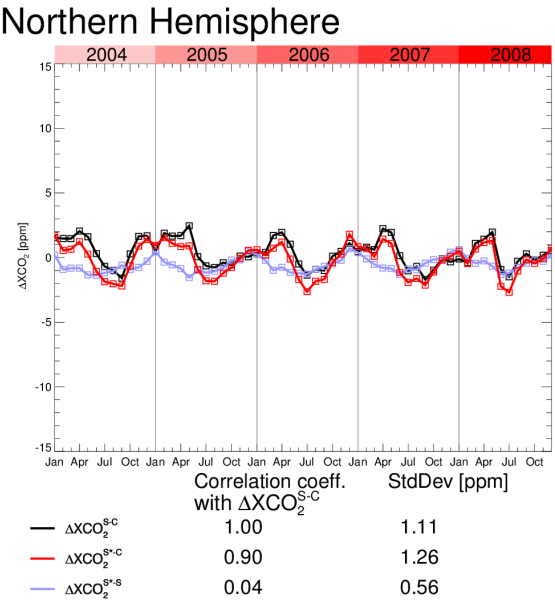

Figure A2: As Fig. 3.9 but for the Northern Hemisphere.

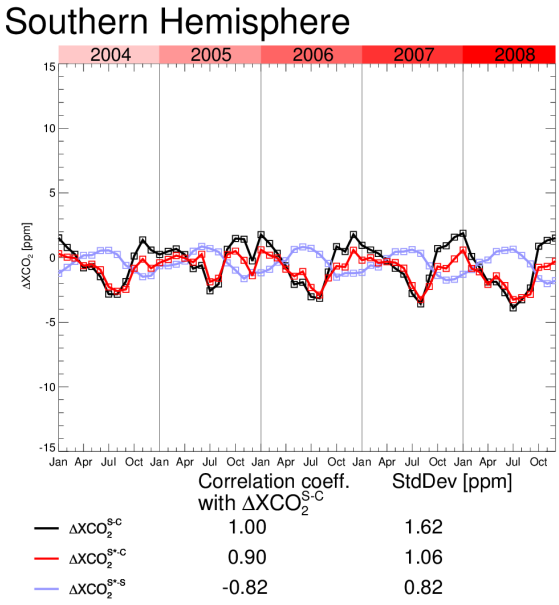

Figure A3: As Fig. 3.9 but for the Southern Hemisphere.

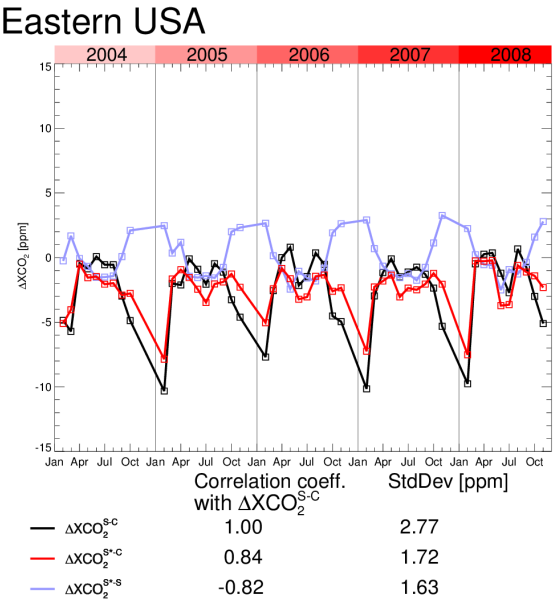

Figure A5: As Fig. 3.9 but for Eastern USA.

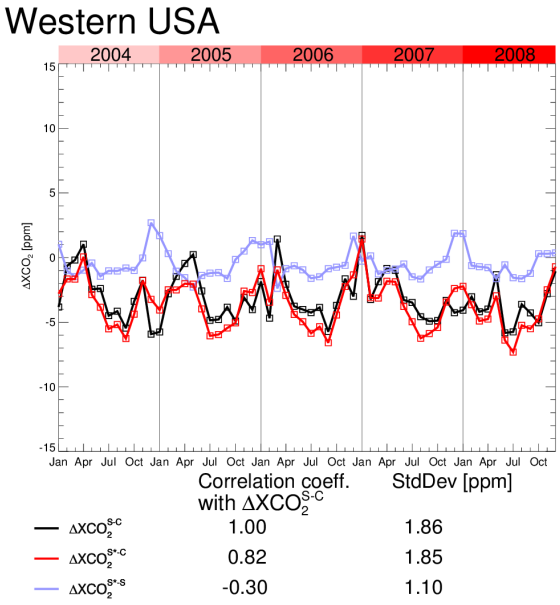

Figure A4: As Fig. 3.9 but for Western USA.

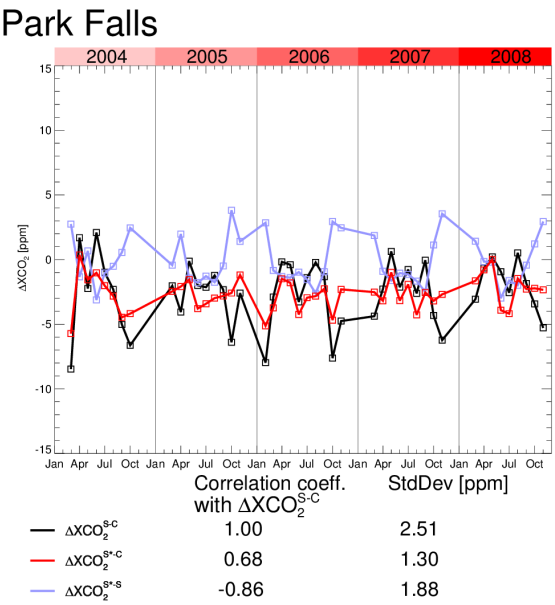

Figure A6: As Fig. 3.9 but for Park Falls.

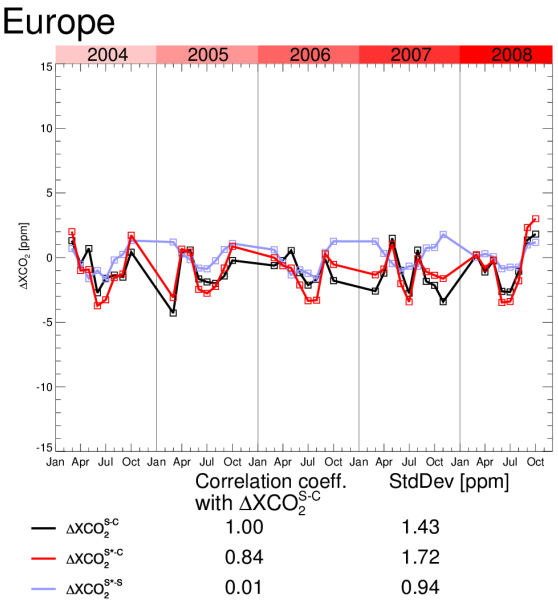

Figure A7: As Fig. 3.9 but for Europe.

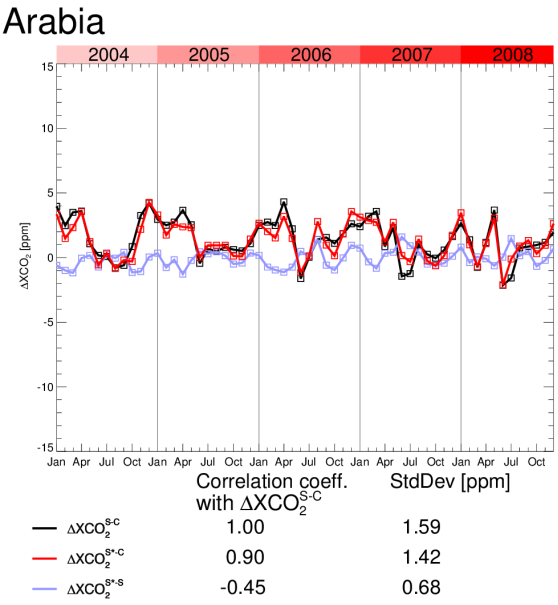

Figure A9: As Fig. 3.9 but for Arabia.

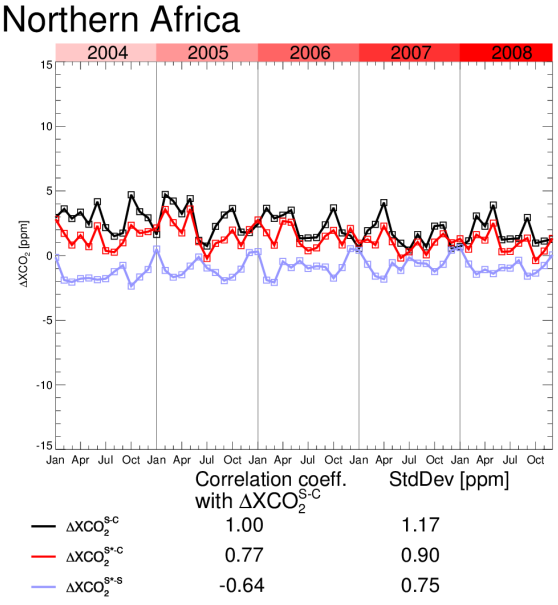

Figure A8: As Fig. 3.9 but for Northern Africa.

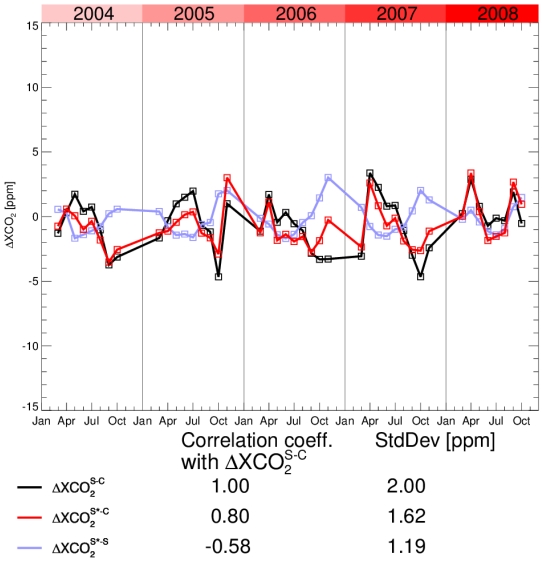

Figure A10: As Fig. 3.9 but for Russia.

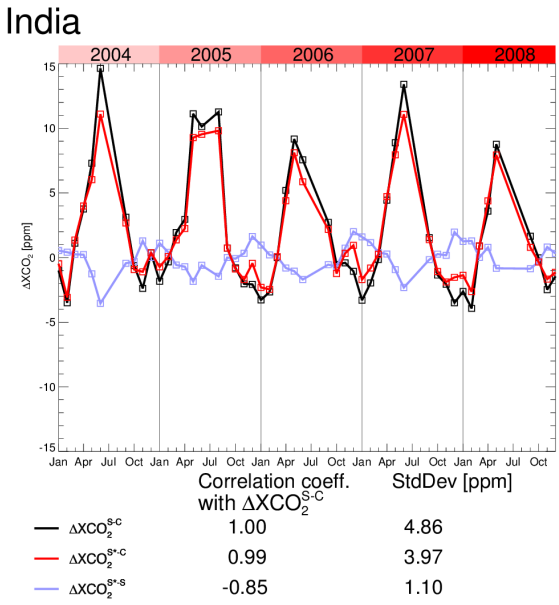

Figure A11: As Fig. 3.9 but for India.

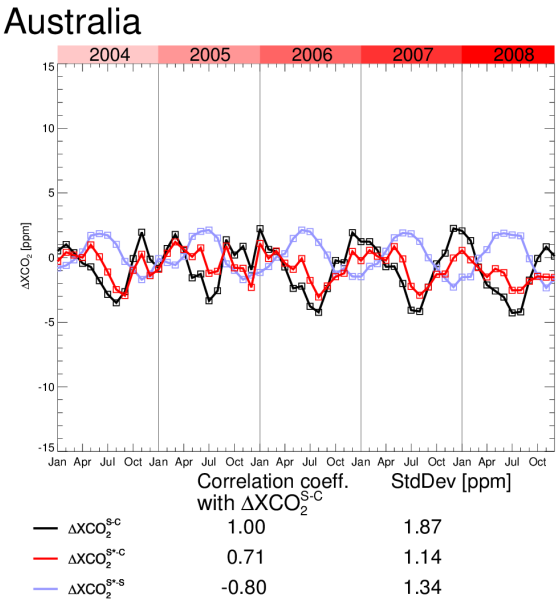

Figure A13: As Fig. 3.9 but for Australia.

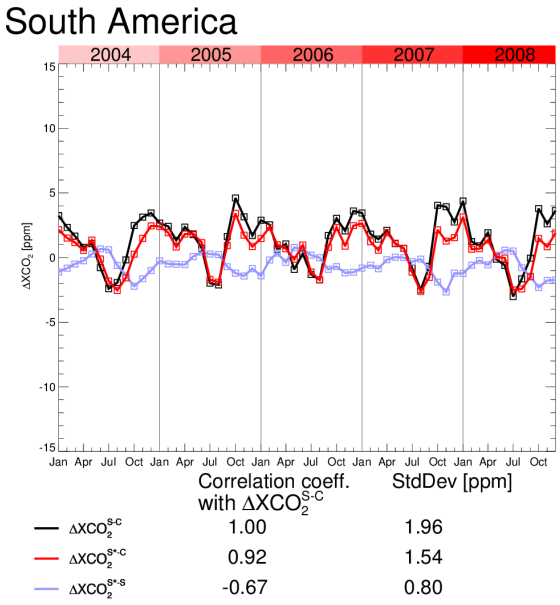

Figure A12: As Fig. 3.9 but for South America.

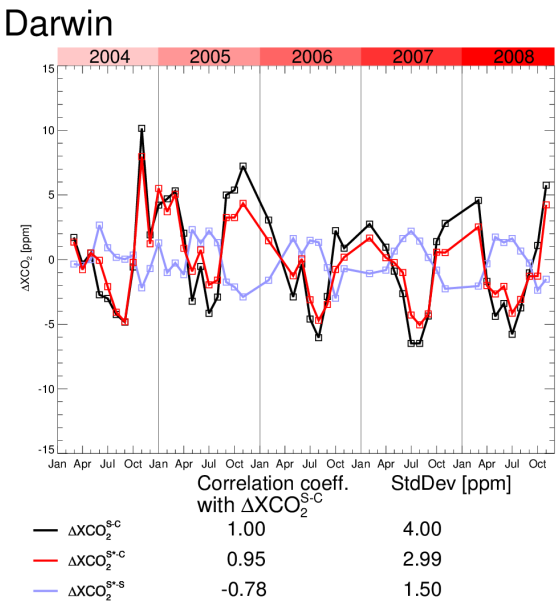

Figure A14: As Fig. 3.9 but for Darwin.

B Comparison of SCIAMACHY WFM-DOAS with CarbonTracker XCO_2 - Additional Figures

This part of the appendix is an extension of Sec. 4.3 and shows the results of the comparison between SCIAMACHY WFM-DOAS v2.1 XCO_2 and CarbonTracker XCO_2 focussing on aerosols and thin clouds for all investigated regions (see Fig. 3.8 and Tab. 3.2). All relevant values of this comparison can be found in Table 4.1.

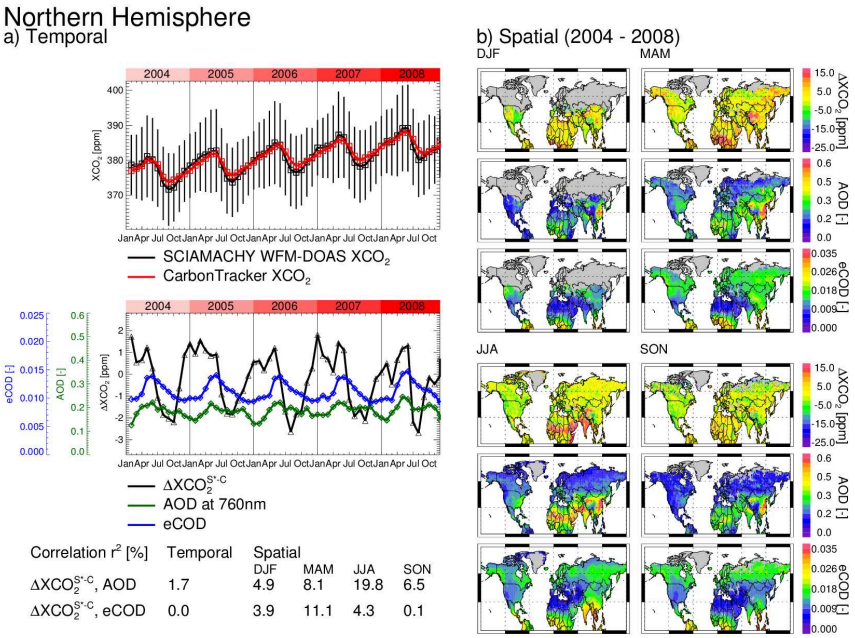

Figure B1: As Fig. 4.4 but for the Northern Hemisphere.

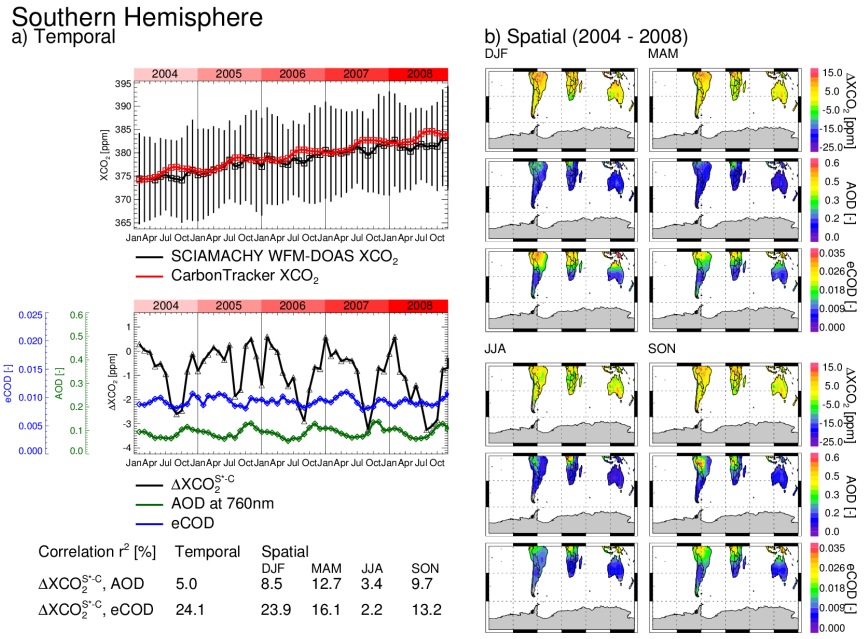

Figure B2: As Fig. 4.4 but for the Southern Hemisphere.

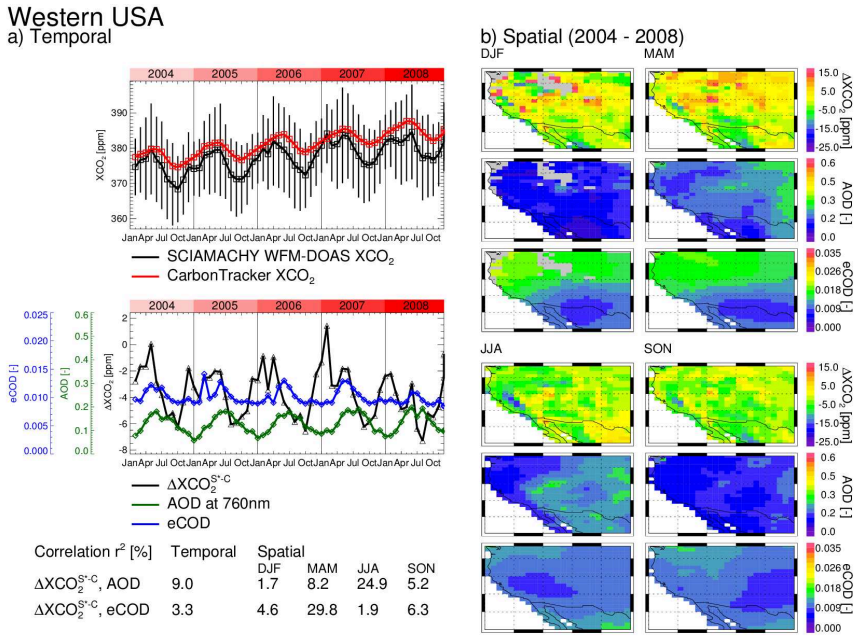

Figure B3: As Fig. 4.4 but for Western USA.

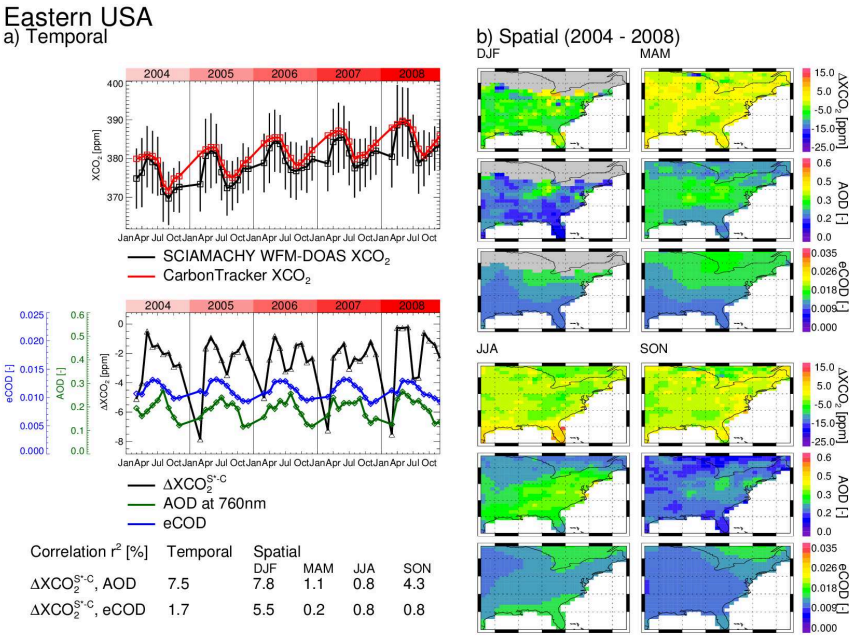

Figure B4: As Fig. 4.4 but for Eastern USA.

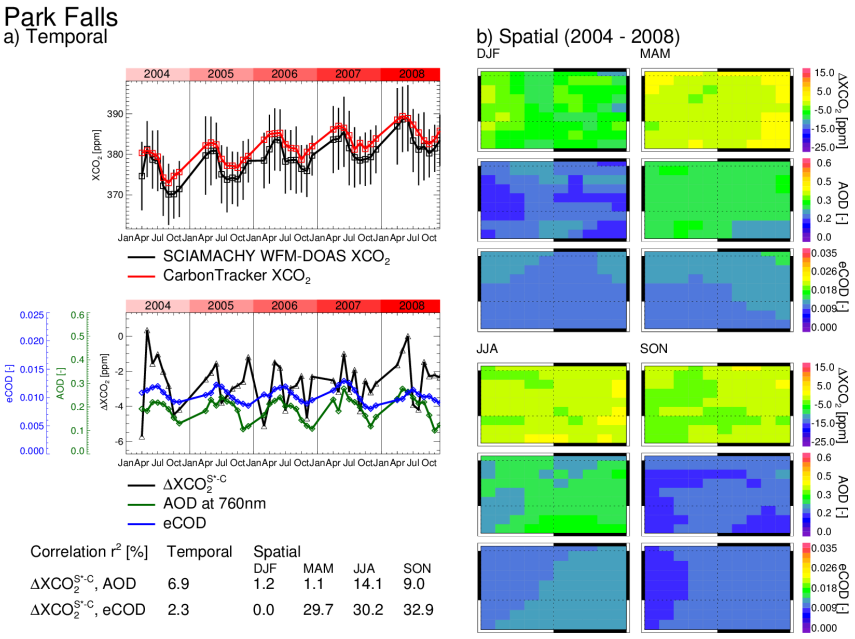

Figure B5: As Fig. 4.4 but for Park Falls.

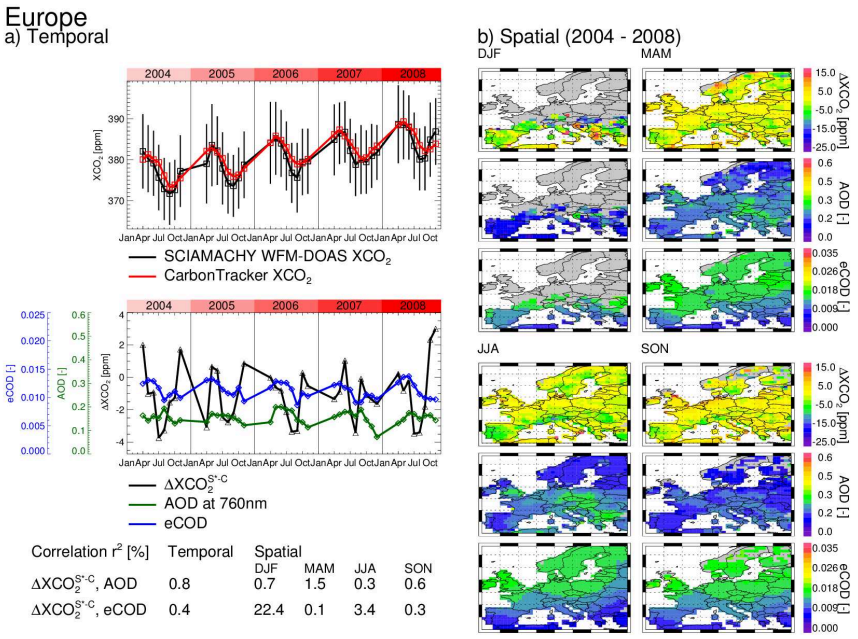

Figure B6: As Fig. 4.4 but for Europe.

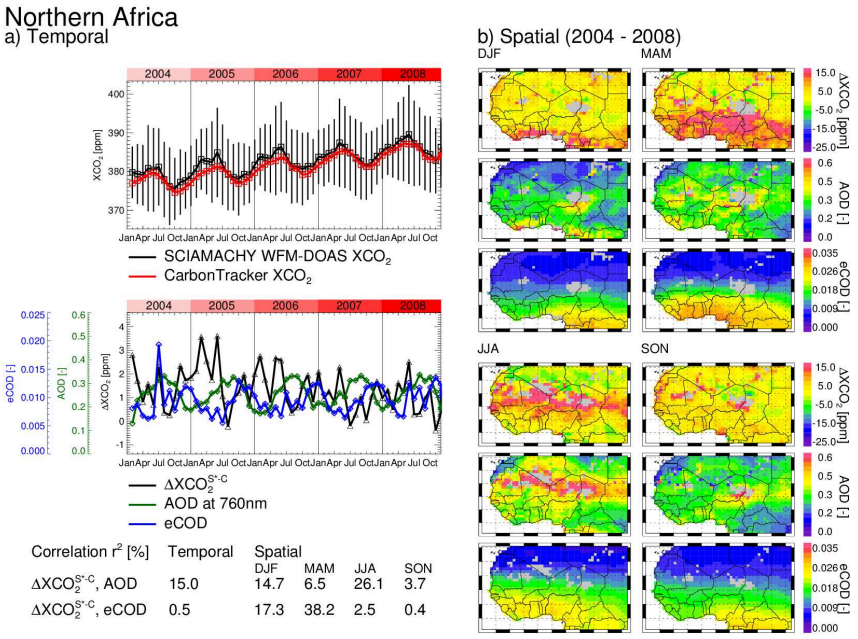

Figure B7: As Fig. 4.4 but for Northern Africa.

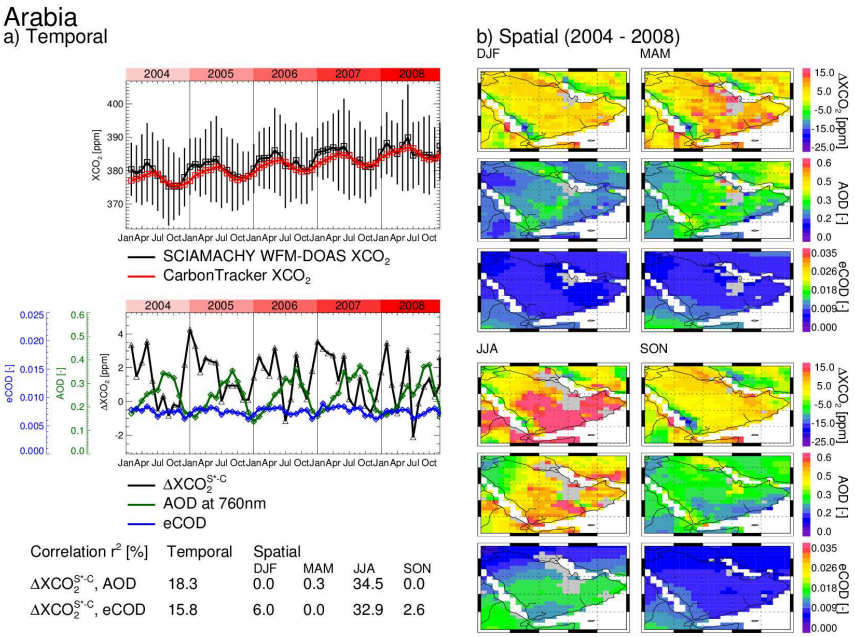

Figure B8: As Fig. 4.4 but for Arabia.

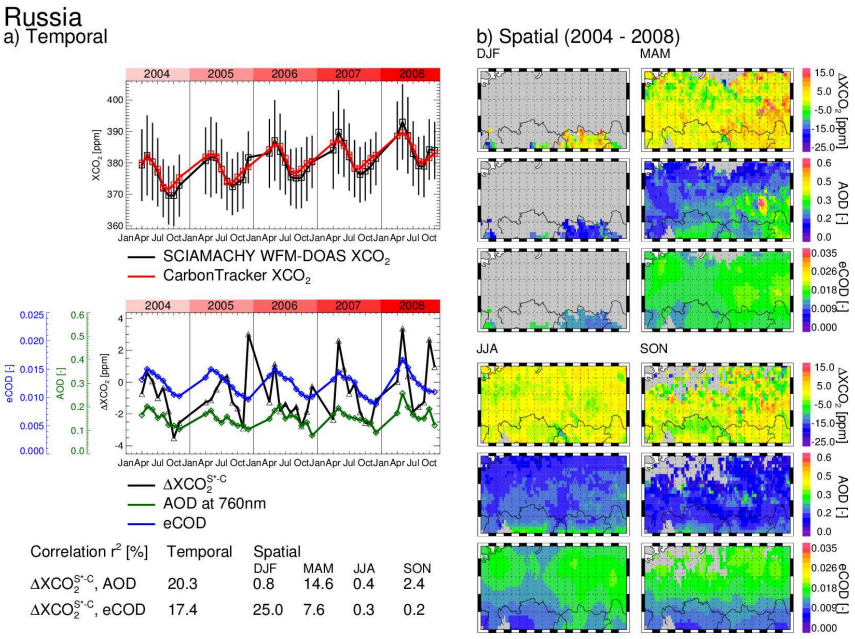

Figure B9: As Fig. 4.4 but for Russia.

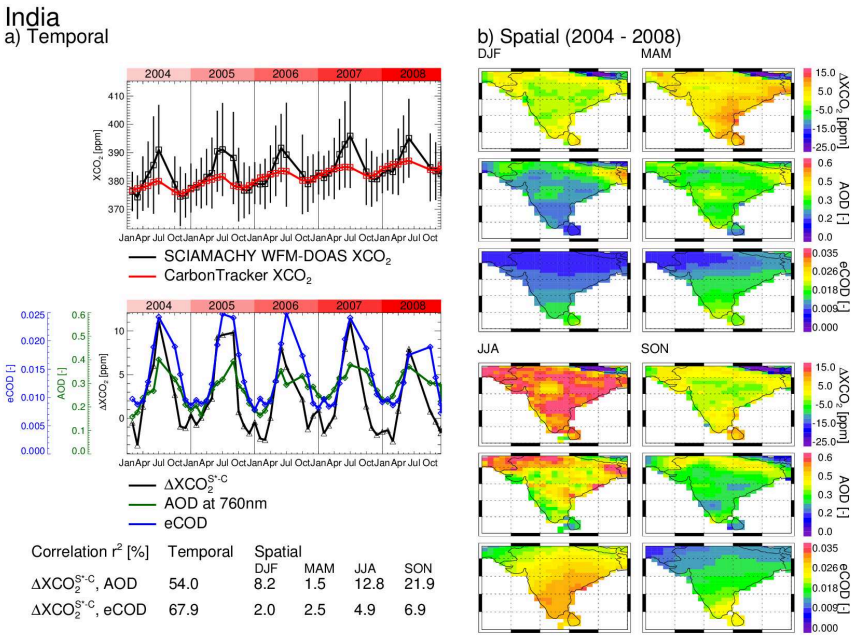

Figure B10: As Fig. 4.4 but for India.

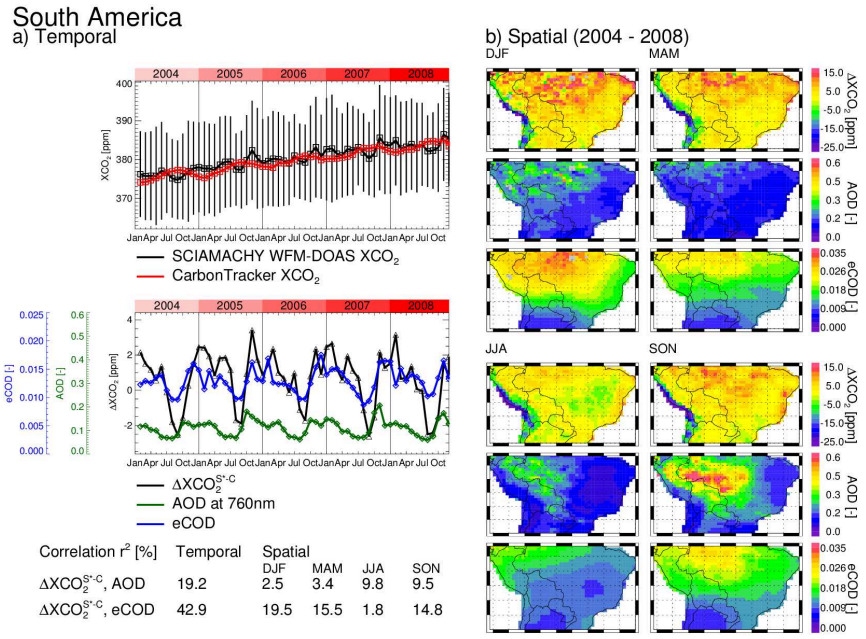

Figure B11: As Fig. 4.4 but for South America.

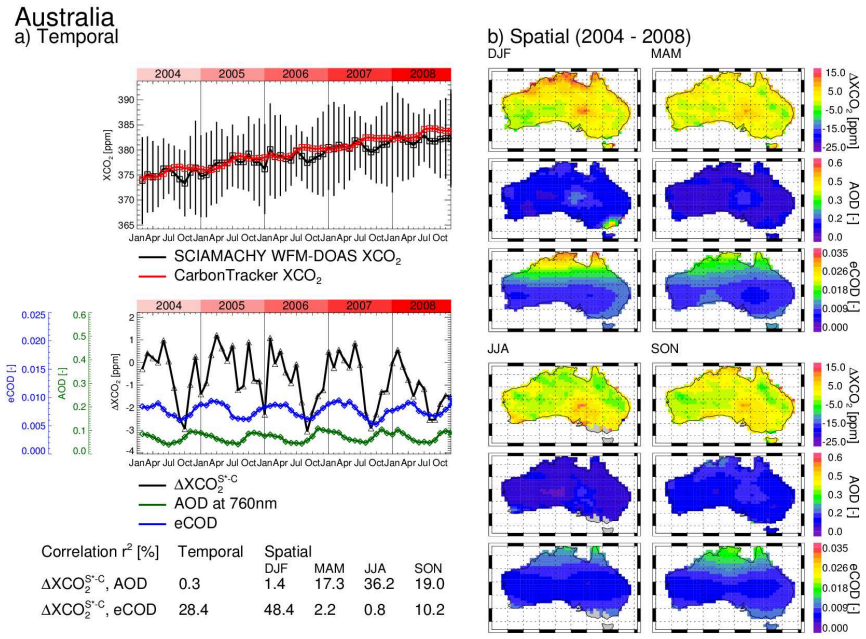

Figure B12: As Fig. 4.4 but for Australia.

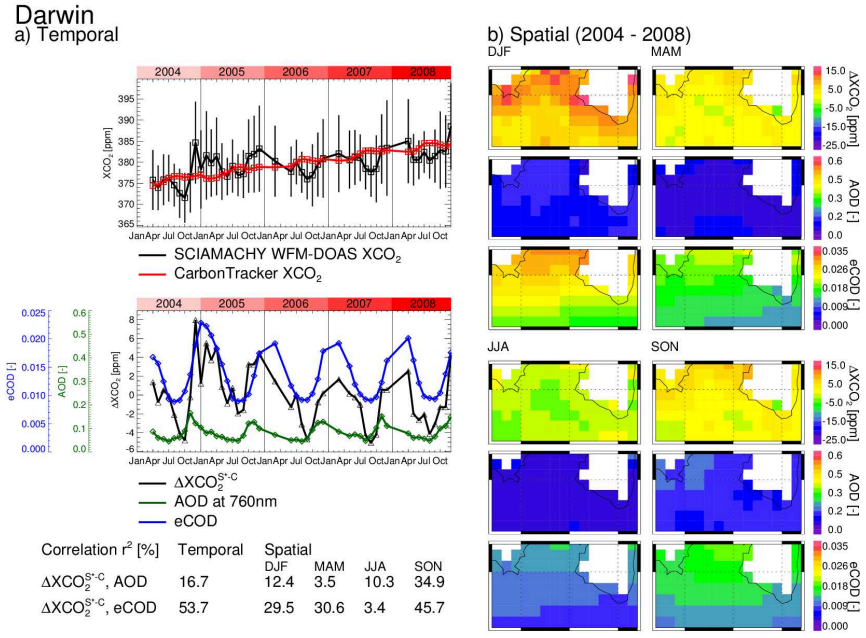

Figure B13: As Fig. 4.4 but for Darwin.

Bibliography

Aben, I., Hasekamp, O., and Hartmann, W.: Uncertainties in the space-based measurements of CO_2 columns due to scattering in the Earth's atmosphere, J. Quant. Spectrosc. Radiat. Transfer, 104, 450–459, doi:10.1016/j.jqsrt.2006.09.013, 2006.

Baldridge, A. M., Hook, S., Grove, C., and Rivera, G.: The ASTER Spectral Library Version 2.0, Remote Sensing of Environment, 113, 711–715, doi:10.1016/j.rse.2008.11.007, 2009.

Barkley, M. P., Frieß, U., and Monks, P. S.: Measuring atmospheric CO_2 from space using Full Spectral Initiation (FSI) WFM-DOAS, Atmos. Chem. Phys., 6, 3517–3534, 2006a.

Barkley, M. P., Monks, P. S., and Engelen, R. J.: Comparison of SCIAMACHY and AIRS CO_2 measurements over North America during the summer and autumn of 2003, Geophys. Res. Lett., 33, L20805, doi:10.1029/2006GL026807, 2006b.

Barkley, M. P., Monks, P. S., Frieß, U., Mittermeier, R. L., Fast, H., Körner, S., and Heimann, M.: Comparisons between SCIAMACHY atmospheric CO_2 retrieved using (FSI) WFM-DOAS to ground based FTIR data and the TM3 chemistry transport model, Atmos. Chem. Phys., 6, 4483–4498, 2006c.

Barkley, M. P., Monks, P. S., Hewitt, A. J., Machida, T., Desai, A., Vinnichenko, N., Nakazawa, T., Yu Arshinov, M., Fedoseev, N., and Watai, T.: Assessing the near surface sensitivity of SCIAMACHY atmospheric CO_2 retrieved using (FSI) WFM-DOAS, Atmos. Chem. Phys., 7, 3597–3619, 2007.

Barnes, W., Pagano, T., and Salomonson, V.: Prelaunch characteristics of the Moderate Resolution Imaging Spectroradiometer (MODIS) on EOS-AM1, Geoscience and Remote Sensing, IEEE Transactions on, 36, 1088 – 1100, doi:10.1109/36.700993, 1998.

Barrow, G. M.: Introduction to Molecular Spectroscopy, McGraw-Hill Education, 1962.

Basu, S., Houweling, S., Peters, W., Sweeney, C., Machida, T., Maksyutov, S., Patra, P. K., Saito, R., Chevallier, F., Niwa, Y., Matsueda, H., and Sawa, Y.: The seasonal cycle amplitude of total column CO_2: Factors behind the model-observation mismatch, J. Geophys. Res., 116, D23 306, doi:10.1029/2011JD016124, 2011.

Benedetti, A., Morcrette, J.-J., Boucher, O., Dethof, A., Engelen, R.-J., Fisher, M., Flentje, H., Huneeus, N., Jones, L., Kaiser, J. W., Kinne, S., Mangold, A., Razinger, M., Simmons, A. J., and Suttie, M.: Aerosol analysis and forecast in the European Centre for Medium-Range Weather Forecasts Integrated Forecast System: 2. Data assimilation, J. Geophys. Res., 114, D13 205, doi:10.1029/2008JD011115, 2009.

Bösch, H., Toon, G. C., Sen, B., Washenfelder, R. A., Wennberg, P. O., Buchwitz, M., de Beek, R., Burrows, J. P., Crisp, D., Christi, M., Connor, B. J., Natraj, V., and Yung, Y. L.: Space-based near-infrared CO_2 measurements: Testing the Orbiting Carbon Observatory retrieval algorithm and validation concept using SCIAMACHY observations over Park Falls, Wisconsin, J. Geophys. Res., 111, D23302, doi:10.1029/2006JD007080, 2006.

Bösch, H., Baker, D., Connor, B., Crisp, D., and Miller, C.: Global Characterization of CO_2 Column Retrievals from Shortwave-Infrared Satellite Observations of the Orbiting Carbon Observatory-2 Mission, Remote Sens., 3(2), 270–304, doi:10.3390/rs3020270, 2011.

Bousquet, P., Ciais, P., Miller, J. B., Dlugokencky, E. J., Hauglustaine, D. A., Prigent, C., Van der Werf, G. R., Peylin, P., Brunke, E.-G., Carouge, C., Langenfelds, R. L., Lathiere, J., Papa, F., Ramonet, M., Schmidt, M., Steele, L. P., Tyler, S. C., and White, J.: Contribution of anthropogenic and natural sources to atmospheric methane variability, Nature, 443, 439–443, doi:10.1038/nature05132, 2006.

Bovensmann, H., Burrows, J. P., Buchwitz, M., Frerick, J., Noël, S., Rozanov, V. V., Chance, K. V., and Goede, A.: SCIAMACHY – Mission Objectives and Measurement Modes, J. Atmos. Sci., 56, 127–150, 1999.

Bovensmann, H., Buchwitz, M., Burrows, J. P., Reuter, M., Krings, T., Gerilowski, K., Schneising, O., Heymann, J., Tretner, A., and Erzinger, J.: A remote sensing technique for global monitoring of power plant CO_2 emissions from space and related applications, Atmos. Meas. Tech., 3, 781–811, doi:10.5194/amt-3-781-2010, 2010.

Brasseur, G. P., Orlando, J. J., and Tyndall, G. S., eds.: Atmospheric Chemistry and Global Change, Oxford University Press, New York, Oxford, 1999.

Bril, A., Oshchepkov, S., Yokota, T., and Inoue, G.: Parameterization of aerosol and cirrus cloud effects on reflected sunlight spectra measured from space: application of the equivalence theorem, Appl. Opt., 46, 2460–2470, 2007.

Buchwitz, M.: Strahlungstransport und Inversions-Algorithmen zur Ableitung atmosphärischer Spurengasinformationen aus Erdfernerkundungsmessungen in Nadirgeometrie im ultravioletten bis nahinfraroten Spektralbereich am Beispiel SCIAMACHY, Ph.D. thesis, University of Bremen, URL http://nbn-resolving.de/urn:nbn:de:gbv:46-diss000000338, 2000.

Buchwitz, M. and Burrows, J. P.: Retrieval of CH_4, CO, and CO_2 total column amounts from SCIAMACHY near-infrared nadir spectra: Retrieval algorithm and first results, in: Remote Sensing of Clouds and the Atmosphere VIII, edited by: Schäfer, K. P., Comèron, A., Carleer, M. R., and Picard, R. H., Proceedings of SPIE, 5235, 375–388, 2004.

Buchwitz, M., Rozanov, V. V., and Burrows, J. P.: A correlated-k distribution scheme for overlapping gases suitable for retrieval of atmospheric constituents from moderate resolution radiance measurements in the visible/near-infrared spectral region, J. Geophys. Res., 105, 15 247–15 261, 2000a.

Buchwitz, M., Rozanov, V. V., and Burrows, J. P.: A near-infrared optimized DOAS method for the fast global retrieval of atmospheric CH_4, CO, CO_2, H_2O, and N_2O total column amounts from SCIAMACHY Envisat-1 nadir radiances, J. Geophys. Res., 105, 15 231–15 245, 2000b.

Buchwitz, M., de Beek, R., Burrows, J. P., Bovensmann, H., Warneke, T., Notholt, J., Meirink, J. F., Goede, A. P. H., Bergamaschi, P., Körner, S., Heimann, M., and Schulz, A.: Atmospheric methane and carbon dioxide from SCIAMACHY satellite data: initial comparison with chemistry and transport models, Atmos. Chem. Phys., 5, 941–962, 2005a.

Buchwitz, M., de Beek, R., Noël, S., Burrows, J. P., Bovensmann, H., Bremer, H., Bergamaschi, P., Körner, S., and Heimann, M.: Carbon monoxide, methane and carbon dioxide columns retrieved from SCIAMACHY by WFM-DOAS: year 2003 initial data set, Atmos. Chem. Phys., 5, 3313–3329, 2005b.

Buchwitz, M., de Beek, R., Noël, S., Burrows, J. P., Bovensmann, H., Schneising, O., Khlystova, I., Bruns, M., Bremer, H., Bergamaschi, P., Körner, S., and Heimann,

M.: Atmospheric carbon gases retrieved from SCIAMACHY by WFM-DOAS: version 0.5 CO and CH_4 and impact of calibration improvements on CO_2 retrieval, Atmos. Chem. Phys., 6, 2727–2751, 2006.

Buchwitz, M., Schneising, O., Burrows, J. P., Bovensmann, H., Reuter, M., and Notholt, J.: First direct observation of the atmospheric CO_2 year-to-year increase from space, Atmos. Chem. Phys., 7, 4249–4256, 2007.

Burrows, J. P., Hölzle, E., Goede, A. P. H., Visser, H., and Fricke, W.: SCIAMACHY – Scanning Imaging Absorption Spectrometer for Atmospheric Chartography, Acta Astronautica, 35, 445–451, 1995.

Burrows, J. P., Platt, U., and Borrell, P., eds.: The Remote Sensing of Tropospheric Composition from Space, Springer Verlag, Heidelberg, doi:10.1007/978-3-642-14791-3, 2011.

Butz, A., Hasekamp, O. P., Frankenberg, C., and Aben, I.: Retrievals of atmospheric CO_2 from simulated space-borne measurements of backscatteres near-infrared sunlight: accounting for aerosol effects, Applied Optics, 48, 3322–3336, 2009.

Caldeira, K. and Wickett, M. E.: Anthropogenic carbon and ocean pH, Nature, 425, 365, 2003.

Canadell, J. G., Le Quéré, C., Raupach, M. R., Field, C. B., Buitenhuis, E. T., Ciais, P., Conway, T. J., Gillett, N. P., Houghton, R. A., and Marland, G.: Contributions to accelerating atmospheric CO_2 growth from economic activity, carbon intensity, and efficiency of natural sinks, Proceedings of the National Academy of Sciences (PNAS) of the United States of America, November 20, 2007, 104, 18 866–18 870, 2007.

Chevallier, F., Bréon, F.-M., and Rayner, P. J.: Contribution of the Orbiting Carbon Observatory to the estimation of CO_2 sources and sinks: Theoretical study in a variational data assimilation framework, J. Geophys. Res., 112, D09307, doi:10.1029/2006JD007375, 2007.

Crisp, D., Atlas, R. M., Bréon, F.-M., Brown, L. R., Burrows, J. P., Ciais, P., Connor, B. J., Doney, S. C., Fung, I. Y., Jacob, D. J., Miller, C. E., O'Brien, D., Pawson, S., Randerson, J. T., Rayner, P., Salawitch, R. S., Sander, S. P., Sen, B., Stephens, G. L., Tans, P. P., Toon, G. C., Wennberg, P. O., Wofsy, S. C., Yung, Y. L., Kuang, Z., Chudasama, B., Sprague, G., Weiss, P., Pollock, R., Kenyon, D., and Schroll, S.: The Orbiting Carbon Observatory (OCO) mission, Adv. Space Res., 34, 700–709, 2004.

Crisp, D., Boland, S., Bösch, H., Brown, L., Burrows, J. P., Ciais, P., Connor, B., Denning, S., Doney, S., Engelen, R., Fung, I., Griffith, P., Jacob, D., Johnson, B., Martin-Torres, J., Michalak, A., Miller, C., O'Brien, D., Polonsky, I., Potter, C., Randerson, J., Rayner, P., Salawitch, R., Santee, M., Tans, P., Wennberg, P., Wunch, D., Wofsy, S., and Yung, Y.: The Need for Atmospheric Carbon Dioxide Measurements from Space: Contributions from a Rapid Reflight of the Orbiting Carbon Observatory, Tech. rep., OCO White Paper, 2009.

d'Almeida, G., Koepke, P., and Shettle, E.: Atmospheric Aerosol: global climatology and radiative characteristics, Deepak Publ., Hampton, VA, 1991.

Dubin, M., Hull, A. R., and Champion, K. S. W., eds.: U.S. Standard Atmosphere, 1976, U.S. Government Printing Office, Washington, D.C., 1976.

Dufour, E. and Bréon, F.-M.: Spaceborn estimate of atmospheric CO_2 column by use of the differential absorption method: error analysis, Appl. Opt., 42, 3595–3609, 2003.

Efron, B.: Bootstrap Methods: Another Look at the Jackknife, Ann. Statist., 7, 1–26, doi:10.1214/aos/1176344552, 1979.

Field, C.: Plant Physiology of the "Missing" Carbon Sink, Plant Physiology, 125, 25–28, doi:10.1104/pp.125.1.25, 2001.

Friedlingstein, P., Cox, P., Betts, R., Bopp, L., von Bloh, W., Brovkin, V., Cadule, P., Doney, S., Eby, M., Fung, I., Bala, G., John, J., Jones, C., Joos, F., Kato, T., Kawamiya, M., Knorr, W., Lindsay, K., Metthews, H. D., Raddatz, T., Rayner, P., Reick, C., Roeckner, E., Schnitzler, K.-G., Schnur, R., Strassmann, K., Weaver, A. J., Yoshikawa, C., and Zeng, N.: Climate-Carbon Cycle Feedback Analysis: Results from the C^4MIP Model Intercomparison, Journal of Climate, 19, 3337–3353, 2006.

Gao, B.-C., Goetz, A. F. H., and Wiscombe, W. J.: Cirrus cloud detection from airborne imaging spectromter data using the 1.38 μm water vapor band, Geophys. Res. Lett., 20, 301–304, 1993.

Goody, R.: Principles of Atmospheric Physics and Chemistry, Oxford University Press, New York, 1995.

Gottwald, M. and Bovensmann, H., eds.: SCIAMACHY - Exploring the Changing Earth's Atmosphere, Springer, 2011.

Grainger, J. F. and Ring, J.: Anomalous Fraunhofer Line Profiles, Nature, 193, 762, doi:10.1038/193762a0, 1962.

Haken, H. and Wolf, H. C.: Molekülphysik und Quantenchemie, Springer, Berlin, 2006.

Herzberg, G.: Einführung in die Molekülspektroskopie, Dr. Dietrich Steinkopff Verlag, Darmstadt, 1973.

Heymann, J., Schneising, O., Reuter, M., Buchwitz, M., Rozanov, V., Velazco, V. A., Bovensmann, H., and Burrows, J. P.: SCIAMACHY WFM-DOAS XCO_2: comparison with CarbonTracker XCO_2 focusing on aerosols and thin clouds, Atmos. Meas. Tech., 5, 1935–1952, doi:10.5194/amt-5-1935-2012, 2012a.

Heymann, J., Bovensmann, H., Buchwitz, M., Burrows, J. P., Deutscher, N. M., Notholt, J., Rettinger, M., Reuter, M., S. O., Sussmann, R., and Warneke, T.: SCIAMACHY WFM-DOAS XCO_2: reduction of scattering related errors, Atmos. Meas. Tech., 5, 2375–2390, doi:10.5194/amt-5-2375-2012, 2012b.

Hoogen, R.: Mie Theory Outline & IUPMIE User's Guide, Tech. rep., University of Bremen, 1995.

Houweling, S., Breon, F.-M., Aben, I., Rödenbeck, C., Gloor, M., Heimann, M., and Ciais, P.: Inverse modeling of CO_2 sources and sinks using satellite data: a synthetic inter-comparison of measurement techniques and their performance as a function of space and time, Atmos. Chem. Phys., 4, 523–538, 2004.

Houweling, S., Hartmann, W., Aben, I., Schrijver, H., Skidmore, J., Roelofs, G.-J., and Breon, F.-M.: Evidence of systematic errors in SCIAMACHY-observed CO_2 due to aerosols, Atmos. Chem. Phys., 5, 3003–3013, 2005.

Joiner, J., Yoshida, Y., Vasilkov, A. P., Yoshida, Y., Corp, L. A., and Middleton, E. M.: First observations of global and seasonal terrestrial chlorophyll flourescence from space, Biogeosciences, 8, 637–651, doi:10.5194/bg-8-637-2011, 2011.

Karion, A., Sweeney, C., Tans, P., and Newberger, T.: AirCore: An Innovative Atmospheric Sampling System, J. Atmos. Oceanic Technol., 27, 1839–1853, doi:10.1175/2010jtecha1448.1, 2010.

Kauss, J.: Aerosol-Parameterisierung für Strahlungstransport-Simulationen im ultravioletten bis nahinfraroten Spektralbereich, Master's thesis, Universität Bremen, 1998.

Keppel-Aleks, G., Wennberg, P. O., Washenfelder, R. A., Wunch, D., Schneider, T., Toon, G. C., Andres, R. J., Blavier, J.-F., Connor, B., Davis, K. J., Desai, A. R., Messerschmidt, J., Notholt, J., Roehl, C. M., Sherlock, V., Stephens, B. B., Vay, S. A., and Wofsy, S. C.: The imprint of surface fluxes and transport on variations in total column carbon dioxide, Biogeosciences, 9, 875–891, doi:10.5194/bg-9-875-2012, 2012.

Kokhanovsky, A. A.: Cloud Optics, Springer, 2006.

Kuang, Z., Margolis, J., Toon, G., Crisp, D., and Yung, Y.: Spaceborne measurements of atmospheric CO_2 by high-resolution NIR spectrometry of reflected sunlight: an introductory study, Geophy. Res. Let., 29, 1716, doi:10.1029/2001GL014298, 2002.

Kuze, A., Suto, H., Nakajima, M., and Hamazaki, T.: Thermal and near infrared sensor for carbon observation Fourier-transform spectrometer on the Greenhouse Gases Observing Satellite for greenhouse gases monitoring, Appl. Opt., 48, 6716–6733, 2009.

Marquis, M. and Tans, P.: Carbon Crucible, SCIENCE, 320, 460–461, doi: 10.1126/science.1156451, 2008.

Messerschmidt, J., Parazoo, N., Deutscher, N. M., Roehl, C., Warneke, T., Wennberg, P. O., and Wunch, D.: Evaluation of atmosphere-biosphere exchange estimations with TCCON measurements, Atmos. Chem. Phys. Discuss., 12, 12 759–12 800, doi: 10.5194/acpd-12-12759-2012, 2012.

Mie, G.: Beiträge zur Optik trüber Medien, speziell kolloidaler Metallösungen, Ann. Phys., 330, 377–445, 1908.

Miller, C. E., Crisp, D., DeCola, P. L., Olsen, S. C., Randerson, J. T., Michalak, A. M., Alkhaled, A., Rayner, P., Jacob, D. J., Suntharalingam, P., Jones, D. B. A., Denning, A. S., Nicholls, M. E., Doney, S. C., Pawson, S., Boesch, H., Connor, B. J., Fung, I. Y., O'Brien, D., Salawitch, R. J., Sander, S. P., Sen, B., Tans, P., Toon, G. C., Wennberg, P. O., Wofsy, S. C., Yung, Y. L., and Law, R. M.: Precision requirements for space-based X_{CO_2} data, J. Geophys. Res., 112, D10314, doi:10.1029/2006JD007659, 2007.

Morcrette, J.-J., Boucher, O., Jones, L., Salmond, D., Bechtold, P., Beljaars, A., Benedetti, A., Bonet, A., Kaiser, W., Razinger, M., Schulz, M., Serrar, S., Simmons, A. J., Sofiev, M., Suttie, M., Tompkins, A., and Untch, A.: Aerosol analysis and forecast in the European Centre for Medium-Range Weather Forecasts Integrated Forecast System: Forward modeling, J. Geophy. Res., 114, D06 206, doi: 10.1029/2008JD011235, 2009.

Myneni, R., Dong, J., Tucker, C., Kaufmann, R., Kauppi, P., Liski, J., Zhou, L., Alexeyev, V., and Hughes, M.: A large carbon sink in the woody biomass of Northern forests, Proc. Natl. Acad. Sci. USA, 98, 14 784–14 789, doi:10.1073/pnas.261555198, 2001.

Nakićenović, N. and Swart, R., eds.: Special Report on Emissions Scenarios. A Special Report of Working Group III of the Intergovernmental Panel on Climate Change, Cambridge University Press, 2000.

Noël, S., Buchwitz, M., Bovensmann, H., and Burrows, J. P.: Validation of SCIAMACHY AMC-DOAS water vapour columns, Atmos. Chem. Phys., 5, 1835–1841, doi:10.5194/acp-5-1835-2005, 2005.

O'Brien, D. M. and Rayner, P. J.: Global observations of the carbon budget 2. CO_2 column from differential absorption of reflected sunlight in the 1.61 μm band of CO_2, J. Geophys. Res., 107, 4354, doi:10.1029/2001JD000617, 2002.

O'Dell, C. W., Connor, B., Bösch, H., O'Brien, D., Frankenberg, C., Castano, R., Christi, M., Eldering, D., Fisher, B., Gunson, M., McDuffie, J., Miller, C. E., Natraj, V., Oyafuso, F., Polonsky, I., Smyth, M., Taylor, T., Toon, G. C., Wennberg, P. O., and Wunch, D.: The ACOS CO_2 retrieval algorithm - Part 1: Description and validation against synthetic observations, Atmos. Meas. Tech., 5, 99–121, doi:10.5194/amt-5-99-2012, 2012.

Peters, W., Jacobson, A. R., Sweeney, C., Andrews, A. E., Conway, T. J., Masarie, K., Miller, J. B., Bruhwiler, L. M. P., Petron, G., Hirsch, A. I., Worthy, D. E. J., van der Werf, G. R., Randerson, J. T., Wennberg, P. O., Krol, M. C., and Tans, P. P.: An atmospheric perspective on North American carbon dioxide exchange: CarbonTracker, Proc. Natl. Acad. Sci. USA, 104, 18 925–18 930, doi:10.1073/pnas.0708986104, 2007.

Pregitzer, K., Burton, A., Zak, D., and Talhelm, A.: Simulated chronic nitrogen deposition increases carbon storage in Northern Temperate forests, Global Change Biology, 14, 142–153, doi:10.1111/j.1365-2486.2007.01465.x, 2008.

Rayner, P. J. and O'Brien, D. M.: The utility of remotely sensed CO_2 concentration data in surface inversions, Geophys. Res. Lett., 28, 175–178, 2001.

Reuter, M., Buchwitz, M., Schneising, O., Heymann, J., Bovensmann, H., and Burrows, J. P.: A method for improved SCIAMACHY CO_2 retrieval in the presence of optically thin clouds, Atmos. Meas. Tech., 3, 209–232, URL `www.atmos-meas-tech.net/3/209/2010/`, 2010.

Reuter, M., Bovensmann, H., Buchwitz, M., Burrows, J. P., Connor, B. J., Deutscher, N. M., Griffith, D. W. T., Heymann, J., Keppel-Aleks, G., Messerschmidt, J., Notholt, J., Petri, C., Robinson, J., Schneising, O., Sherlock, V., Velazco, V., Warneke, T., Wennberg, P. O., and Wunch, D.: Retrieval of atmospheric CO_2 with enhanced accuracy and precision from SCIAMACHY: Validation with FTS measurements and comparison with model results„ J. Geophys. Res., 116, D04 301, doi:10.1029/2010JD015047, 2011.

Reuter, M., Bovensmann, H., Buchwitz, M., Burrows, J., Deutscher, N., Heymann, J., Rozanov, A., Schneising, O., Suto, H., Toon, G., and Warneke, T.: On the potential of the 2041–2047nm spectral region for remote sensing of atmospheric CO_2 isotopologues, Journal of Quantitative Spectroscopy and Radiative Transfer, 12, 2012a.

Reuter, M., Bösch, H., Bovensmann, H., Bril, A., Buchwitz, M., Butz, A., Burrows, J. P., O'Dell, C. W., Guerlet, S., Hasekamp, O., Heymann, J., Kikuchi, N., Oshchepkov, S., Parker, R., Pfeifer, S., Schneising, O., Yokota, T., and Yoshida, Y.: A joint effort to deliver satellite retrieved atmospheric CO_2 concentrations for surface flux inversions: the ensemble median algorithm EMMA, Atmos. Chem. Phys. Discuss., 12, 23 195–23 217, doi:10.5194/acpd-12-23195-2012, 2012b.

Rodgers, C. D.: Inverse Methods for Atmospheric Sounding: Theory and Practice, World Scientific Publishing, Singapore, 2000.

Roedel, W.: Physik unserer Umwelt: die Atmosphäre, Springer-Verlag Berlin Heidelberg New York, 2000.

Rothman, L. S., Gordon, I. E., Barbe, A., Benner, D. C., Bernath, P. E., Birk, M., Boudon, V., Brown, L. R., Campargue, A., Champion, J. P., Chance, K., Coudert, L. H., Dana, V., Devi, V. M., Fally, S., Flaud, J. M., Gamache, R. R., Goldman, A., Jacquemart, D., Kleiner, I., Lacome, N., Lafferty, W. J., Mandin, J. Y., Massie, S. T., Mikhailenko, S. N., Miller, C. E., Moazzen-Ahmadi, N., Naumenko, O. V., Nikitin, A. V., Orphal, J., Perevalov, V. I., Perrin, A., Predoi-Cross, A., Rinsland, C. P., Rotger, M., Simeckova, M., Smith, M. A. H., Sung, K., Tashkun, S. A., Tennyson, J., Toth, R. A., Vandaele, A. C., and Vander Auwera, J.: The HITRAN 2008 molecular spectroscopic database, J. Quant. Spectrosc. Ra., 110, 533–572, doi:10.1016/j.jqsrt.2009.02.013, 2009.

Rozanov, A., Rozanov, V., Buchwitz, M., Kokhanovsky, A., and Burrows, J.: SCIATRAN 2.0 - A new radiative transfer model for geophysical applications in the 175-2400 nm spectral region, in: Atmospheric remote sensing: Earth's surface, troposphere, stratosphere and mesosphere - I, edited by Burrows, J. and Eichmann, K., vol. 36

of *Adv. Space Res.*, pp. 1015–1019, doi:10.1016/j.asr.2005.03.012, 35th COSPAR Scientific Assembly, Paris, France, JUL 18-25, 2004, 2005.

Schneising, O., Buchwitz, M., Burrows, J. P., Bovensmann, H., Reuter, M., Notholt, J., Macatangay, R., and Warneke, T.: Three years of greenhouse gas column-averaged dry air mole fractions retrieved from satellite - Part 1: Carbon dioxide, Atmos. Chem. Phys., 8, 3827–3853, 2008.

Schneising, O., Buchwitz, M., Burrows, J. P., Bovensmann, H., Bergamaschi, P., and Peters, W.: Three years of greenhouse gas column-averaged dry air mole fractions retrieved from satellite - Part 2: Methane, Atmos. Chem. Phys., 9, 443–465, 2009.

Schneising, O., Buchwitz, M., Reuter, M., Heymann, J., Bovensmann, H., and Burrows, J. P.: Long-term analysis of carbon dioxide and methane column-averaged mole fractions retrieved from SCIAMACHY, Atmos. Chem. Phys., 11, 2863–2880, doi:10.5194/acp-11-2863-2011, 2011.

Schneising, O., Bergamaschi, P., Bovensmann, H., Buchwitz, M., Burrows, J. P., Deutscher, N. M., Griffith, D. W. T., Heymann, J., Macatangay, R., Messerschmidt, J., Notholt, J., Rettinger, M., Reuter, M., Sussmann, R., Velazco, V. A., Warneke, T., Wennberg, T. O., and Wunch, D.: Atmospheric greenhouse gases retrieved from SCIAMACHY: comparison to ground-based FTS measurements and model results, Atmos. Chem. Phys., 12, 1527–1540, doi:10.5194/acp-12-1527-2012, 2012.

Schneising, O., Heymann, J., Buchwitz, M., Reuter, M., Bovensmann, H., and Burrows, J. P.: Anthropogenic carbon dioxide source areas observed from space: assessment of regional enhancements and trends, Atmos. Chem. Phys. Discuss., 12, 31 507–31 530, doi:10.5194/acpd-12-31507-2012, 2012b.

Solomon, S., Qin, D., Manning, M., Chen, Z., Marquis, M., Averyt, K. B., Tignor, M., and Miller, H. L., eds.: Climate change 2007: The physical science basis, Contribution of working group I to the Fourth Assessment Report of the Intergovernmental Panel on Climate Change (IPCC), Cambridge University Press, 2007.

Stephens, B. B., Gurney, K. R., Tans, P. P., Sweeney, C., Peters, W., Bruhwiler, L., Ciais, P., Ramonet, M., Bousquet, P., Nakazawa, T., Aoki, S., Machida, T., Inoue, G., Vinnichenko, N., Lloyd, J., Jordan, A., Heimann, M., Shibistova, O., Langenfelds, R. L., Steele, L. P., Francey, R. J., and Denning, A. S.: Weak northern and strong tropical land carbon uptake from vertical profiles of atmospheric CO_2, Science, 316, 1732–1735, doi:10.1126/science.1137004, 2007.

Tilstra, L. G., de Graaf, M., Aben, I., and Stammes, P.: Analysis of 5 years of SCIAMACHY absorbing aerosol index data, Proceedings ENVISAT Symposium, Montreux, Switzerland, ESA Special Publication SP-636, 2007.

Tolton, B. T. and Plouffe, D.: Sensitivity of radiometric measurements of the atmospheric CO_2 column from space, Appl. Opt., 40, 1305–1313, 2001.

van Diedenhoven, B., Hasekamp, O. P., and Aben, I.: Surface pressure retrieval from SCIAMACHY measurements in the O_2 A Band: validation of the measurements and sensitivity on aerosols, Atmos. Chem. Phys., 5, 2109–2120, 2005.

Vaughan, M., Young, S., Winker, D., Powell, K., Omar, A., Liu, Z., Yongxiang, H., and Hostetler, C.: Fully automated analysis of space-based lidar data: an overview of the CALIPSO retrieval algorithms and data products, Laser Radar Techniques for Atmospheric Sensing, 5575, 16 – 30, doi:10.1117/12.572024, 2004.

Winker, D., Vaughan, M., Omar, A., Hu, Y., Powell, K. A., Liu, Z., Hunt, W., and Young, S.: Overview of the CALIPSO Mission and CALIOP Data Processing Algorithms, Journal of Atmospheric and Oceanic Technology, 26, 2310–2323, 2009.

Winker, D. M., Hunt, W. H., and McGill, M. J.: Initial performance assessment of CALIOP, Geophys. Res. Lett., 34, L19 803, doi:doi:10.1029/2007GL030135, 2007.

Wunch, D., Toon, G. C., Blavier, J., Washenfelder, R. A., Notholt, J., Connor, B. J., Griffith, D. W. T., Sherlock, V., and Wennberg, P. O.: The Total Carbon Column Observing Network, Phil. Trans. R. Soc. A, 369, 2087–2112, doi: doi:10.1098/rsta.2010.0240, 2011.

Yang, Z., Washenfelder, R. A., Keppel-Aleks, G., Krakauer, N. Y., Randerson, J. T., Tans, P. P., Sweeney, C., and Wennberg, P. O.: New constraints on Northern Hemisphere growing season net flux, Geophys. Res. Lett., 34, L12 807, doi: 10.1029/2007GL029742, 2007.

Yokota, T., Oguma, H., Morino, I., and Inoue, G.: A nadir looking SWIR sensor to monitor CO_2 column density for Japanese GOSAT project, Proceedings of the twenty-fourth international symposium on space technology and science. Miyazaki: Japan Society for Aeronautical and Space Sciences and ISTS, pp. 887–889, 2004.

Yoshida, Y., Ota, Y., Eguchi, N., Kikuchi, N., Nobuta, K., Tran, H., Morino, I., and Yokota, T.: Retrieval algorithm for CO_2 and CH_4 column abundances from short-wavelength infrared spectral observations by the Greenhouse gases observing satellite, Atmos. Meas. Tech., 4, 717–734, doi:10.5194/amt-4-717-2011, 2011.

List of Figures

List of Tables

Acknowledgements

This dissertation would not have been possible unless the support which I experienced throughout my PhD project. For this reason, I would like to thank:

- my supervisor Professor John P. Burrows for giving me the opportunity to work on this interesting topic and his valuable advice,
- Otto Schrems for his interest in my work and his willingness to be the second reviewer of this thesis,
- Michael Buchwitz, Maximilian Reuter and Oliver Schneising who guided me throughout my project, gave me support on many scientific and technical issues and had always time for fruitful discussions,
- all recent and former members of the greenhouse gas group, especially Voltair A. Velazco, Dhanyalekshmi Pillai, Thomas Krings, Heinrich Bovensmann,
- Alexei and Vladimir Rozanov for their support on the radiative transfer code SCIATRAN,
- all my other colleagues at the Institute of Environmental Physics,
- the European Union (CityZen, MACC), the European Space Agency (ESA) (ADVANSE, CARBONGASES, GHG-CCI, SQWG), the Deutsches Zentrum für Luft- und Raumfahrt (DLR) (SADOS), the Postgraduate International Programme (PIP) and the University and the State of Bremen for the financial support,
- the National Oceanic and Atmospheric Administration of the United States (NOAA) for providing me with the CarbonTracker 2010 data, the European GEMS project for the global aerosol data set, the NASA Langley Research Center Atmospheric Science Data Center for providing me with the CALIOP/CALIPSO data,
- the Total Carbon Column Observing Network (TCCON) for giving me the access to their FTS data. I especially want to thank Justus Notholt, Thorsten

Warneke and Nicolas Deutscher for the Bremen and Bialystok FTS data, Ralf Sussman and Marcus Rettinger for the Garmisch FTS data, David Griffith for the Darwin and Wollongong FTS data and Paul Wennberg for the Lamont and Park Falls FTS data,

- my family and my friends for their moral support in the last few years. In particular, I want to thank my parents for their interest in my work and their believe in me. Thank you.

As I do not want to miss anyone, I want to say thank you all.